Optimisation of

the conversion probability of axions

in a transversal magnetic field

Optimierung der Konversionswahrscheinlichkeit

von Axionen im transversalen Magnetfeld

von

Christoph Mangels

geboren am:

24. August 1990

Master-Arbeit im Studiengang Physik an der Universität Hamburg

Institut für Experimentalphysik

2017

1. Gutachter: Prof. Dr. Dieter Horns
2. Gutachter: Dr. Andrei Lobanov

Abstract

The largest fraction of the matter in the Universe is not consistently observable yet. The structure of this dark matter is still unknown. One possibility is that it is comprised of very weakly interacting particles with masses in the sub-eV range, called WISPs. Among these well-motivated candidates are the axions, axion-like particles and hidden photons. Recently, a new haloscopic experiment enabling broadband searches for these particles was proposed. The required magnetic field is planned to be generated by a two-dimensional Halbach array. In this thesis, preliminary computations regarding the characteristics of such arrays are presented. Multiple different two-dimensional Halbach arrangements are analysed to find the most suitable one for the experiment. Additionally, preliminary measurements of the magnetic field of real arrays are made to confirm the computational results.

Zusammenfassung

Der Großteil der Materie im Universum ist bisher nicht beständig beobachtbar. Die Natur dieser dunklen Materie ist immer noch unbekannt. Ein möglicher Erklärungsansatz ist, dass sie aus sehr schwach wechselwirkenden Teilchen mit Massen im Subelektronenvoltbereich besteht, den sogenannten WISPs. Zu diesen gut motivierten Teilchen gehören unter anderen die Axionen, die Axion-like-particles und die Hidden Photons. Kürzlich wurde ein neues haloskopisches Experiment zur breitbandigen Suche nach ebendiesen Teilchen vorgestellt. Es ist geplant, das hierzu benötigte Magnetfeld durch ein zweidimensionales Halbach-Array zu erzeugen. Das Ziel der vorliegenden Arbeit sind vorbereitende Ergebnisse bezüglich dieses Experiments. Es werden computergestützte Berechnungen hinsichtlich der Eigenschaften solcher Halbach-Arrays präsentiert. Um die für dieses Experiment passendste zweidimensionale Halbach-Anordnung zu ermitteln, werden mehrere verschiedene Anordnungen analysiert. Des Weiteren werden Magnetfeldmessungen an realisierten Arrays durchgeführt, um die theoretisch ermittelten Ergebnisse zu bestätigen.

Contents

1. Introduction

The most acknowledged cosmological model in modern physics is the "ΛCDM"-model, with Λ denoting the cosmological constant and CDM abbreviating "cold dark matter" [1]. According to this model, the energy density Ω in the Universe is comprised of three constituents: the known baryonic matter, the yet unknown dark matter and the dark energy. The results of the Planck mission published in 2016 [2] yield that the combined fraction of baryonic and dark matter adds up to 30.8% ($\Omega_m = 0.308 \pm 0.012$) of the energy density and that the dark energy accounts for the remaining 69.2% ($\Omega_\Lambda = 0.692 \pm 0.012$). If viewed independently of each other, the baryonic matter accounts for a fraction of 4.9% ($\Omega_b h^2 = 0.02226 \pm 0.00029$) and the dark matter for a fraction of 25.9% ($\Omega_c h^2 = 0.1186 \pm 0.0020$), with h correlated to the Hubble constant as $H_0 = 100h\,\mathrm{km/(s\,Mpc)} = 67.81 \pm 0.92$. Two of the main open questions of astro- and particle physics are the natures of the dark energy and the dark matter. While the former one is by far the bigger mystery [3], there are numerous theories trying to answer the question regarding the dark matter. Although theories with various approaches were set up, none could be verified by experimental results. A possible solution for the dark matter problem are the "weakly interacting slim particles" [4]. These WISPs are well-motivated particles with masses in the sub-eV range, which interact weakly with Standard Model particles. Among these hypothetical particles are the axion, axion-like particles (ALPs) and hidden photons, which naturally appear in the compactifications of string theories [5].

The detection of most possible dark matter candidates is utterly challenging due to them interacting only very weakly with Standard Model particles. Regardless of the manifold experiments for direct and indirect dark matter searches, no signal could be consistently found yet [6]. In the WISP case, there are basically three main types of experiments, which are all based on WISP to photon conversions, namely haloscopes, helioscopes and light-shining-through-a-wall experiments. These types differ in the considered WISP sources and are searching for WISPs produced in the galactic dark matter halo, the sun and the laboratory respectively. A new broadband haloscope proposed recently [7] is giving attention to the conversions of WISPs and photons at reflective surfaces. This experiment called BRASS ("Broadband Radiometric Axion SearcheS") is the main topic of this thesis. It offers the possibility of exploring large areas of the parameter space of both axions (and ALPs) and hidden photons with relatively low effort.

Axions and ALPs require an external magnetic field to convert into photons. Therefore, a rather crucial part in the design process of a new WISP experiment searching for axions and ALPs is the generation of a suitable magnetic field. The field used by BRASS is planned to be generated by magnets forming a so-called “Halbach array”. This term comprises particular arrangements of magnets with an increased magnetic field on one side and a decreased field at the opposite side [8]. BRASS is still in the preliminary phase, in which the most suitable magnet composition is aimed to be found. For this purpose, analyses concerning Halbach arrays and their properties are made. In a first step, they are limited to small length scales. To get a complete overview, these analyses include both computational and experimental approaches.

This thesis is structured as follows: chapter 2 focuses on the theoretical background of the BRASS experiment, which itself is the subject of chapter 3. In chapters 4 and 5 the computational and the experimental results of the preliminary analyses are presented. An outlook of future topics is given in chapter 6 and finally the conclusion can be found in chapter 7.

2. Theoretical background

2.1. Dark matter

The term “dark matter" is used for matter which is not directly detectable through electromagnetic radiation. This type of matter neither emits nor absorbs or reflects light and is therefore invisible for telescopes [9]. Contrary to common baryonic matter which exists either as luminous matter (stars, hot gas) or as non luminous matter (planets, cold gas), the dark matter could not be measured directly yet [6]. However, its existence is well motivated due to observations regarding gravitation on various astrophysical levels. The results of these observations are mostly explainable if additional mass is assumed. Nevertheless, the nature of dark matter is still unknown, although various theories were constructed to change this situation. Aside from theories introducing new particles as candidates for dark matter, there are also theories declining the idea of additional mass and instead introducing new options in the calculation of the gravitational force. As a matter of fact, neither of all these theories could be supported by experimental results, and therefore both approaches are equally legitimate at this point.
This section presents some of the mentioned observations as well as selected theories for their explanation, whereupon both mentioned approaches will be covered.

2.1.1. Evidences for dark matter

There are various astrophysical observations made in the past century which can be considered as evidences for the existence of dark matter. These evidences are present on multiple astrophysical length scales, ranging from galactic to cosmological lengths. A selection of the most important evidences is given in this section, arranged in chronological order.

Density of the Coma galaxy cluster

One of the first hints for dark matter was discovered by Fritz Zwicky in 1933 [10]. He analysed the measurements of the Coma galaxy cluster taken with the 100-inch Hooker telescope. Using the results concerning the size and the mass of the cluster as well as the virial theorem

$$\overline{E_{kin}} = -\frac{1}{2}\overline{E_{pot}} \ , \tag{2.1}$$

he calculated the mean velocity difference of the particular galaxies of the cluster. Zwicky estimated the mass of the galaxy cluster to be uniformly distributed in space. For his calculation he assumed the radius to be $R = 10^6\,\mathrm{ly} = 10^{24}\,\mathrm{cm}$ and the Coma cluster to consist of 800 individual galaxies with a mass of $M_{\mathrm{galaxy}} = 10^9\,M_\odot$ each, resulting in a total mass $M = 1.6 \times 10^{42}\,\mathrm{kg}$. He then obtained the mean velocity difference as follows, considering $G \simeq 6.67 \times 10^{-11}\,\frac{\mathrm{m}^3}{\mathrm{kg\,s}^2}$:

$$\Omega = -\frac{3}{5} \cdot G \cdot \frac{M^2}{R} \tag{2.2}$$

$$\overline{E_{pot}} = \frac{\Omega}{M} \simeq -6.4 \times 10^3\,\frac{\mathrm{km}^2}{\mathrm{s}^2} \tag{2.3}$$

$$\overline{E_{kin}} = \frac{\overline{v^2}}{2} = -\frac{\overline{E_{pot}}}{2} = 3.2 \times 10^3\,\frac{\mathrm{km}^2}{\mathrm{s}^2} \tag{2.4}$$

$$\Rightarrow \quad \left(\overline{v}^2\right)^{\frac{1}{2}} = 80\,\frac{\mathrm{km}}{\mathrm{s}}. \tag{2.5}$$

In comparison to this result, the measurements showed velocity differences of at least 1500 to 2000 $\frac{\mathrm{km}}{\mathrm{s}}$. The experimental values are therefore 20 times larger than the theoretical value. This implies a mass 400 times larger than the one assumed by Zwicky.
In this calculation Zwicky assumed the Coma galaxy cluster to be a mechanically stable system, allowing him to use the virial theorem. He also discussed the case of an unstable system, in which the whole potential energy would appear as kinetic energy. As this reduces the difference just by a factor of 2, the necessity for an explanation for this missing mass remains. Another case discussed is the assumption that the entire mass consists of visible baryonic mass. This would imply that the individual galaxies of the cluster have to drift away from each other with time, keeping the distinct velocities of around 1000 to 2000 $\frac{\mathrm{km}}{\mathrm{s}}$. This is at odds with the observed distinct velocities of at most 200 $\frac{\mathrm{km}}{\mathrm{s}}$. A fourth and last attempt in the discussion was to take the redshift into account. This resulted in a necessity for even more additional mass than in the first two cases.
Since three of the four cases required the existence of invisible mass while the last case could be excluded by existing observations, Zwicky concluded that dark matter could account for the missing mass. He also assumed that its density could be higher than the density of baryonic matter.

Rotation curves

Even after the first hints were found, the theory of dark matter was declined by most physicists. This position first changed when Rubin and Ford analysed the rotation curves of galaxies [11]. A rotation curve displays the radial velocities of stars and gas as a function of their distance to the galactic centre. It is usually obtained by combining the measurements of the hydrogen line with optical surface photometry.
Assuming the visible matter in galaxies behaves according to Newtonian dynamics, the radial velocity v as a function of the radius r can be described as

$$v(r) = \sqrt{\frac{G\ M(r)}{r}} \tag{2.6}$$

while the mass distribution $M(r)$ is obtained by

$$M(r) = 4\pi \int \rho(r)\ r^2\ \mathrm{d}r\ . \tag{2.7}$$

Beyond the edge of the optical disk, M is constant. This implies $v(r) \propto \sqrt{1/r}$.
In contrast to this approach, the observed rotation curves show a flat gradient where $v(r)$ is approximately constant (a typical rotation curve is shown in 2.1). This is only possible if the density is distributed as $\rho(r) \propto 1/r^2$ and therefore $M(r) \propto r$. Such a distribution of density and mass is not explainable with visible matter only, but with an existing halo of dark matter surrounding the galaxy [12].
The observation of many different galaxies showed that the flat behaviour is the normal case and not just a coincidence. More examples of flat rotation curves can be found in [13].

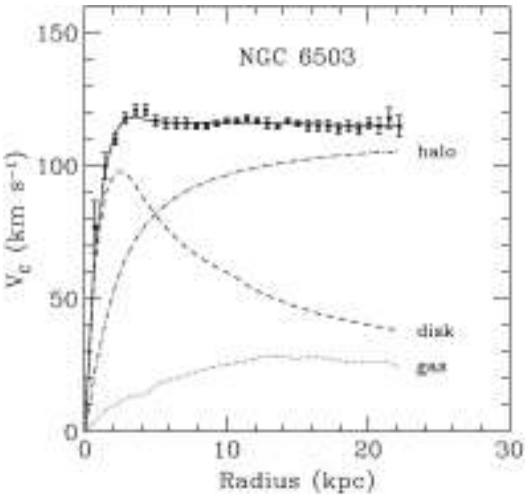

Figure 2.1.: Rotation curve of the galaxy NGC 6503. The solid line depicts the experimental result. The interrupted lines depict the theoretically predicted contributions of gas (dotted), galaxy disk (dashed) and dark matter halo (dash-dotted). From [12].

Gravitational lenses

The effect of gravitational lensing describes the deflection of light in a strong gravitational field [14]. It is observable if a massive object (the "gravitational lens") lies in the line-of-sight between a light source and the observer. The direction of propagation of light propagating near the gravitational lens is changed by the strong gravitation. Depending on the geometry of the three mentioned objects, the mass and mass distribution of the lens and further factors, the light source seems to be shifted or multiplied or appears as a (part of a) ring of light. Two examples of gravitational lensing are shown in figures 2.2 and 2.3. The effect is classified into 3 types [14]: the strong lensing, the weak lensing and the microlensing. The strong lensing is the "classical" lensing effect with very massive objects like galaxies, galaxy clusters or black holes functioning as the lens. It creates all three mentioned kinds of distortion, which can be detected easily. The weak lensing occurs if the lens is less heavy or far away. Contrary to the strong lensing, the effect is often only detectable via statistical methods and only an apparent shifting of the light source is possible. Lastly, the microlensing describes the effect if a comparatively light object like a single star is functioning as the lens. This lens is so weak that no distortion can be seen, but instead the amount of light arriving at the observer changes in time. The microlensing effect was used to detect and observe some MACHOs which are discussed in section 2.1.2.

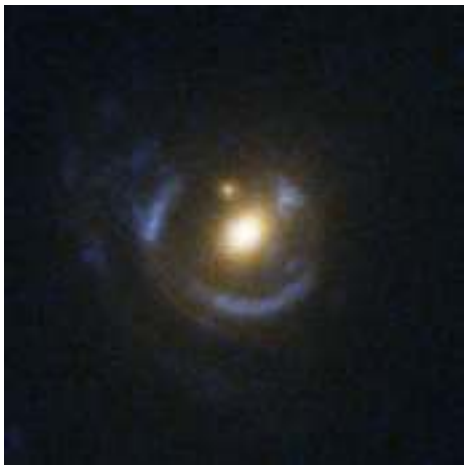

Figure 2.2.: Example of the gravitational lensing. Due to this effect the background light source appears as a part of a ring. Such a ring is also called "Einstein ring". From [15].

It is possible to calculate the fraction of dark matter in relation to the entire matter accountable for the gravitational lensing. This is done by comparing the assumed gravitational potential based on the visible matter to the measured one reconstructed via gravitational lensing. This way, several eminent astrophysical observations were made. One example is the Bullet Cluster described in the next section. Moreover, it is worth mentioning that the gravitational lensing was the first experimental validation of the general theory of relativity. See chapter 4 in [14] and references therein for further information.

(a) telescope picture

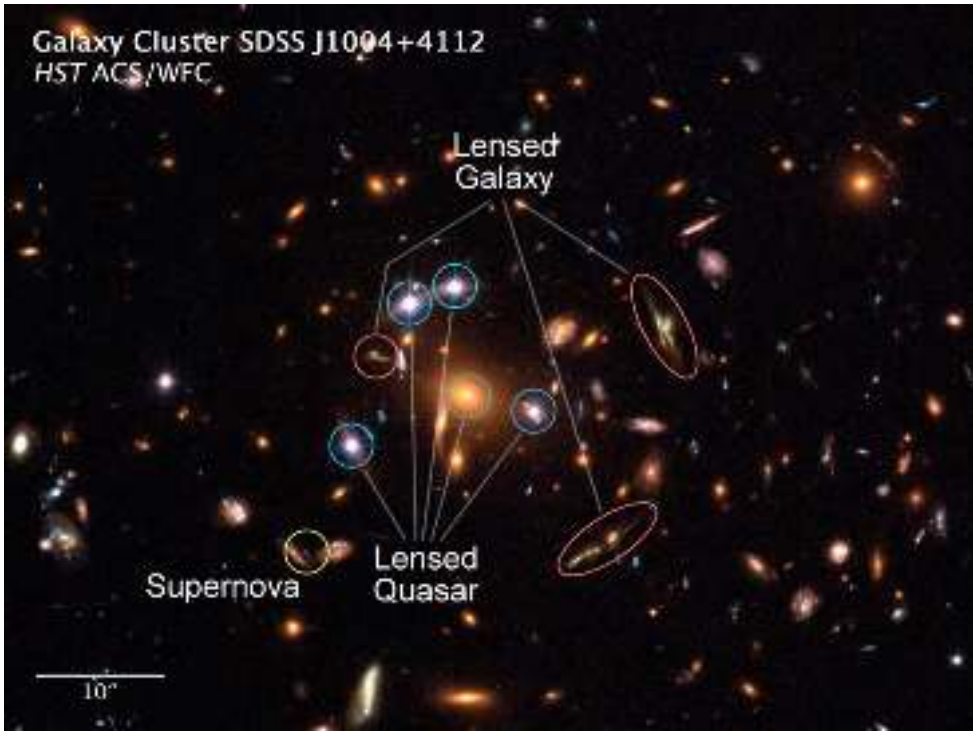

(b) multiplied objects

Figure 2.3.: Another example of the gravitational lensing. Figure (a) is the picture taken by the telescope. The background objects are marked in figure (b). Due to the gravitational lensing of a foreground galaxy cluster, the image of a background galaxy got multiplied three times and seems to be circular. The image of a background quasar even got multiplied five times. This is the first observation of a five-fold multiplication of light from a background light source. From [16].

"Bullet Cluster" 1E 0657-558

One major evidence for the existence of dark matter is provided by the measurements of the galaxy cluster 1E 0657-558 taken in 2006 and presented in [17]. This galaxy cluster consists of two subclusters with different size, which collided approximately 100 million years ago, and is also called "Bullet Cluster" because of the shape of the smaller subcluster. Measurements in the optical range (2.4(a)) showed that the two subclusters are clearly distinguishable as a result of two areas with an increased galaxy density with a separation of 0.72 Mpc. Furthermore, the intracluster medium (ICM) which accounts for most of the baryonic matter in the cluster was observed via x-ray measurements (2.4(b)). It turned out that this medium is located mainly in the centre of the cluster and thus between the two subclusters. The results of these two measurements can be reconciled with each other by means of the collision of the subclusters. Whereas the galaxies remained almost collisionless, the gas of the ICM was slowed down by many small collisions due to the smaller distances between the individual components.
In addition to these measurements, the gravitational potential of the Bullet Cluster was analysed via gravitational lensing (2.4(c)). Naturally, this potential is highest where the most matter is present. The analysed potential offers two maxima near the two areas with an increased galaxy density. Since these areas contain less matter than the ICM, this result is a strong evidence for the existence of additional, non-visible matter inside the subclusters. This evidence is all the more eminent as the offset between the gravitational distribution and the gas distribution adds up to 8σ and can not be explained by "simple" theories without dark matter (see section 2.1.3).
The observations on the Bullet Cluster show that dark matter, if it proves to be existent, interacts only weakly with the ICM. It also shows that dark matter behaves like the galaxies during self-intersection, given that their trajectories are similar.

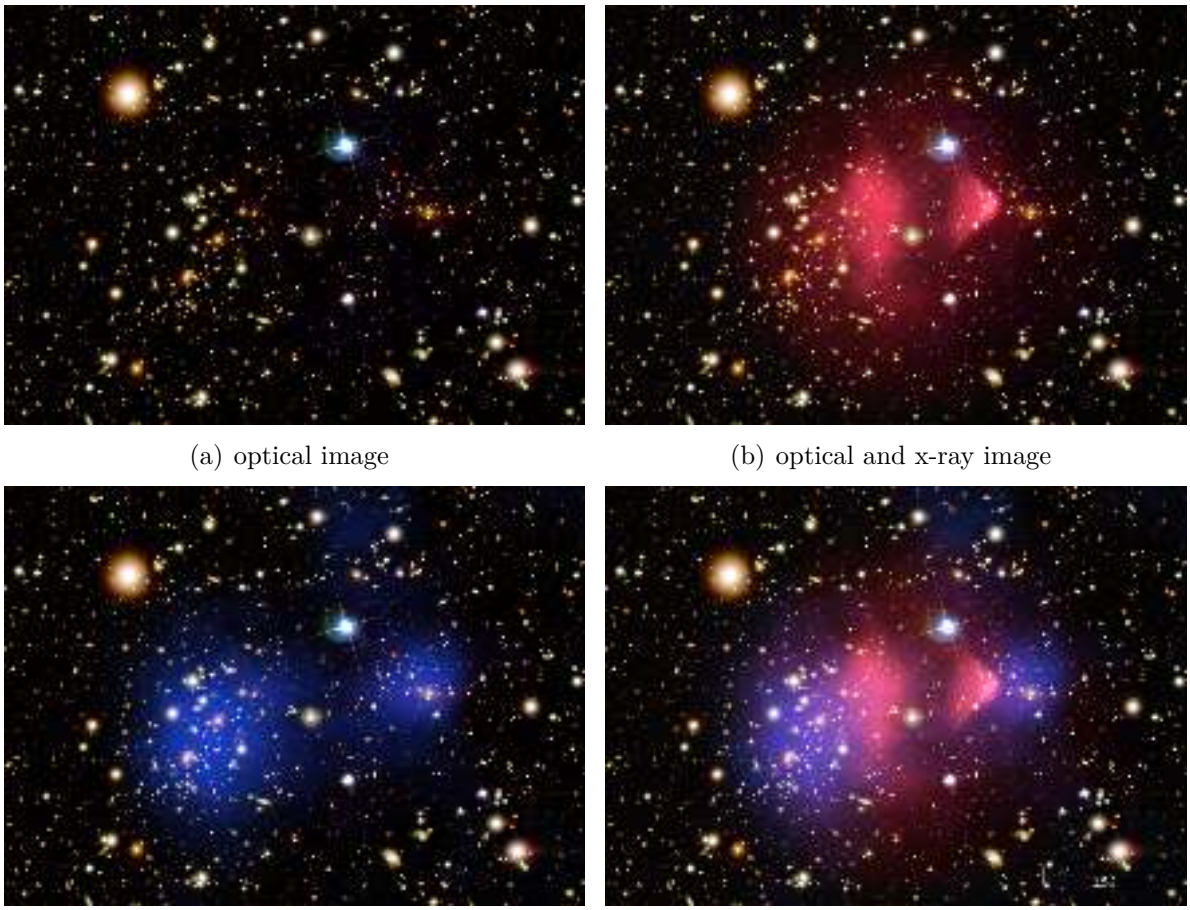

(a) optical image

(b) optical and x-ray image

(c) optical image with depiction of gravitational potential

(d) combination of all three components

Figure 2.4.: Several images of the Bullet Cluster. Figure (a) shows the optical image. This is superposed with the x-ray image in figure (b), in which the intracluster medium is coloured in red. By the shape of the smaller gas cloud of the intracluster medium (the "Bullet") it is clearly visible that both gas clouds interacted heavily while the subclusters were colliding. In figure (c) the optical image is superposed with a depiction of the gravitational potential. Its distribution is obtained through the analysis of gravitational lensing and is coloured in blue. Finally, figure (d) is a combination of the three components. Here, it is also clearly visible that the maxima of the gravitational potential do not coincide with the gas clouds. From [18].

2.1.2. Dark matter candidates

In the past decades, a lot of different candidates were suggested as a solution to the dark matter mystery. These candidates need to meet essentially three conditions to possibly be capable of explaining dark matter [19]. Naturally, they have to be undetectable directly through radiation. Furthermore, they have to be stable relating to cosmological timescales. Otherwise, they would have been decayed in large part until now. Finally, it is crucial that a sufficiently large quantity of these candidates is existing to equate to the expected mass density of dark matter. Note that it may be possible that two or more candidates contribute to the entire dark matter mass density instead of just one.
The candidates suggested to date are classified using two major criteria. On the one hand, they are differentiated between "baryonic" and "non-baryonic" dark matter, assuming the latter to be the dominant part. This assumption is most notably based on the measurements of the Bullet Cluster and the consequential observation that dark matter interacts weakly with itself during self-intersection. On the other hand, the candidates are differentiated between "hot" and "cold" dark matter or, in other words, relativistic and accordingly non-relativistic dark matter. It is assumed that non-relativistic cold dark matter has to account for the largest part, whilst the fraction of relativistic hot dark matter is rather small. If it would be vice versa, there would have been a "top-down-scenario" in the structure building inside the Universe. This means that galaxy clusters would have formed prior to galaxies, which would for their part have formed prior to stars. However, this scenario is excluded by observations stating that the Milky Way is older than the Local Group [12]. In the following section various dark matter candidates are discussed shortly. Note that only a selection of suggested candidates are presented.

Neutrinos

In the Standard Model of particle physics the neutrino is the only possible dark matter candidate. Neutrinos only interact via gravitation and weak interaction and are therefore hard to detect. The Standard Model includes three kinds of neutrinos, distinguished by their flavour (electron, muon or tau neutrino), which were all assumed to be massless. However, the observation of neutrinos changing into different flavours (neutrino oscillations) contrasts strongly with this assumption. Such a change is only possible if the rest mass of neutrinos is non-zero and if the differences of the masses of the flavours are rather small. Measurements of the spectrum of the β-decay of tritium taken in Mainz and Troizk offered an upper limit for the neutrino mass as [20]

$$m_\nu < 2.05\,\mathrm{eV}(95\%CL). \tag{2.8}$$

The next generation of this kind of experiment is the KATRIN-experiment in Karlsruhe which is aiming to improve this limit by one order of magnitude [21].

The mass density of neutrinos in the Universe is given by [12]

$$\Omega_\nu h^2 = \sum_{i=1}^{3} \frac{m_i}{93\,\mathrm{eV}}, \tag{2.9}$$

with m_1, m_2 and m_3 as the masses of the three neutrino flavours. Considering the results from Mainz and Troizk, the mass density adds up to

$$\Omega_\nu h^2 \lesssim 0.07. \tag{2.10}$$

Obviously, the neutrinos of the Standard Model can only contribute a small part to the dark matter mass density.
Aside from this, there is another reason for neutrinos to not be the main constituent of dark matter. Due to their small mass, neutrinos move with a velocity close to the velocity of light. Therefore, they are classified as relativistic hot dark matter and, as described above, hot dark matter is less abundant than cold dark matter.

Sterile neutrinos

Sterile neutrinos are hypothetical elementary particles expanding the Standard Model of particle physics. Contrary to common neutrinos, they only interact via gravitation and kinetic mixing with common Standard Model particles. The nature of sterile neutrinos is yet to be discovered, though they are often assumed to be right-handed neutrinos. The "Neutrino Minimal Standard Model" (νMSM) is a theory proposed by Canetti, Drewes and Shaposhnikov [22] with the ambition to explain the nature of dark matter, the neutrino oscillations and the baryon asymmetry problem, i.e. the dominance of matter compared to antimatter in the Universe, at once. This theory expands the Standard Model with three right-handed neutrinos without changing the gauge group. This could solve three major puzzles of modern physics without the need to introduce major modifications. However, until now, neither the νMSM nor other theories concerning sterile neutrinos could be supported, let alone verified by experimental results.
Using data from the WMAP experiment regarding the optical depth and the reionization it was possible to obtain a lower limit for dark matter consisting of sterile neutrinos [12]:

$$m_{\nu_s} \gtrsim 10\,\mathrm{keV} \tag{2.11}$$

MACHOs

The term MACHO is an acronym for "massive astrophysical compact halo object" and describes massive celestial bodies inside the halo of a galaxy, which are emitting no or almost no radiation. Examples of such objects are black holes, brown dwarves and neutron stars. They are per definition not detectable via telescopes and therefore logically candidates for dark matter. Instead, their detection is made via gravitational microlensing as described in section 2.1.1, since their mass is sufficient enough to slightly alter the direction of propagation of light. The MACHO collaboration measured microlensing events in front of the Magellanic Clouds and, based on their results, predicted in 2000 that 20% of the dark matter halo of the Milky Way is composed of MACHOs [23]. However, this prediction was challenged by more sensitive measurements of the EROS2 collaboration a few years later [24].
MACHOs are consisting of baryons and are therefore classified as baryonic dark matter. Hence it is assumed that they only contribute a small part to the entire dark matter.

Black hole particle

A relatively new candidate called "black hole particle" was proposed in 2014 by Dokuchaev and Eroshenko [25]. This particle consists of an electrically charged, non-rotating black hole which can be considered as an atomic nucleus and electrons in bound quantum states. A system with such a composition was first mentioned by Stephen Hawking in 1971 [26]. He supposed that these black holes could have been generated via density fluctuations in the very early universe and that they could appear with every mass $m \geq 10 \times 10^{-5}\,\mathrm{g}$. He furthermore supposed that the systems of black hole and electrons could behave like atoms with proton number Z and calculated that these systems could possess an electrical charge of up to $Z = 30e$. This would make them detectable in bubble chambers. Dokuchaev and Eroshenko took this work and added some new ideas. Assuming a central black hole characterized by the Reissner-Nordström metric[1] they postulate configurations of the system in such a way that the electrons are arranged in quantum states inside the Cauchy horizon[2]. Given the proper amount of electrons the entire system becomes electrically neutral and seems to be a black hole characterized by the Schwarzschild metric if observed from the outside. This way its cross section is very small and it barely interacts with baryonic matter. Naturally, the black hole particle is therefore hardly detectable and thus a dark matter candidate.

[1] The Reissner-Nordström metric describes charged, non-rotating black holes, whereas the Schwarzschild metric describes uncharged, non-rotating black holes.
[2] The Reissner-Nordström metric includes two singularities, thus there exist two event horizons. The Cauchy horizon is the inner one.

WIMPs

For a long time the "weakly interacting massive particles" (WIMPs) were the favourite dark matter candidates. These massive particles possess masses between 10 and 1000 GeV and are thus classified as non-relativistic cold dark matter. They only interact via gravitation and weak interaction and potentially via yet unknown interactions with cross sections smaller than the cross section of the weak interaction, but not via electromagnetic or strong interaction. Hence, they interact similarly to neutrinos and are able to pass areas with high baryonic densities almost interaction-free [27].
One exemplary theory postulating the WIMPs is the "Minimal Supersymmetric Standard Model" (MSSM) [19]. This theory is an extension of the Standard Model allocating a new particle called "super partner" to each common particle. The super partner of a fermion is a boson and vice versa. Assuming an unbroken symmetry, the super partners would possess an equal mass and equal quantum numbers except for the spin. Since no super partner was detected yet, the supersymmetry is supposed to be spontaneously broken. This way, the yet undetected particles could possess masses much larger than the common particles of the Standard Model. In combination with a theory regarding the R-parity a stable supersymmetric particle arises as a possible WIMP [12]. Since the nature of such a particle is still unknown, it was generally called "lightest supersymmetric particle" (LSP). With time, all supersymmetric particles decay into one or multiple LSPs. Due to the assumed R-parity conservation, the stable LSP will not decay any further, especially not into particles of the Standard Model. The sneutrino, the neutralino and the gravitino are three possible candidates for the LSP arising in the MSSM. The neutralino, which is a mixture of the super partners of the gauge bosons of the Standard Model, is the overall preferred one, whereas the sneutrino and the gravitino could be excluded as dark matter candidates to a great extent [19].
As being dark matter candidates, WIMPs are hardly detectable. Nevertheless, a lot of different experiments exist, searching both directly and indirectly for WIMPs (see [12] and references therein for further detail). However, their results differ strongly until now. As an example, the XENON100 experiment in Gran Sasso published strong exclusion limits as shown in figure 2.5. Although no WIMP could be found experimentally by XENON100 [28], the DAMA experiment (also in Gran Sasso) claimed to have obtained sufficient evidence for the existence of WIMPs [29]. Due to such contrasts, it seems to take some more time until satisfying results will be realized either for verification or for falsification.

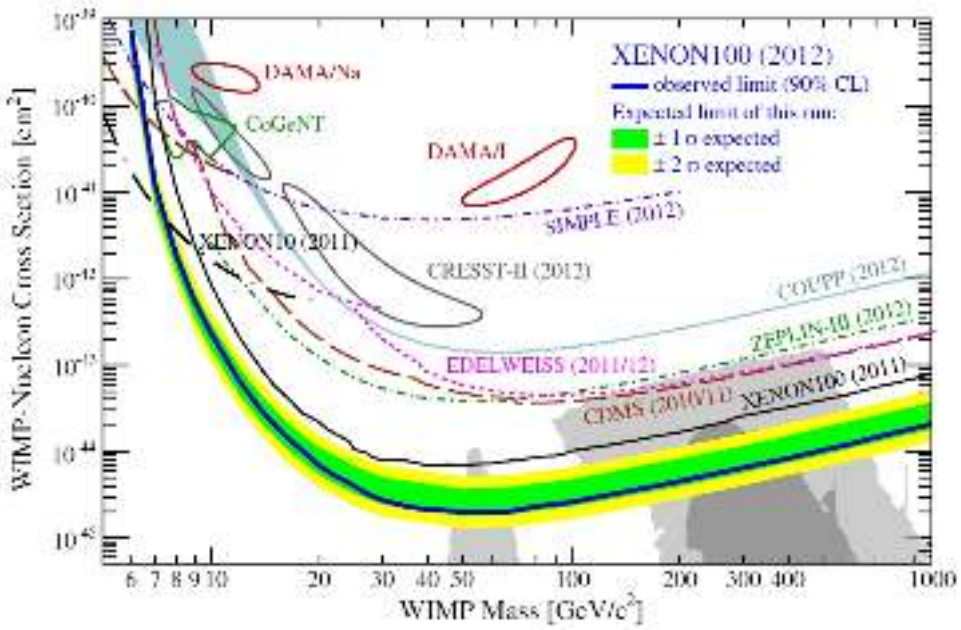

Figure 2.5.: Results of the XENON collaboration for spin-independent scattering. The WIMP mass is plotted on the x-axis and the WIMP-nucleon cross section is plotted on the y-axis. The solid blue line represents the exclusion limits with 90% CL. The sensitivity of the measurements is represented by the green (1σ) and the yellow (2σ) band. For comparison, other experimental limits with 90% CL and detection claims with 2σ are also shown. The regions preferred by supersymmetric models are depicted as the grey shades (dark: 1σ, light: 2σ). From [28].

2.1.3. Alternative theories

Many of the mentioned observations are also explainable via theories not including dark matter. The most prominent of these theories are MOND and MOG, which are shortly introduced in this section. For further information and detailed discussions see the given references.

MOND

MOND is an acronym for "modified Newtonian dynamics" and describes an expansion of the Newtonian dynamics. The theory was first proposed by Milgrom in 1983 [30], who did not exclude the existence of dark matter explicitly, but estimated it to be of minor relevance. The main ambition of Milgrom was to explain the flat rotation curves of galaxies (which are described in section 2.1.1). His basic premise was that Newtonian dynamics were solely tested in high-acceleration environments like the Earth or the Solar System, but not in low-acceleration environments like stars in outer galaxy regions.

Milgrom expanded the equation of motion as follows:

$$F_N = m \cdot \mu\left(\frac{a}{a_0}\right) \cdot a. \tag{2.12}$$

Here, a_0 is a new fundamental constant and $\mu(x)$ is a function unspecified yet. Limits for this function are $\mu(x) \to 1$ for $x \gg 1$ (agreement with Newtonian dynamics) and $\mu(x) \to x$ for $x \ll 1$ (consistency with astrophysical observations).
The most important characteristic of this theory is the fact that it only requires a simple modification of a known equation and a new fundamental constant. This way, multiple observations aside from the flat rotation curves could be explained by MOND. However, the results of the Bullet Cluster were incompatible with the version of the theory proposed by Milgrom. By switching to a Finsler geometry, this inconsistency could be avoided, but this was done at the cost of simplicity [31].
Different extensions of Milgrom's original work were presented by Bekenstein. In a first attempt, together with Milgrom, he developed a theory of gravity called "AQUAL" ("A Quadratic Lagrangian") which is based on MOND but using a Lagrangian [32]. Further enhancements led to a theory called "TeVeS" ("tensor-vector-scalar gravity") which is a relativistic generalization of MOND [33]. Although these enhanced theories solve some of the problems of the original MOND, they are also incompatible with certain observations. A truly generalized MOND theory consistent with all observations made is therefore still in development.

MOG

MOG is an acronym for "modified gravity" and describes a theory which was first proposed by Moffat in 2006 as the "scalar-tensor-vector gravity" [34]. In this theory he postulates a new vector field in a way that the gravitational constant G, the coupling constant ω and the mass μ of this field can vary depending on time and space. In addition, he postulates a force counteracting the gravitation on small length scales, hence expanding the Standard Model with a fifth basic force. In contrast to MOND, all the mentioned evidences for dark matter given in section 2.1.1 could be also explained with MOG. As an example, the explanation for the results of the Bullet Cluster was published shortly after the publication of said results.[35] Nevertheless, despite being a powerful theory, MOG could not be supported explicitly by experimental results, analogue to the theories including dark matter.

2.2. WISPs

For a noticeable amount of time, the search for dark matter constituents focused mainly on the WIMPs. The moving spirit in this context was the expected possibility to explore the electroweak scale with the Large Hadron Collider (LHC). However, despite the great effort put into the WIMP search, neither the runs at the LHC nor the measurements of further experiments could yet deliver a clear indication for the existence of these particles [5]. This enabled another sort of hypothetical particles to move closer into the focus and gain attention, namely the ones called "weakly interacting slim particles" (WISPs). Similar to the WIMPs and indicated by their name, these WISPs interact only weakly with Standard Model particles. The big difference is their mass. While WIMPs possess masses in the higher GeV range, the masses of WISPs are in the sub-eV range. Among these well-motivated light particles are the axion, the axion-like particles and the hidden photons which are presented in this section.

2.2.1. Axions

For the electromagnetic interaction the combination of charge (C) and parity (P) is conserved. Contrary, this is not the case for the weak interaction, and the Lagrangian of the strong interaction also contains a term which allows CP violation [5]:

$$\mathcal{L}_{CP-v} = \frac{\alpha_s}{8\pi}\theta G^a_{\mu\nu}\tilde{G}^{a,\mu\nu}. \tag{2.13}$$

Here, G is the gluonic field strength and α_s is the coupling constant of the strong interaction. The fundamental constant θ determines the strength of the CP violation. Similar to α_s it has to be determined experimentally.
Since the neutron consists of quarks, the CP violation should be observed in it. The most prominent example for such an observation is the electric dipole moment of the neutron which would violate CP-symmetry [4]. It depends linearly on

$$\overline{\theta} \equiv \theta + \arg\,\det M, \tag{2.14}$$

with M as the quark mass matrix, and is of order

$$|d_n| \sim \frac{e}{m_n}\left(\frac{m_q}{m_n}\right)|\overline{\theta}| \sim 10^{-16}|\overline{\theta}|e \text{ cm}. \tag{2.15}$$

Here, m_n is the neutron mass, m_q the light-quark mass and e the electric unit charge. To date, d_n could not be observed and the current upper limit is

$$|d_n| < 2.9 \times 10^{-26} e \text{ cm}. \tag{2.16}$$

This corresponds to the following limit for $\overline{\theta}$:

$$|\overline{\theta}| \lesssim 10^{-10}. \tag{2.17}$$

As a matter of fact, $\overline{\theta}$ is in the range $-\pi \leq \overline{\theta} \leq +\pi$ and is therefore expected to be of order ~ 1 [19]. Thus, it is unnaturally small, being 10 orders of magnitude below the expectation. The lack of an explanation for this fact is called "strong CP problem".
The most prominent solution for this problem was proposed by Peccei and Quinn in 1977 [36]. They introduced a spontaneously broken global U(1) symmetry called "Peccei-Quinn symmetry" [19]. This way, $\overline{\theta}$ becomes dynamical and can relax spontaneously to 0. This relaxation is equivalent to a breaking of the PQ symmetry. Weinberg and Wilczek independently showed that a new pseudo-Nambu-Goldstone boson arises in the course of this breaking [37][38]. This new particle is called "axion".
The reason for the symmetry breaking is the axion's anomalous triangle coupling to gluons with the Lagrangian [19]

$$\mathcal{L} = \left(\overline{\theta} - \frac{\phi_A}{f_A}\right) \frac{\alpha_s}{8\pi} G^{a,\mu\nu} \tilde{G}^a_{\mu\nu}. \tag{2.18}$$

Here, ϕ_A is the axion field and f_A is the axion decay constant. Via non-perturbative effects the axion field gains a potential with a minimum at $\phi_A = \overline{\theta} f_A$. Inserting this minimum into equation (2.18) cancels the entire term, resulting in the conservation of CP-symmetry. The mentioned potential promotes the axion with a small but non-vanishing mass. This mass can be calculated by the dint of the couplings of the axion to quarks and gluons as well as to mesons and baryons. Expressed in terms of the properties of the light quarks and the pion, the mass is calculated as [5]

$$m_A = \frac{m_\pi f_\pi}{f_A} \frac{\sqrt{m_u m_d}}{m_u + m_d} \simeq 0.6\,\mathrm{meV} \times \left(\frac{10^{10}\mathrm{GeV}}{f_A}\right), \tag{2.19}$$

with $m_{u/d}$ as the mass of the up- and down-quark respectively, m_π as the mass of the pion and f_π as the decay constant of the pion. This shows that the mass of the axion is inversely proportional to its decay constant. It was primarily assumed that f_A is around the order of the electroweak symmetry-breaking scale $v_{weak} = 247\,\mathrm{GeV}$, but this "standard" axion was already excluded [19]. Instead, astrophysical calculations resulted in new limits of order $f_A \geq 10^9\,\mathrm{GeV}$ [39]. This corresponds to axion masses in the sub-eV range. For $f_A \gg v_{weak}$ new models were introduced, with the KSVZ-axion and the DFSZ-axion as the most prominent ones[40][41][42][43]. In both models the coupling of the axion to photons is described by the Lagrangian

$$\mathcal{L}_{A\gamma\gamma} = -\frac{1}{4} g_{A\gamma} \phi_A F_{\mu\nu} \tilde{F}^{\mu\nu} = g_{A\gamma} \phi_A \vec{E} \cdot \vec{B}, \tag{2.20}$$

with F as the electromagnetic field strength and $\vec{E}$ and $\vec{B}$ as the electric and magnetic field respectively. The coupling constant is denoted as

$$g_{A\gamma\gamma} = \frac{\alpha}{2\pi f_A}\left(C_{A\gamma} - \frac{2}{3}\frac{m_u + 4m_d}{m_u + m_d}\right) \sim 10^{-13}\,\mathrm{GeV}^{-1}\left(\frac{10^{10}\,\mathrm{GeV}}{f_A}\right), \tag{2.21}$$

with α as the fine structure constant. The model dependent dimensionless parameter $C_{A\gamma}$ possesses a value of 8/3 in the DFSZ model and a value of 0 in the KSVZ model [19].
The Lagrangian in equation (2.20) describes a coupling to two photons. One of these photons can be provided by one of the two involved fields ($\vec{E}$ and $\vec{B}$) as a virtual photon. The production of an axion (or a similar particle) via such a virtual photon is called "Primakoff effect". In analogy, the conversion of an axion to a photon in an external field is called "inverse Primakoff effect". Despite the fact that the coupling constant is rather small, the coupling of axions to two photons can occur with a measurable frequency in the presence of a sufficiently strong external field. Given that the axion exists, this occurs often in astrophysical environments and, in addition, it is possible to prepare laboratory experiments, as described in section 2.3 [5].

2.2.2. Axion-like particles

Aside from the Peccei-Quinn symmetry further possible global U(1) symmetries exist. A breaking of these symmetries results in further pseudo-Nambu-Goldstone bosons. These particles are called "axion-like particles" (ALPs) and represent a generalization of the axion. Compared to the axion whose mass and coupling to Standard Model photons is depending on f_A, the ALPs are much less constrained, with their mass and coupling as independent parameters [39]. This also means that their possible parameter space is much larger than the one of the axion. Another difference between axions and ALPs is the fact that there is no guaranteed non-zero coupling to photons for generic ALPs [4]. However, there do exist ALPs which are coupled to two photons corresponding to the following Lagrangian [7]:

$$\mathcal{L} = -\frac{1}{4}F_{\mu\nu}F^{\mu\nu} + \frac{1}{2}\partial_\mu\phi\partial^\mu\phi - \frac{1}{2}m_\phi^2\phi^2 - \frac{g_{\phi\gamma\gamma}}{4}\phi F_{\mu\nu}\tilde{F}^{\mu\nu}. \tag{2.22}$$

Here, F is the photon field strength, $\tilde{F}$ is the dual field strength, ϕ and m_ϕ are the ALP field and the ALP mass and $g_{\phi\gamma\gamma}$ is the coupling constant.
Axions and ALPs are not only motivated by the search for a solution for the strong CP problem but also by string theory. They both arise generically in the compactifications of the six extra spatial dimensions. This way, multiple ALP candidates with masses evenly distributed in logarithmic scale are suggested by string theory [5]. However, various known mechanisms which remove a part of these suggested candidates from the low-energy spectrum exist. The remaining particles not affected by these mechanisms can be considered as potential WISPs.

2.2.3. Hidden photons

Another type of WISPs are the "hidden photons" (HPs). These are the gauge bosons of additional U(1) gauge groups appearing in string theory compactifications. Although called photons, they are not necessarily massless. Instead, it is possible that they obtain a mass via the Higgs or the Stückelberg mechanism. For both cases the potential mass ranges between sub-eV and GeV [39]. This leads to a possible distinction of two types of HPs with the HP mass as the deciding factor. HPs with masses $m_{\gamma'} > 1\,\mathrm{MeV}$ are theoretically capable of decaying into two electrically charged Standard Model particles, for example into e^+e^-, $\mu^+\mu^-$ or $\pi^+\pi^-$. It is also possible for the HPs to decay into "hidden particles", given that those are existing, which for their part could decay into Standard Model particles. In contrast, HPs with masses $m_{\gamma'} < 1\,\mathrm{MeV}$ are not capable to decay into such particles due to their low mass. Instead, they can decay into three photons, but this process is much slower than the other ones [39].
Some of the HP U(1) gauge groups may remain unbroken down to very small energy scales. If this is the case, the main interaction of HPs with the Standard Model is the kinetic mixing with ordinary photons. The Lagrangian of this mixing is the following one [7]:

$$\mathcal{L} = -\frac{1}{4}F_{\mu\nu}F^{\mu\nu} - \frac{1}{4}\tilde{X}_{\mu\nu}\tilde{X}^{\mu\nu} - \frac{\chi}{2}F_{\mu\nu}\tilde{X}^{\mu\nu} + \frac{m_{\gamma'}^2}{2}\tilde{X}_\mu\tilde{X}^\mu + J^\mu A_\mu. \tag{2.23}$$

Here, $\tilde{X}^\mu$ and $\tilde{X}^{\mu\nu}$ denote the hidden photon and its field strength, A^μ and $F^{\mu\nu}$ denote the ordinary photon and its field strength, J^μ is the ordinary electromagnetic current and χ is the dimensionless parameter quantifying the kinetic mixing. Fundamental extensions of the Standard Model typically predict values for χ between 10^{-3} and 10^{-12} [44][45][46]. The kinetic mixing term can be eliminated by a shift $\tilde{X}^\mu \to X^\mu - \chi A^\mu$. After performing this shift and dropping the terms of order $\sim \chi^2$ when convenient, the following Lagrangian is obtained:

$$\mathcal{L} = -\frac{1}{4}F_{\mu\nu}F^{\mu\nu} - \frac{1}{4}X_{\mu\nu}X^{\mu\nu} + \frac{m_{\gamma'}^2}{2}\left(X_\mu X^\mu - 2\chi A_\mu X^\mu + \chi^2 A_\mu A^\mu\right) + J^\mu A_\mu \tag{2.24}$$

At low masses, the kinetic mixing results in HP $\rightleftarrows$ photon oscillations, similar to the neutrino oscillations. This enables various possible experimental setups for HP searches, which are partly described in the next section. For the specific values $m_{\gamma'} \sim 100\,\mathrm{keV}$ and $\chi \sim 10^{-2}$, the oscillation mechanism can generate a HP energy density sufficiently high for the HPs to account for the entire dark matter [39].
Contrary to axions and ALPs, HPs do not require an external magnetic field to interact with Standard Model particles. On the one hand, this allows detection experiments without big magnets, which are easier to design and arrange; on the other hand, it enables experiments searching for axions and ALPs to simultaneously search for HPs without further adjustments to the already designed setup.

2.3. WISPy experiments

As a result of the WISP-photon coupling, direct experimental searches for WISPs are possible. The required WISP source can either be laboratory based or of astrophysical or cosmological origin. The latter ones offer the advantage of a great number of particles, but hold the disadvantage of the necessity of knowing the relevant characteristics of the particles and their environment [5].
Since the mass of the WISPs is small and their interactions with photons are weak, the WISPy experiments are executed at the limits of low energy and high intensity. Therefore, the detection of the coupling requires for example high intensity lasers, high magnetic fields or measurement devices in the radio frequency range. This is in contrast to most other experiments of modern particle physics which are executed at the limits of high energy, with particle accelerators as the most prominent examples [5].
The following section presents selected WISPy experiments. Haloscopes and helioscopes are introduced as examples for sources with astrophysical and cosmological origin respectively. The laboratory based sources are covered by "Light shining through a wall" (LSW) experiments. These experiments are sensitive directly to the coupling strength, whereas the previous ones are sensitive to the product of the flux of the WISPs and the coupling strength. In addition, several experiments with different approaches are mentioned but not discussed in detail.

2.3.1. Haloscopes

Haloscopes are, as implied by their name, experiments searching for WISPs accounting for the galactic halo of dark matter and hence experiments with cosmological sources. Since the Earth is part of this halo, it is hypothetically possible that WISPs convert into photons anywhere on Earth via the inverse Primakoff effect or via oscillations between hidden photons and common photons. These photons can then be detected. Since their frequency is only depending on the mass of the WISPs, the photons can be assumed to be monochromatic [5]. They are detected in cavity resonators with eigenmodes in the microwave range. If the photon frequency matches the eigenmode of the cavity, the signal will be intensified resonantly. Based on this principle, by tuning the eigenmodes, for example via mechanical means, a great range of WISP masses can be explored with haloscopes [4].
Sikivie was the first to propose haloscopes as experiments for the search for axions in 1983 [47]. From that time onward, multiple experiments were planned and started, with first ones executed at the Brookhaven National Laboratory and the University of Florida. The largest and most sensitive cavity haloscope is ADMX which is currently located in Washington. In the first phase ADMX explored the mass range 1.9 - 3.7 µeV, and the planned second phase aims for the wider range 2 - 40 µeV [48]. Furthermore, a branch

experiment called ADMX-HF is located at the Yale University. In this already running experiment Josephson parametric amplifier are additionally used to search for axions with masses $m > 20\,\mu\text{eV}$ [49]. For lower WISP masses, WISPDMX is the first experiment which is enhanced resonantly in the range 0.8 - 2.0 μeV. This experiment is located in Hamburg and currently explores the mentioned range for the HP case, whereas future measurements for the ALPs case are already planned [50]. Aside from these "classical" cavity haloscopes, there are also proposed experiments with additional features. Prominent examples are the dielectric cavity haloscope called MADMAX [51] and BRASS in Hamburg, which is the topic of this thesis and of [52].

2.3.2. Helioscopes

Helioscopes are experiments searching for WISPs produced in the sun, which is an example for an astrophysical WISP source. It is hypothetically possible that WISPs are produced in stars via the Primakoff effect. If this is the case, it should be also possible that these WISPs convert into photons via the inverse Primakoff effect in a magnetic field on Earth. These photons have an energy of about 0.1 - 10 keV and are thus x-ray photons. So the basic idea is in analogy to the haloscopes, but the big difference is the absence of a resonator. Since the WISPs produced in the sun are not monochromatic, a resonator would be almost useless and a search for a specific frequency, whose signal could be intensified, would not be sensible [3]. Instead, the probability of a positive signal gets enhanced if the experiment is orientated towards the sun. For this purpose, sun tracking methods were invented such that the experiment gets dynamic and can "follow" the movement of the sun. For every new generation of experiments new tracking methods are introduced to improve the results [39].
The first helioscope searching for axions was started at the Brookhaven National Laboratory in 1992 with just a stationary magnet [53]. The first dynamic experiment was the Tokyo Axion Helioscope which additionally used a stronger magnet and achieved a background three orders of magnitude lower than the previous helioscope [54][55]. The most sensitive experiment of the third generation of helioscopes is the CAST experiment at CERN, which was started in 2003 and still gets expanded and improved. In the latest run, CAST delivered the best limit to the photon-axion coupling strength to date [56]. However, there is one big disadvantage shared by all experiments of the first three generations. They use magnets which were originally designed for different purposes, e.g. the LHC test magnet used by CAST. This limitation gets removed in the fourth generation of helioscopes, given that the planned IAXO experiment will use a specifically designed magnet. By means of this new magnet and further adjustments, IAXO aims for improving the sensitivity to axion signals by over five orders of magnitude compared to CAST in the mass range up to 0.25 eV [57].

Most helioscopes focus on the search for axions and ALPs and only a few search for hidden photons simultaneously. Nevertheless, there are also helioscopes without magnetic fields solely searching for HPs. One example of such an experiment is SHIPS in Hamburg. SHIPS ran until 2015 and is still the most sensitive experiment for the search for transversely polarized HPs [58].

2.3.3. LSW experiments

The LSW experiments are laboratory based experiments first proposed in 1982 in the context of paraphotons [59]. A few years later the principle was also introduced to the search for axions [60][61]. The idea behind the LSW experiments is the following: a brilliant laser is directed towards an opaque obstacle (the "wall") with a detector behind it. If a photon of the laser beam converts into a WISP in front of the obstacle, this WISP can pass the obstacle due to the small interaction probability, convert back into a photon behind the obstacle and then be detected by the detector. Given a sufficient shielding against other photon sources, a positive signal at the detector would therefore be an evidence for a WISP-photon conversion. This uncomplex setup is sufficient enough to search for hidden photons and, with a present magnetic field, also for axions and ALPs. A detailed discussion of the LSW theory and additional reviews can be found in [4] and [62]. The first LSW experiments were executed in the early 1990's [39]. The second generation of LSW experiments was built at multiple locations, for example BMV in Toulouse, OSQAR at CERN, GammeV at Fermilab, LIPPS at Jefferson Lab or ALPS-I at DESY [3]. The highest sensitivity of the mentioned experiments was obtained by ALPS-I, which provided the best exclusion limits in the meV range [63]. Nevertheless, this second generation was inferior compared to haloscopes and helioscopes both for the HP and the axion and ALPs case. The planned ALPS-II experiment of the third LSW generation aims to change this situation. ALPS-II is currently constructed in two stages and will be the first LSW experiment using a regeneration cavity to resonantly enhance the probability of the back conversion of photons. It will search for WISP masses below 1 meV and aims to perform the most sensitive searches for HPs with masses $m_{\gamma'} > 5 \times 10^{-5}\,\mathrm{eV}$ [64].
It should be noted that the disadvantage of the lesser sensitivity is compensated by the hypothetical possibility to control the WISP production as well as by the independence of astrophysical and cosmological assumptions. This offers the chance for independent fundamental research.

2.3.4. Additional experiments

The presented haloscopes, helioscopes and LSW experiments are all based on the conversion of WISPs into photons and vice versa. They are therefore examples for the experiments called “photon regeneration experiments”. Aside from these, further WISPy experiments based on other principles exist. Moreover, these experiments deal not only with axions, ALPs and HPs, but instead also with various WISPs not mentioned in this thesis, for example the “chameleons”. For the sake of completeness, a selection of these experiments is listed below without further discussion. For detailed information see the given references.

- Fifth force experiments [4][19]
- Laser polarization experiments [4][19]
- Afterglow experiments [4][39]
- Electron fixed-target and proton fixed-target experiments [39]
- Proton and electron-positron collider [39]
- Satellite based experiments [39]

2.4. Magnetostatics

For the conversion of axions and ALPs into Standard Model photons a magnetic field is required. To be able to chose a magnetic configuration creating a field fitting to the purposes of the experiment, some basic principles of magnetostatics need to be understood. This section highlights a selection of topics important in the context of this thesis. Unless otherwise noted, the content of this section is based on the information in [65].

2.4.1. Dia-, para- and ferromagnetism

There are in principle three basic possibilities for materials to behave inside an external magnetic field. The paramagnetism and the ferromagnetism describe materials whose magnetic moments orientate themselves parallel to the external field. These two types differ in the magnitude of the resulting magnetization. Ferromagnetic materials possess magnetizations multiple orders of magnitude higher than paramagnetic materials. Contrary, the diamagnetism describes materials whose magnetic moments orientate themselves opposite to the external field.
Every elementary particle of a material can be assigned with an elementary magnetic dipole moment. The total magnetization of a material is a superposition of these magnetic moments. Since the ones of nuclear spins are negligible small, only the magnetic moments of the electron spins are relevant for the macroscopic magnetization. In a pair of electrons occupying the same orbit the electron spins are opposite and so are the magnetic dipole moments of said electrons. Therefore, the magnetic moment of paired electrons is cancelled out and the magnitude of the magnetization depends on the unpaired electrons. A material consisting solely of paired electrons shows a diamagnetic behaviour.
Without the presence of an external magnetic field the elementary dipole moments are in principle each directed randomly. However, even without such an external field, ferromagnetic materials possess small areas in which all the dipole moments are orientated in parallel. These areas are called “Weiss domains” and are separated by the so-called “Bloch walls”. These domains are in turn directed randomly. The creation of Weiss domains is possible due to the so called “exchange interactions” between the electron spins, which are based on the Pauli principle. Caused by these interactions, the spins stabilize each other in their parallel orientation. If an external field is then applied to the material, its dipole moments gradually align with the field such that the Weiss domains orientated parallel to the field get bigger. Moreover, even after switching off the external field, most of the dipole moments maintain their direction due to the exchange interactions. Therefore, the material stays magnetized, thus creating its own field, resulting in a permanent magnet. To demagnetize a permanent magnet, it has to be energized sufficiently so that the thermal energy of the electrons is higher than the exchange interactions. If this is the case, the parallel orientation of the electron spins gets cancelled. This can be achieved by applying

an opposite external field, via commotions or by heating the magnet up. There are two material-dependent threshold temperatures in this context. The first one is the maximum working temperature $T_{\max}$. Up to this temperature the magnetization of the magnet remains constant. If heated above this threshold, the magnetization starts to decrease. The second threshold is the Curie temperature T_C, above which the magnet changes from ferromagnetic to paramagnetic behaviour. This change can be reversed by cooling the material down again.
The dipole moments of paramagnetic materials do not form Weiss domains. In analogy to the ferromagnetic materials, they align themselves inside a present external magnetic field, but to a lesser extent due to smaller exchange interactions. Moreover, since these interactions are much smaller than the thermal energy of the electrons, the dipole moments orientate themselves randomly again if the external field is switched off.

2.4.2. Hysteresis

Due to the exchange interactions and the creation of Weiss domains, ferromagnetic materials show a hysteretic behaviour. This means that the magnitude of the magnetic field strength does not only depend on the external magnetic field but also on its past state.
If a very small magnetic field H surrounding a demagnetized magnet is steadily powered up, the elementary magnetic dipole moments will gradually align themselves with the external field and hence the magnetic flux density B of the magnet increases. After an early rapid increase, B asymptotically reaches a saturation value B_s since all dipoles are orientated in parallel. A further increase of H only results in an insignificant increase of B. Now, if H is steadily reduced, the dipoles do not re-orientate themselves the same way as they aligned themselves before. Instead, B decreases slowly and settles at a non-zero value if H is reduced to zero. This value is called "remanence" (B_r). To further reduce B, it is necessary to apply an opposite magnetic field $-H$. The value of this field at which B reduces to zero is called "coercivity" ($-H_c$). Again, a further increase of $-H$ results in B reaching saturation, now also in opposite direction ($-B_s$). The same way as before, steadily decreasing $-H$ leads to a slow decrease of $-B$, traversing the remanence $-B_r$ and, if H is again applied in the initial direction, zero. If H is then increased sufficiently, B again reaches B_r. The graphical representation of this relation between H and B is called hysteresis. Two examples are given in figure 2.6.
If the exchange interactions inside a material are strong, a high energy is necessary to change the direction of the individual magnetic moments. If this is the case, the hysteresis of this material possesses a high remanence and a high coercivity and the material is called "magnetically hard". Contrary, materials with low values for B_r and H_c are called "magnetically soft". Permanent magnets should possess a high remanence to retain their magnetization. Therefore, they should be made of magnetically hard materials.

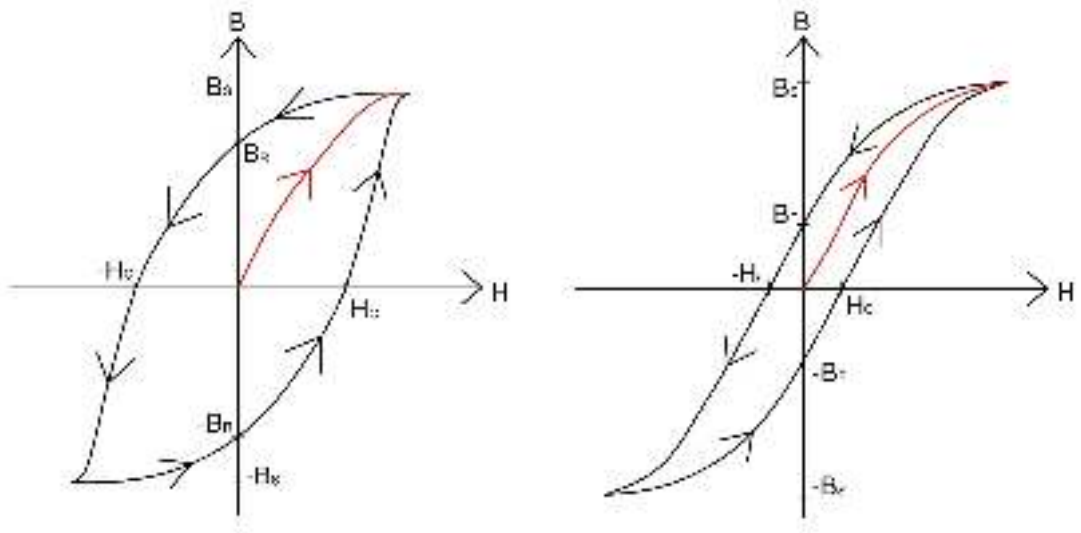

(a) magnetically hard material (b) magnetically soft material

Figure 2.6.: Two exemplary hystereses. The red line indicates the initial curve of the yet unmagnetized material and is therefore called "initial magnetization curve". If the magnetic field H increases steadily, the magnetic flux density B also increases up to a saturation value B_s. If H decreases steadily after this, B decreases much slower and settles at a value B_r called remanence when H reaches zero. To reduce B to zero, an opposite field $-H$ has to be applied and increased up to the value $-H_c$, called coercivity. If $-H$ is further increased, the flux density also changes its direction and reaches the saturation $-B_s$. This course is displayed as the upper black lines, as denoted by the arrows. The lower black lines display the "return path" with conditions being equal, except for the respective signs of H and B. Since the hystereses are point symmetric to the origin, B_s and $-B_s$, H_c and $-H_c$ and B_r and $-B_r$ also only differ in their respective sign but not in their absolute value. If the remanence and coercivity of a material are high, as shown in figure (a), the material is called magnetically hard. Contrary, if they are low, the material is called magnetically soft. The images are based on the ones in [65].

The product of the remanence and the coercivity of a material (multiplied with an additional factor < 1) is called "energy product" $BH_{\max}$ [66]. It is an indicator of the maximum density of magnetic energy stored into the magnet and thus for the maximum work that can be performed by the magnet. It is therefore used as a quality factor grading permanent magnets. It can also be determined graphically using the hysteresis curve of the material. The value of the maximum area a rectangle located solely in the second quadrant can enclose is equal to the energy product.

2.4.3. Neodymium magnets

The currently strongest permanent magnets at ambient temperature are made of an alloy of neodymium, iron and boron in the form of $Nd_2Fe_{14}B$ [66]. This composition was independently developed by Sumitomo Special Metals [67] and General Motors [68] in 1984. One of the main motivations for this development were the high expenses of the predecessors of these neodymium magnets, namely the samarium-cobalt magnets. These are produced in the form of either $SmCo_5$ or Sm_2Co_{17} and are still the second strongest permanent magnets at ambient temperature. Considering that iron is cheaper than cobalt, neodymium is cheaper and more abundant than samarium and the rare earth content of neodymium magnets is relatively small, only adding up to 12% by volume, these magnets are more profitable than the samarium magnets [66].
One of the most important properties of $Nd_2Fe_{14}B$ is its tetragonal crystal structure which possesses a high uniaxial magnetocrystalline anisotropy (see chapter 13.5 in [66] for a more detailed view). This means that the crystal magnetizes preferentially in the direction of one specific crystal axis and that it is difficult to change the magnetization direction. Therefore, the crystal possesses a high resistance to being demagnetized, i.e. a high coercivity, and a high remanence. The best neodymium magnets provide the following values [66]:

- $H_c \sim 2000\,\mathrm{kA/m} \sim 25\,\mathrm{kOe}$
- $B_r \sim 1.5\,\mathrm{T} = 15000\,\mathrm{G}$
- $BH_{\max} \sim 400\,\mathrm{kJ/m^3} \sim 50\,\mathrm{MGOe}$
- $T_{\max} = 80\,^\circ\mathrm{C} \quad \text{and} \quad T_C = 310\,^\circ\mathrm{C}$

The average energy product adds up to $BH_{\max} \sim 320\,\mathrm{kJ/m^3} \sim 40\,\mathrm{MGOe}$. In contrast, the samarium magnets only reach on average an energy product of $BH_{\max} \sim 200\,\mathrm{kJ/m^3} \sim 25\,\mathrm{MGOe}$. However, since their threshold temperatures are much higher, with $T_C = 750\,^\circ\mathrm{C}$ and $T_{\max} = 300\,^\circ\mathrm{C}$, they surpass the neodymium magnets at high temperatures and are the strongest permanent magnets in the range of $310\,^\circ\mathrm{C} \leq T \leq 750\,^\circ\mathrm{C}$.
There are two basic methods to produce neodymium magnets. The commonly applied method is the sintering process. In this process, the raw materials are first melted, molded and cooled to form blocks. These are then pulverized and milled, after which the grains of the powder are aligned via magnetic pressing. This leads to a partially dense compact which can then be sintered. In a final step, the resulting dense blocks are further heat treated and coated [69][70]. The second method is the bonded magnet process. This process starts with melt-spinning a ribbon of NdFeB. This ribbon gets pulverized, mixed with a polymer and then finally molded into bonded magnets [70][71]. While the micro-crystalline sintered magnets provide higher magnetic flux intensities, the nanocrystalline bonded ones can be formed into more complex shapes.

An undesired property of the neodymium magnets is their vulnerability to corrosion. This can lead to various forms of deterioration and material losses, including spalling and crumbling. These types of corrosion especially affect the sintered neodymium magnets. To reduce the amount of losses, most magnets are covered with a protective coating. This typically consists of nickel, a mixture of nickel and cobalt or epoxy [72].

2.4.4. Hall effect

One possibility to measure a magnetic field is via a probe using the Hall effect. This effect was discovered by Edwin Hall in 1879 [73]. It describes the appearance of a voltage at an electric conductor in a perpendicularly orientated magnetic field.
The current of an electric conductor consists of moving charge carriers, which can either be electrons, ions or holes. Without an external magnetic field, these carriers take a straight path across the conductor. Contrary, in the presence of a magnetic field with non-zero components perpendicular to the direction of the current, the carriers are deflected and driven onto a curved path due to the acting Lorentz force. This results in a separation of charge inside the conductor and hence in an arising voltage called "Hall voltage". The separation of charge naturally also generates an electric field which counters the Lorentz force after reaching a threshold value. This way, a steady electric potential is created as long as the strengths of the current and the magnetic field are constant. A sketch of this effect is shown in figure 2.7.
The Hall voltage U_H is directly proportional to the strength of the external magnetic field:

$$U_H = \frac{A_H \cdot I}{d} \cdot B. \tag{2.25}$$

Here, I is the strength of the current and d the thickness of the conductor parallel to B. The parameter A_H is called "Hall coefficient" of the conductor material which can be calculated as

$$A_H = \frac{1}{n \cdot q}, \tag{2.26}$$

with n as the charge carrier density and q as the charge of each carrier. Since materials with a high Hall coefficient provide a high sensitivity, most Hall probes are made of semiconductors with a low charge carrier density.
Contrary to various other methods of measuring magnetic fields, it is possible to measure constant fields with Hall probes. In addition, the measurement range is comparatively wide. Another advantage is the fact that Hall probes do not include magnetic material. Therefore, only a small but mostly negligible perturbation caused by the magnetic field of the electric current appears. Finally, three-dimensional and gradient measurements are possible if multiple probes are used. However, there are some disadvantages. The most relevant ones are the relatively small accuracy as well as the dependence on the environmental temperature. See [74] for further detail concerning the Hall probes.

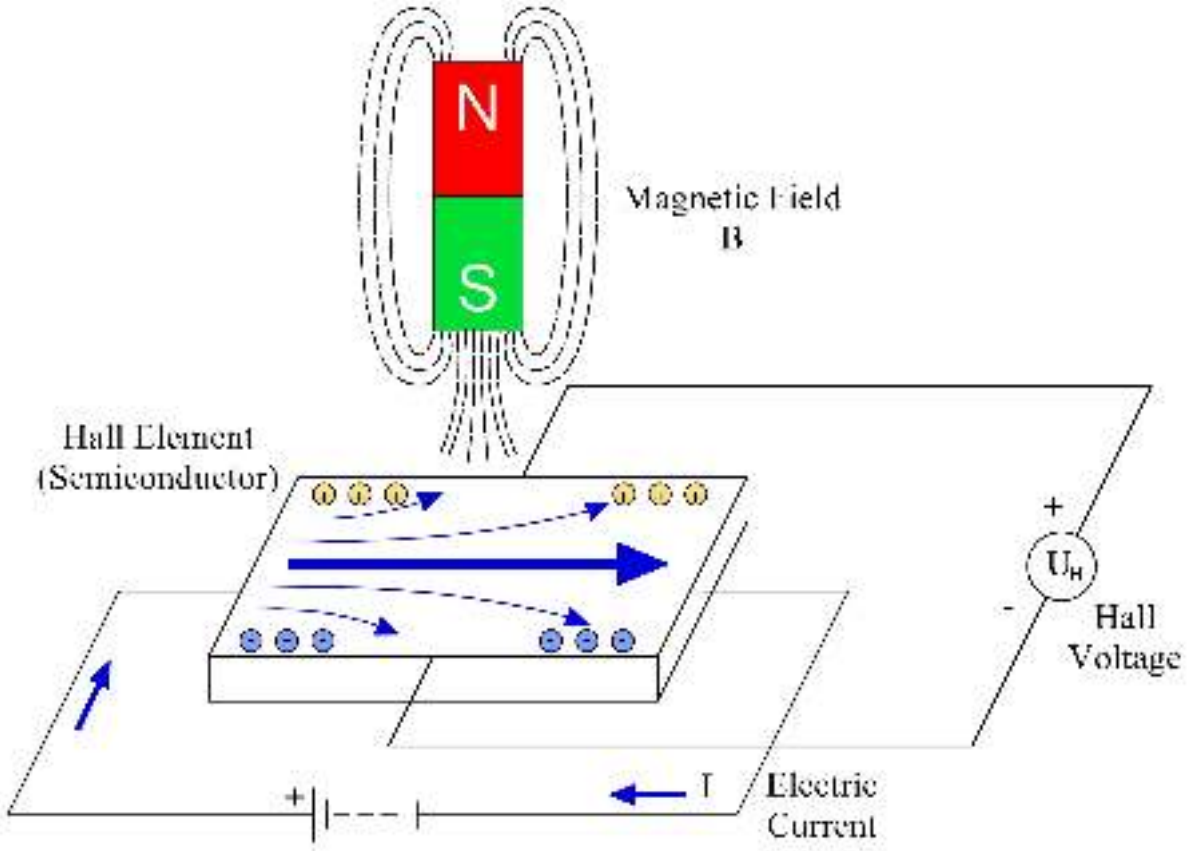

Figure 2.7.: A sketch of the principle of the Hall effect. The centred object (denoted as "Hall Element") is an electric semiconductor with a constantly flowing current I. Due to the presence of a magnetic field B which is perpendicular to the direction of the current, the charge carriers are deflected by the acting Lorentz force perpendicularly both to the current direction as well as to the magnetic field direction. They are driven onto a curved path leading to the edges of the semiconductor (thin blue arrows). This results in a separation of charge inside the conductor (light blue and orange circles). Due to this separation, a voltage U_H appears between the edges which can then be measured to calculate the magnetic field strength. Moreover, an electric field arises between the edges which is countering the Lorentz force such that the following charge carriers take a straight path across the semiconductor (thick blue arrow). Therefore, the voltage remains constant as long as the current strength and the magnetic field strength stay unchanged.

3. The BRASS experiment

BRASS ("Broadband Radiometric Axion SearcheS") is a new type of haloscope searching for WISPy dark matter via a dish antenna. It is based on the assumption that reflective surfaces can convert WISPs into electromagnetic radiation and was first proposed in [7]. The following chapter recaps this publication and outlines the theoretical basis as well as the potential and the limitations of the planned experiment.

3.1. Theoretical basis

Hidden photons

The starting point are the equations of motion for plane waves with frequency ω and momentum k:

$$\left[(\omega^2 - k^2)\begin{pmatrix} 1 & 0 \\ 0 & 1 \end{pmatrix} - m_{\gamma'}^2 \begin{pmatrix} \chi^2 & -\chi \\ -\chi & 1 \end{pmatrix}\right]\begin{pmatrix} \mathbf{A} \\ \mathbf{X} \end{pmatrix} = \begin{pmatrix} 0 \\ 0 \end{pmatrix}. \tag{3.1}$$

Here, a suitable gauge choice offers $X^0 = A^0 = 0$, so that the dark matter solution is found with $k = 0$ and $\omega = m_{\gamma'}$ as

$$\left.\begin{pmatrix} \mathbf{A} \\ \mathbf{X} \end{pmatrix}\right|_{\mathrm{DM}} = \mathbf{X}_{\mathrm{DM}} \begin{pmatrix} -\chi \\ 1 \end{pmatrix} \exp(-i\omega t). \tag{3.2}$$

The vector field $\mathbf{X}_{\mathrm{DM}}$ is either directed uniformly, independent of the location in space, or randomly.
The energy density of the dark matter in the galactic halo is given by

$$\rho_{\mathrm{CDM,halo}} \sim \frac{0.3\,\mathrm{GeV}}{\mathrm{cm}^3}. \tag{3.3}$$

If hidden photons account for the entire dark matter in the halo, their energy density is given by

$$\rho_{\mathrm{HP}} = \frac{m_{\gamma'}^2}{2}\langle|\mathbf{X}_{\mathrm{DM}}|^2\rangle = \rho_{\mathrm{CDM,halo}} \sim \frac{0.3\,\mathrm{GeV}}{\mathrm{cm}^3}, \tag{3.4}$$

where $\mathbf{X}_{\mathrm{DM}}$ is only averaged if it is directed randomly. This energy density is in small part also present as a small oscillating ordinary electric field

$$\mathbf{E}_{\mathrm{DM}} = -\partial_0 \mathbf{A} = \chi m_{\gamma'} \mathbf{X}_{\mathrm{DM}}. \tag{3.5}$$

If averaged over a sufficiently large spatial volume, this corresponds to an electric field with an amplitude

$$\sqrt{\langle|\mathbf{E}_{\mathrm{DM}}|^2\rangle} \;=\; \chi\sqrt{2\rho_{\mathrm{CDM,halo}}} \;\sim\; 3.3\times10^{-9}\,\frac{\mathrm{V}}{\mathrm{m}}\left(\frac{\chi}{10^{-12}}\right)\left(\frac{\rho_{\mathrm{CDM,halo}}}{0.3\,\mathrm{GeV/cm^3}}\right) \tag{3.6}$$

and an oscillation frequency

$$f \;=\; \frac{m_{\gamma'}}{2\pi} \;=\; 0.24\,\mathrm{GHz}\left(\frac{m_{\gamma'}}{\mu\mathrm{eV}}\right). \tag{3.7}$$

If there are no boundaries present, the electric fields of the HP dark matter, both visible and hidden, have the following form:

$$\left.\begin{pmatrix}\mathbf{E}(\mathbf{x},t)\\ \mathbf{E}_{\mathrm{hid}}(\mathbf{x},t)\end{pmatrix}\right|_{\mathrm{DM}} \;=\; -m_{\gamma'}\mathbf{X}_{\mathrm{DM}}\begin{pmatrix}-\chi\\ 1\end{pmatrix}\exp(-i\omega t), \tag{3.8}$$

with

$$\omega \;=\; m_{\gamma'}. \tag{3.9}$$

Now, if there exists an infinite plane mirror at $x=0$, perfectly reflecting the frequencies of interest, the following boundary condition appears for the components parallel to the plane:

$$\mathbf{E}_{\parallel}(x=0,y,t) \;=\; 0. \tag{3.10}$$

Since the mirror, consisting of ordinary matter, can only affect the ordinary electric field, this boundary condition is fulfilled on the right hand side by an additional outgoing plane wave with the same frequency:

$$\begin{pmatrix}\mathbf{E}\\ \mathbf{E}_{\mathrm{hid}}\end{pmatrix}_{\mathrm{out}} \;=\; \mathbf{E}_{\mathrm{DM}\parallel}\exp(-i(\omega t-\mathbf{kx}))\begin{pmatrix}1\\ \chi\end{pmatrix}, \tag{3.11}$$

with

$$\mathbf{k} \;=\; \omega\;(1,0,0)^{\mathbf{T}}. \tag{3.12}$$

This wave is an almost ordinary electromagnetic wave and is emitted perpendicularly to the mirror's surface. Microscopically, this can be explained as follows: the electrons on the surface of the mirror react to the electric field of the HP and start to oscillate. This oscillation causes the outgoing wave which has the same amplitude as the HP field, an opposite phase and a polarization lying within the surface plane. Its magnitude is depending on the dark matter density:

$$\sqrt{\langle|\mathbf{E}_{\mathrm{DM}\parallel}|^2\rangle} \;=\; \chi\;\sqrt{2\rho_{\mathrm{DM}}}\;\alpha, \tag{3.13}$$

with α depending on the vector field $\mathbf{X}_{\mathrm{DM}}$. If it is directed uniformly, α is $|\cos(\theta)|$, otherwise it is $\sqrt{2/3}$. Here, the angle θ lies between the HP field and the plane. Added to the dark matter field from equation (3.8), this wave fulfils the boundary condition at $x = 0$, i.e. on the mirror:

$$\begin{aligned}\begin{pmatrix} \mathbf{E} \\ \mathbf{E}_{\mathrm{hid}} \end{pmatrix}_{\mathrm{total}\parallel} &= \mathbf{E}_{\mathrm{DM}\parallel} \left[\begin{pmatrix} 1 \\ \chi \end{pmatrix} \exp(-i(\omega t - \mathbf{kx})) + \frac{1}{\chi} \begin{pmatrix} -\chi \\ 1 \end{pmatrix} \exp(-i\omega t) \right]_{x=0} \\ &= \mathbf{E}_{\mathrm{DM}\parallel} \frac{1}{\chi} \begin{pmatrix} 0 \\ 1 \end{pmatrix}. \end{aligned} \tag{3.14}$$

Evaluated at a finite distance, this yields

$$\mathbf{E}(\mathbf{x}, t)_{\parallel} = \mathbf{E}_{\mathrm{DM}\parallel} \exp(-i\omega t)(\exp(i\mathbf{kx}) - 1). \tag{3.15}$$

On every point on the mirror an outgoing wave like this can be emitted perpendicularly to the mirror. Thus, to focus these waves, the mirror has to be curved. The simplest approach is to put the mirror on the surface of a spherical object like a dish antenna.
The size of the dish antenna is in principle arbitrary. An appreciated advantage occurs if the radius of the dish antenna is much larger than the wavelength of the outgoing wave, i.e. of the DM particle. In this situation diffraction effects are negligibly small so that the waves behave as given in ray optics. This way, the waves are best focused to the centre of the sphere where a broadband detector can then be placed and where the following power is concentrated:

$$P_{\mathrm{centre}} \approx A_{\mathrm{dish}} \langle |\mathbf{E}_{\mathrm{DM}\parallel}|^2 \rangle = \langle \alpha^2 \rangle_{\mathrm{dish}} \, \chi^2 \rho_{\mathrm{CDM}} A_{\mathrm{dish}}. \tag{3.16}$$

A sketch of such an experimental setup is given in figure 3.1.

Axion-like particles

As mentioned before, ALPs couple to photons only in a present magnetic field. In this case the equations of motion are

$$\left[(\omega^2 - k^2) \begin{pmatrix} 1 & 0 \\ 0 & 1 \end{pmatrix} + \begin{pmatrix} 0 & -g_{\phi\gamma\gamma}|\mathbf{B}|\omega \\ -g_{\phi\gamma\gamma}|\mathbf{B}|\omega & m_\phi^2 \end{pmatrix} \right] \begin{pmatrix} \mathbf{A}_{\parallel} \\ \phi \end{pmatrix} = \begin{pmatrix} 0 \\ 0 \end{pmatrix}. \tag{3.17}$$

ALPs do not affect the components of the photon field which are perpendicular to the magnetic field. Hence the equations of motion only contain the parallel components $A_{\parallel}$. The solutions to these equations are similar to the solutions in the hidden photon case, replacing

$$\chi \to \frac{g_{\phi\gamma\gamma}|\mathbf{B}|}{m_\phi}. \tag{3.18}$$

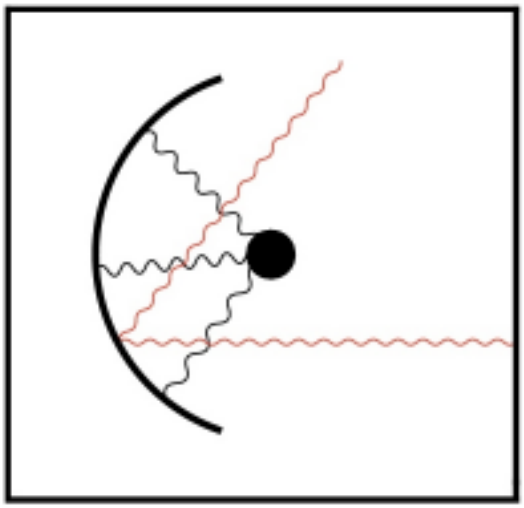

Figure 3.1.: Sketch of the principle of BRASS. Non-relativistic HPs and ALPs, which are mixing with SM photons, are converted into SM photons on the surface of a spherical dish antenna. These monochromatic photons (black) are emitted perpendicularly to the surface and are therefore focused in the centre of the sphere, where a broadband detector is placed (black dot). Photons from background sources (red) are typically focused in the focal point but not in the detector. From [7].

3.2. Potential and limitations

A resonant cavity experiment reaches a power output of

$$P_{\text{resonant cavity}} = \kappa\chi^2 m_{\gamma'}\rho_{\text{CDM}} Q V_{\text{cavity}} \mathcal{G}_0 (\alpha')^2, \tag{3.19}$$

with Q as the quality factor of the cavity, $\mathcal{G}_0$ as a geometrical factor encoding the overlap between the cavity mode and the dark matter field and κ as the coupling of the cavity mode to the detector, which should be ~ 1 for good coupling. Again, the factor α' depends on the vector field $\mathbf{X}_{\text{DM}}$. If it is directed uniformly, α' is $|\cos(\theta)|$, otherwise it is $\sqrt{1/3}$. A comparison of equation (3.16) to equation (3.19) shows that, neglecting $\mathcal{G}_0$, QV_{cavity} corresponds to $A_{\text{dish}}/m_{\gamma'} \sim A_{\text{dish}}\lambda$. Hence the difference lies in the respective volume. On the one side there is the volume of the cavity (typically of the order $V_{\text{cavity}} \sim \lambda^3 \sim 1/m_{\gamma'}^3$), and on the other side there is an "effective" volume $V_{\text{dish,effective}}$ consisting of the area of the dish A_{dish} and the distance λ after which the WISP is basically converted.

A cavity experiment usually gains a $Q \sim 10^6$ enhancement due to the resonance. To compensate for the loss of this enhancement, the area of the dish antenna needs to be sufficiently large. This way, the dish can get an "effective" Q:

$$Q_{\text{eff}} \sim A_{\text{dish}}/\lambda^2 \sim 10^4 \left(\frac{A_{\text{dish}}}{1\,\text{m}^2}\right)\left(\frac{\lambda}{\text{cm}}\right)^{-2}. \tag{3.20}$$

One of the most important features of BRASS is that it is broadband. The revisable mass range is only depending on the mass range to which the detector is sensitive. The whole range can be tested, if the detector is sensitive enough, without the need to adjust the experiment. Contrary to this, cavity experiments, for example, need to slowly scan the mass range.
Another advantage of the experiment is shown in figure 3.1. While the radiation emitted as a result of the dark matter field is focused in the detector in the centre of the sphere, far-away background radiation is focused in the focal point which lies halfway between the detector and the spherical surface. It is, however, favoured to avoid this background radiation. For this purpose it is planned to put the whole experimental setup into a shielding box if possible. The problem that the shielding box itself could get excited and emit background radiation can be avoided by a fitting geometry. Since this radiation would be emitted perpendicularly as well, the geometry of the box can minimize the effect.

BRASS is limited by the following aspects:

- As mentioned before, the wavelength has to be much smaller than the size of the dish antenna. If this is the case, diffraction effects can be neglected and the dish focuses the wanted radiation effectively in the detector. For this to happen, the dish should possess a smooth surface and an approximately spherical shape on length scales of the wanted wavelengths.

- The surface of the dish has to be a good reflector, for example a mirror for the IR to UV range or a metal dish for the radio frequency range. Otherwise, the boundary condition of a vanishing electric field on the surface can not be provided.

- Aside from far-away background radiation there is also background radiation originating from thermal emission from the mirror surface. This radiation is on the one hand emitted isotropically, hence it will not be focused into the detector. On the other hand, it can be reduced by cooling the dish. Considering these two dilutions, there is a relative suppression of the order $A_{\text{detector}}/A_{\text{dish}}$.
  Note that contrary to the broad spectrum of background radiation, regardless of the origin, the signal of the wanted radiation would consist of a narrow peak. Hence it should be possible to distinguish the signal from the background.

These aspects limit the experiment to the following masses of HPs and ALPs:

$$m_{\gamma'} \gtrsim \text{few} \times 1\,\mu\text{eV}\left(\frac{\text{m}}{r_{\text{dish}}}\right), \tag{3.21}$$

$$m_{\phi} \gtrsim \text{few} \times 10^{-5}\,\text{eV}. \tag{3.22}$$

In the radio frequency range powers down to $P_{\text{det}} \geq 10^{-21}\,\text{W}$ can be detected. Considering this, equation (3.16) can be rewritten as

$$\chi_{\text{sens}} = 4.5 \times 10^{-14}\left(\frac{P_{\text{det}}}{10^{-23}\,\text{W}}\right)^{\frac{1}{2}}\left(\frac{0.3\,\text{GeV/cm}^3}{\rho_{\text{CDM,halo}}}\right)^{\frac{1}{2}}\left(\frac{1\,\text{m}^2}{A_{\text{dish}}}\right)^{\frac{1}{2}}\left(\frac{\sqrt{2/3}}{\alpha}\right), \tag{3.23}$$

where P_{det} is the detectable power output. Note that this power is in presence of background signals. With sufficient shielding it should be possible to even reach $P_{\text{det}} = 10^{-23}\,\text{W}$ and, although subject to technical challenges, perhaps $P_{\text{det}} = 10^{-25}\,\text{W}$. Measurements of frequencies between 1 and 20 GHz, which correspond to wavelengths between 30 and 1.5 cm, are least affected by background noise originating from sky brightness, which is dominated by the cosmic microwave background in this frequency range, with $T_{\text{sky}} \approx T_{\text{CMB}}$. Beyond this range, shielding becomes more important to sustain $P_{\text{det}} = 10^{-23}\,\text{W}$. At lower frequencies the sky brightness increases $\propto \lambda^{2.8}$ [75] whereas at higher frequencies the atmospheric H_2O and O_2 lines result in $T_{\text{sky}} > 100\,\text{K}$ [76].
The sensitivity can also be described with the detectable photon rate instead of the detectable power. This is for example reasonable at higher frequencies and changes equation (3.23) to

$$\chi_{\text{sens}} = 5.6 \times 10^{-12}\left(\frac{R_{\gamma,\text{det}}}{1\ \text{photon/s}}\right)^{\frac{1}{2}}\left(\frac{m_{\gamma'}}{\text{eV}}\right)^{\frac{1}{2}}\left(\frac{0.3\ \text{GeV cm}^{-3}}{\rho_{\text{CDM,halo}}}\right)^{\frac{1}{2}}\left(\frac{1\ \text{m}^2}{A_{\text{dish}}}\right)^{\frac{1}{2}}\left(\frac{\sqrt{2/3}}{\alpha}\right). \tag{3.24}$$

For both approaches, limits for the sensitivity are shown in figure 3.2.

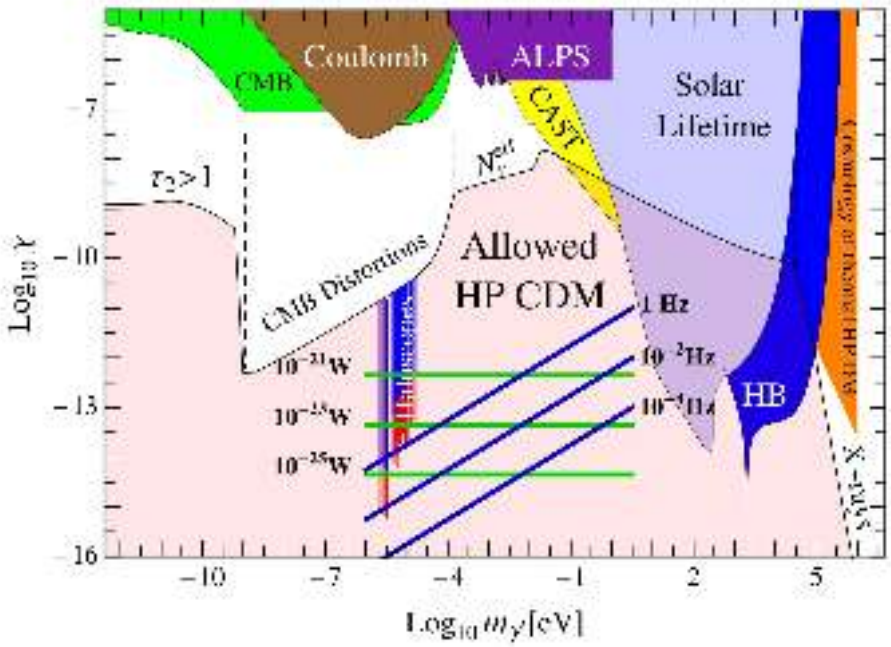

Figure 3.2.: The allowed parameter space for hidden photon cold dark matter (HP CDM) is shown in light red (see [4] for details). The various coloured regions are excluded by experiments and astrophysical observations not requiring HP CDM (see [5] and [77] for reviews). The lines represent the limits of the sensitivity of a dish antenna ($1\,\mathrm{m}^2$) search. The green lines correspond to a detector sensitive to 10^{-21}, 10^{-23} and $10^{-25}\,\mathrm{W}$ respectively and the blue lines correspond to a detector sensitive to 1, 10^{-2} and 10^{-4} photons per second respectively. From [7].

For the search for ALPs the sensitivities can be denoted in analogy to equations (3.23) and (3.24) as

$$g_{\phi\gamma\gamma,\mathrm{sens}} = \frac{3.6\times10^{-8}}{\mathrm{GeV}}\left(\frac{5\ \mathrm{T}}{\sqrt{\langle|\mathbf{B}_\parallel|^2\rangle}}\right)^{\frac{1}{2}}\left(\frac{P_{\mathrm{det}}}{10^{-23}\ \mathrm{W}}\right)^{\frac{1}{2}}\left(\frac{m_\phi}{\mathrm{eV}}\right)\left(\frac{0.3\ \mathrm{GeV\,cm^{-3}}}{\rho_{\mathrm{CDM,halo}}}\right)^{\frac{1}{2}}\left(\frac{1\ \mathrm{m}^2}{A_{\mathrm{dish}}}\right)^{\frac{1}{2}} \tag{3.25}$$

and

$$g_{\phi\gamma\gamma,\mathrm{sens}} = \frac{4.6\times10^{-6}}{\mathrm{GeV}}\left(\frac{5\ \mathrm{T}}{\sqrt{\langle|\mathbf{B}_\parallel|^2\rangle}}\right)^{\frac{1}{2}}\left(\frac{R_{\gamma,\mathrm{det}}}{1\ \mathrm{Hz}}\right)^{\frac{1}{2}}\left(\frac{m_\phi}{\mathrm{eV}}\right)^{\frac{3}{2}}\left(\frac{0.3\ \mathrm{GeV\,cm^{-3}}}{\rho_{\mathrm{CDM,halo}}}\right)^{\frac{1}{2}}\left(\frac{1\ \mathrm{m}^2}{A_{\mathrm{dish}}}\right)^{\frac{1}{2}}, \tag{3.26}$$

where $\langle|\mathbf{B}_\parallel|^2\rangle$ is the average value of the squared magnetic field components parallel to the dish antenna.

Aside from the properties of the detector there are two alterable parameters of the experiment itself which determine the sensitivity to the coupling constant $g_{\phi\gamma\gamma}$, namely the size of the dish area A_{dish} and $\langle|\mathbf{B}_\parallel|^2\rangle$. The product of these two parameters is inversely

proportional to the value of the coupling constant to which the experiment is sensitive. Hence the experimental setup should be designed such that this product gets maximized. Similarly to the HP case, limits for the sensitivity can be found in figure 3.3.

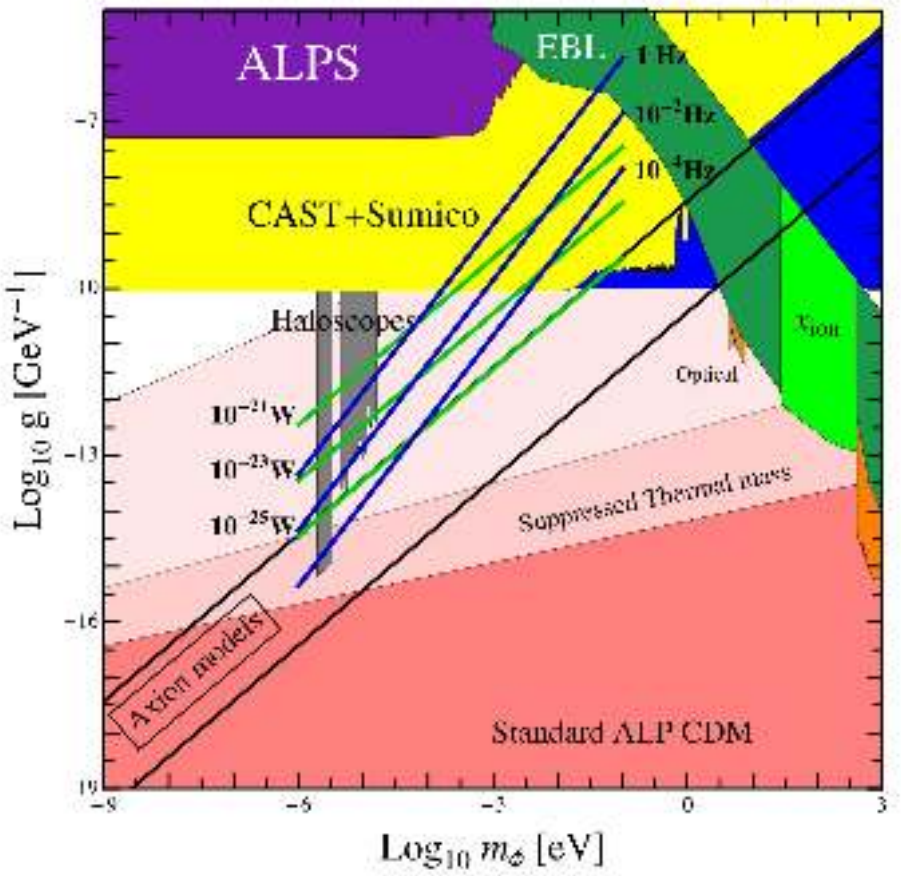

Figure 3.3.: The allowed parameter space for axion-like particle cold dark matter (ALP CDM) is shown in various shades of red (see [4] for details). The various coloured regions are excluded by experiments and astrophysical observations not requiring ALP CDM (see [5] and [77] for reviews). The lines represent the limits of the sensitivity of a dish antenna ($1\,\mathrm{m}^2$ in a magnetic field of $5\,\mathrm{T}$) search. The green lines correspond to a detector sensitive to 10^{-21}, 10^{-23} and $10^{-25}\,\mathrm{W}$ respectively and the blue lines correspond to a detector sensitive to 1, 10^{-2} and 10^{-4} photons per second respectively. From [7].

In both figures 3.2 and 3.3 it is clearly shown that BRASS offers the exploration of huge areas in the parameter spaces of hidden photons and axion-like particles respectively. While in the ALPs case, a rather large part of this area is already excluded by other experiments and observations, in the HP case the biggest part of this area is not yet studied. BRASS should, however, also be beneficial for the ALPs search since lower ALPs masses can be tested with less effort than in cavity experiments.

3.3. Halbach structure

In 1973 Mallinson first mentioned the theoretical indication of a "one-sided flux" generated by a specific pattern of magnetizations [78]. He described a planar structure whose magnetization is a superposition of two sinusoids in quadrature:

$$m_x = m_0 \cdot \sin(kx) \tag{3.27}$$

$$m_y = m_0 \cdot \cos(kx), \tag{3.28}$$

with k as the wavenumber and $m_z = 0$. The resulting flux of such a pattern differs depending on the side of the structure. On one side the flux duplicates and on the other side the flux completely vanishes[1]. This principle is shown in figure 3.4.

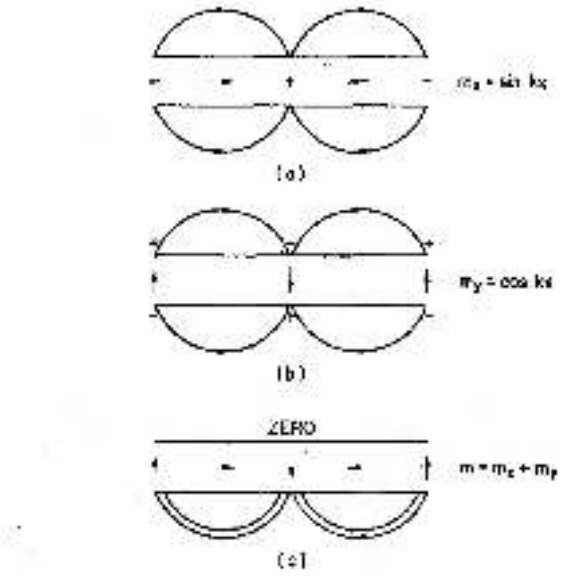

Figure 3.4.: The principle of Mallinson's one-sided flux. All three sketches show a magnetized tape and the magnetic field lines. Sketch (a) corresponds to a longitudinally magnetized tape and sketch (b) corresponds to a transversely magnetized tape. In sketch (c) the magnetization is a superposition of both previous ones so that consecutive magnetization vectors are rotated clockwise by 90°. This results in a duplicated magnetic field on the lower side, where the field lines of (a) and (b) proceed in the same direction, and a vanishing field on the upper side, where the field lines proceed in opposite directions. From [78].

In 1980 Halbach first built a similar structure with this effect [8]. His quadrupole consisted of 16 trapezoidal pieces with 5 different magnetization orientations with respect to the axis of the trapezoid and was meant to focus particle accelerator beams. A scheme of this quadrupole is shown in figure 3.5. Any structures which realize this effect are since then called "Halbach arrays".

[1] This corresponds to the ideal case. In practice, a small field is still present on the vanishing side.

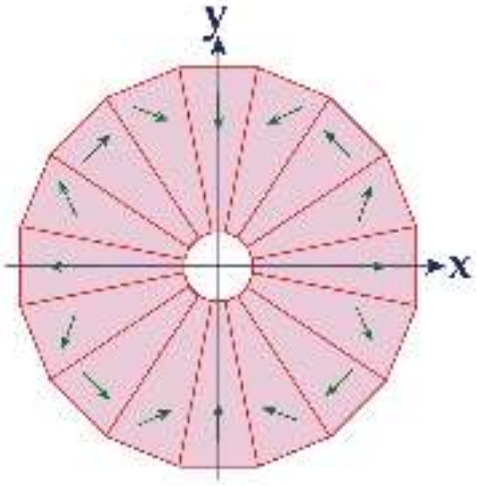

Figure 3.5.: A scheme of the cross section of the quadrupole built by Halbach. With its trapezoidal components and the self-contained structure it differs strongly from Mallinson's tape. Nevertheless, the main principle, i.e. the rotation of consecutive magnetization vectors by a fixed degree, is equal in both cases. From [8].

The nowadays classical one-dimensional Halbach array consists of at least four cubic permanent magnets in a row, whose magnetizations are rotated by 90° along the longitudinal axis. The increase and decrease happen on the sides of the array where the transversely orientated magnets are pointing to. This 4-piece unit can, in principle, be repeated endlessly along the row. If the row is finite, a periodic magnetic field with edge effects on both ends of the row is generated. A sketch of such an array consisting of five magnets is shown in figure 3.6.

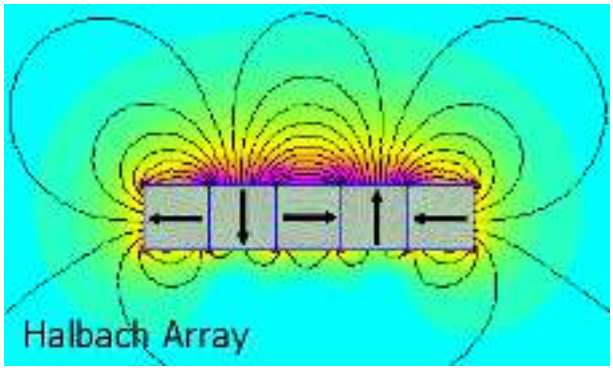

Figure 3.6.: A simulation of an exemplary classical Halbach array. The magnetizations of the five cubic magnets are arranged similarly to figure 3.4. The magnetic field is increased on the upper side and decreased on the lower side. It is clearly visible that the field on the upper side differs at the edges due to edge effects. These effects also result in a small, but not entirely vanishing field on the lower side. From [79].

Aside from this classical structure it is also possible to construct modified Halbach arrays. Some examples are arrays with rectangular instead of cubic magnets, arrays with cylindrical magnets or arrays whose magnetizations are rotated by less than 90°.
The magnetic field of BRASS required for the search for ALPs is planned to be generated by a two-dimensional Halbach array. This array is planned to be located on the inner surface of the dish antenna with a reflecting surface on top of it. Naturally, this reflecting surface should be as thin as possible so that it blocks only a small volume of the field.
There are multiple ways to build two-dimensional Halbach arrays out of cubic magnets. It is possible to create arrays with the Halbach structure either just in one dimension of the array or in both dimensions. However, it is impossible to build an array solely consisting of Halbach structured rows in both dimensions. These various possibilities are discussed in section 4.4.

3.4. Forces between magnets

The construction of a Halbach array is accompanied by forces exerted between the individual magnets of the array. Because of these repellent and torsional forces, the magnets need to be fixated to obtain a stable array. One way to do so is to glue the magnets together. This process is described in section 5.3.

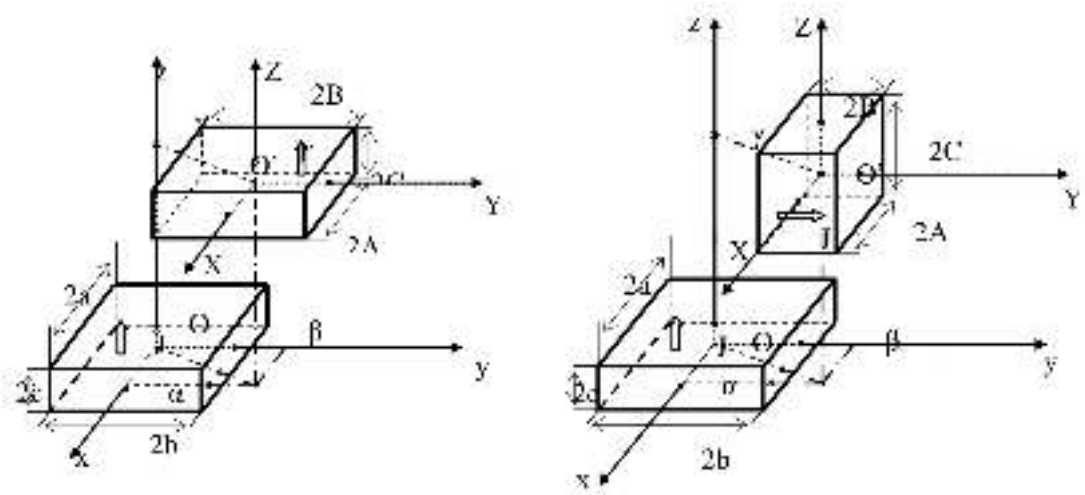

(a) orientated in parallel (b) orientated perpendicularly

Figure 3.7.: Orientation of the two magnets relative to each other. This sketch is the basis of the force calculations. In both cases, a, b, c, A, B, C are half the edge lengths of the magnets and α, β, γ are the distances of the centres with regard to the x-, y-, z-axis respectively. In the perpendicular case, if both magnetizations have a positive leading sign, the first one points towards the positive z-direction and the second one points towards the positive y-direction. From [80].

The repellent forces can be calculated in different ways. One approach is the calculation via the virtual work method which was first published by Akoun and Yonnet in 1984 for two magnets with magnetizations orientated in parallel, as shown in figure 3.7(a) [81]. They denoted the dimensions of the two magnets as $(2a, 2b, 2c)$ and $(2A, 2B, 2C)$ respectively and the vector lying between the centres of the magnets as (α, β, γ), all given in m. Defining and using the following auxiliary quantities

$$\begin{aligned} U_{ij} &= \alpha + (-1)^j A - (-1)^i a \\ V_{kl} &= \beta + (-1)^l B - (-1)^k b \\ W_{pq} &= \gamma + (-1)^q C - (-1)^p c \\ R &= \sqrt{U_{ij}^2 + V_{kl}^2 + W_{pq}^2}, \end{aligned} \tag{3.29}$$

they stated the force to be

$$F = \frac{J \cdot J'}{4\pi \cdot \mu_0} \sum_{i=0}^{1} \sum_{j=0}^{1} \sum_{k=0}^{1} \sum_{l=0}^{1} \sum_{p=0}^{1} \sum_{q=0}^{1} (-1)^{i+j+k+l+p+q} \cdot \phi\left(U_{ij}, V_{kl}, W_{pq}, R\right), \tag{3.30}$$

with J and J' as the two magnetizations in T. The factor ϕ has the three components

$$\phi_x = \frac{1}{2}(V^2 - W^2)\ln(R-U) + UV\ln(R-V) + VW\arctan\left(\frac{UV}{RW}\right) + \frac{1}{2}RU, \tag{3.31}$$

$$\phi_y = \frac{1}{2}(U^2 - W^2)\ln(R-V) + UV\ln(R-U) + UW\arctan\left(\frac{UV}{RW}\right) + \frac{1}{2}RV, \tag{3.32}$$

$$\phi_z = -UW\ln(R-U) - VW\ln(R-V) + UV\arctan\left(\frac{UV}{RW}\right) - RW. \tag{3.33}$$

In 2009 Yonnet and Allag expanded this initial work to cover forces exerted between magnets with magnetizations perpendicular to each other, as shown in figure 3.7(b) [80]. In this case the factor ϕ changes to

$$\begin{aligned} \phi_x = &- VW\ln(R-U) + UV\ln(R+W) + UW\ln(R+V) \\ &- \frac{U^2}{2}\arctan\left(\frac{VW}{RU}\right) - \frac{V^2}{2}\arctan\left(\frac{UW}{RV}\right) - \frac{W^2}{2}\arctan\left(\frac{UV}{RW}\right), \end{aligned} \tag{3.34}$$

$$\phi_y = + \frac{U^2 - V^2}{2}\ln(R+W) - UW\ln(R-U) - UV\arctan\left(\frac{UW}{RV}\right) - \frac{1}{2}RW, \tag{3.35}$$

$$\phi_z = + \frac{U^2 - W^2}{2}\ln(R+V) - UV\ln(R-U) - UW\arctan\left(\frac{UV}{RW}\right) - \frac{1}{2}RV. \tag{3.36}$$

In the case of cubic magnets, it is obvious that these formulae are not defined if the mentioned centre vector is non-zero in just one or in two dimensions. If this is the case, the formulae can be modified using the following limits:

$$\lim_{x\to 0} x \cdot \ln(x) = 0 \tag{3.37}$$

$$\lim_{x\to 0} x \cdot \arctan\left(\frac{y}{x}\right) = \lim_{x,y\to 0} x \cdot \arctan\left(\frac{y}{x}\right) = 0 \tag{3.38}$$

$$\lim_{x\to 0} \arctan\left(\frac{y}{x}\right) = \frac{\pi}{2} \tag{3.39}$$

If the magnets are on the same height and perfectly aligned, which is the case in an ideal array, there are three different possible arrangements, which are shown in figure 3.8. Note that a turn by 180° of one of the magnets only changes the sign of the results but not its value. For various distances between the centres of two magnets the calculated repellent forces are given in tables 3.1, 3.2 and 3.3. The formulae for the calculation of the torsional forces can be found in [80] but will not be covered in this thesis.

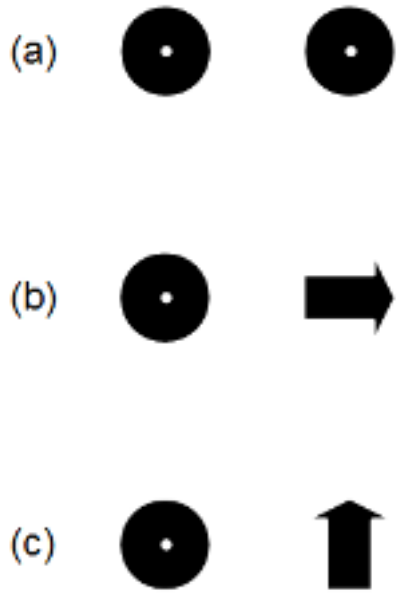

Figure 3.8.: Sketches of possible orientations of the magnetizations of two adjacent magnets relative to each other. The arrows indicate the direction of magnetization, the circles indicate magnetizations pointing out of the paper plane (i.e. in z-direction). The arrow in (b) points in the y-direction and the one in (c) points in the negative x-direction. Every other possible arrangement is a rotated or translated (or both) version of one of these three arrangements. In the strict sense, (c) is a rotated translation of (b). However, regarding the repellent forces these two arrangements are utterly distinguishable. A 180° flip of a magnetization only changes the sign of the resulting repellent force, but not its value.

Table 3.1.: Repellent forces in N with regard to the relative orientation of two magnets with a magnetization of 1.4 T each. The rows correspond to the orientations given in figure 3.8 and the associated direction of the acting force. The columns correspond to the distances between the centres of the two magnets in y-direction. These distances equate to the possible distances in a row of five magnets with an interspace of 0.1 mm each. Note that only the repellent forces are calculated, but not the torsional forces.

		12.1 mm	24.2 mm	36.3 mm	48.4 mm
(a)	F_y	42.84	3.08	0.63	0.20
(b)	F_z	-42.84	-3.08	-0.63	-0.20
(c)	F_i	0	0	0	0

Table 3.2.: Repellent forces in N with regard to the relative orientation of two magnets with a magnetization of 1.4 T each. The structure is equal to the structure of table 3.1. The given distances equate to the possible distances in a row of five magnets with an interspace of 0.5 mm each.

		12.5 mm	25.0 mm	37.5 mm	50.0 mm
(a)	F_y	36.14	2.72	0.56	0.18
(b)	F_z	-36.14	-2.72	-0.56	-0.18
(c)	F_i	0	0	0	0

Table 3.3.: Repellent forces in N exerted between two magnets orientated as depicted in figure 3.8(b). The given distances (in mm) are, regarding the absolute values, the same as in table 3.1, but they are referring to the x-direction.

distance	F_z
0.0	-42.84
12.1	-9.01
24.2	-0.90
36.3	-0.16
48.4	-0.04

Another way to calculate the forces is the approach via the Lorentz force. This approach provides the same results although the formulae differ noticeable. A review regarding this approach can be found in [82].

4. Magnetic field computations

As mentioned before, it is planned to create a magnetic field generated by a Halbach array for BRASS. This is the first time such a magnetic field is used for the haloscopic search for WISPs. Therefore, a better understanding of the relations between the structure and the characteristics of the array and the generated magnetic field is required. For this purpose, magnetic field computations were made for single magnets and for one-dimensional as well as for two-dimensional Halbach arrays. The results of these computations are presented in this chapter.

4.1. CST Studio Suite

The computations are made with the software *CST Studio Suite*. This is a simulation software developed for three-dimensional electromagnetic design. It offers various different solvers for equally various electromagnetic problems. The solver used for the presented computations focuses on the interactions between magnetic elements.
After modelling the relevant magnetic objects and defining the size of the background as well as the boundary conditions, the whole considered volume is divided into a mesh of tetrahedrons. The amount of these tetrahedrons can be chosen freely, whereby the mesh is rather fine in the volume of the objects and rather coarse in the volume of the background. For every individual tetrahedron, the Maxwell equations are solved separately. The resulting total field is a superposition of all these individual results. While solving the equations, the mesh of tetrahedrons gets adaptively refined to improve the results. For the analysis of the field, a cubic grid with a grid constant of either 0.1 mm (single magnet computations) or 0.2 mm (Halbach array computations) is constructed. The output data contains the field strength at the positions of the grid points.
The basic modelled objects of the computations are cubic magnets with an edge length of 12 mm. Their magnetization is defined as 1.4 T. Compared to real magnets and arrays, the modelled ones differ as follows, resulting in them being rather idealized:

- The definition of the background does not include the terrestrial magnetic field. However, since it is much smaller than the field of the cubic magnets, differing by 4 orders of magnitude, it can indeed be neglected.

- The protecting coating of real magnets made of $Nd_2Fe_{14}B$ is not included either. Since this coating is applied to prevent corrosion and since it should only barely change the magnetic properties of the magnet due to its small thickness, it can reasonably be neglected.

- For the creation of the arrays, the magnets are modelled directly next to each other without any gap in between. Therefore, compared to a real array, neither the non-zero distance between the magnets nor the glue inside these gaps are considered. Since the gaps of real arrays should not be greater than 0.5 mm (as a well-spaced upper limit) and since the glue should not affect the magnetic field lines, their influence is assumed to be negligibly small.

- The model of the permanent magnets is essentially just a magnetization defined in the middle of the cubic volume. Therefore, the model neglects specific magnetic and material-dependent properties of $Nd_2Fe_{14}B$. This is presumably the biggest difference between the model and the real magnets.

- It is not clearly apparent if the computations consider the interactions between the individual magnets. As described in section 2.4.2, the remanence of a permanent magnet decreases in an opposed magnetic field. Since the model only contains given total values of magnetizations and not permanent magnets with given remanences and hysteretic behaviour, it is assumed that these interactions are not considered. Further detail concerning this problem can be found in section 6.1.

4.2. Single magnets

In a first step, the magnetic field of a single magnet was computed. The plots in figure 4.1 show the horizontal components of this field at various distances above the pole face of the magnet. The distances are selected specifically so that a comparison with experimental results is possible (this is further described in section 5.2).
The plots show a symmetric field. Directly above the middle of the magnet there is almost no horizontal field component. Moving outwards, the horizontal field increases, peaks at the edges of the magnet and then decreases again, thus resulting in an almost circular shape. While the overall shape of the field remains the same, the field strength decreases with increasing distance. The peak values at the four depicted distances are $B_{\parallel} = 281\,\mathrm{mT}$, $B_{\parallel} = 236\,\mathrm{mT}$, $B_{\parallel} = 201\,\mathrm{mT}$ and $B_{\parallel} = 173\,\mathrm{mT}$ respectively. Hence, the field strength decreases by 38% over a difference in height of 1.5 mm in the considered region above the magnets.

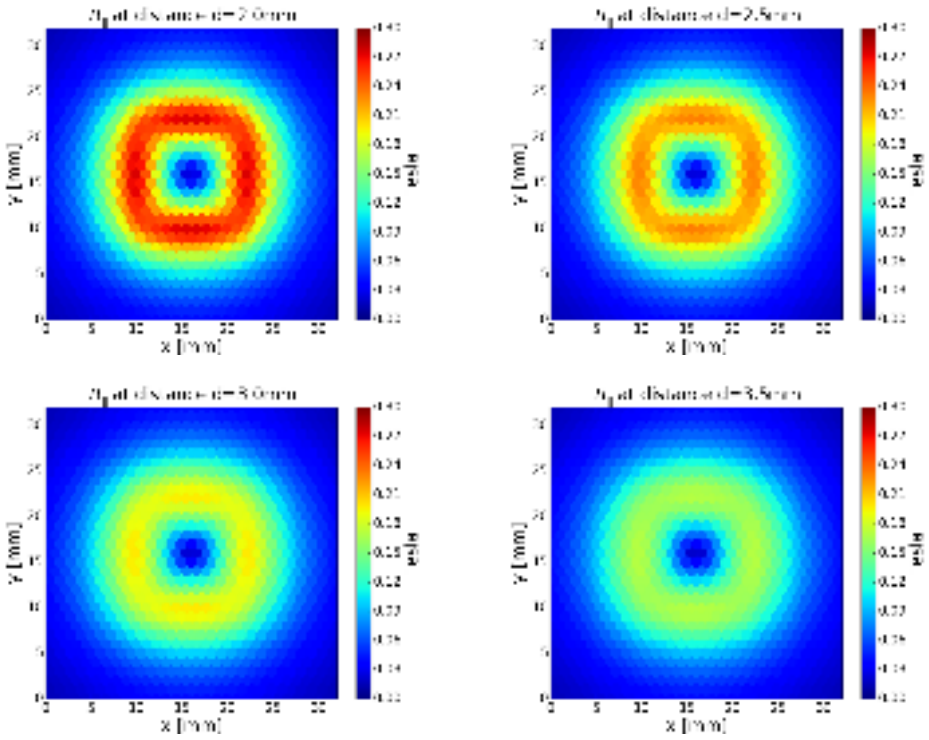

Figure 4.1.: The results of the magnetic field computations of a single magnet. The plots show the field at distances $d = 2.0\,\text{mm}, 2.5\,\text{mm}, 3.0\,\text{mm}, 3.5\,\text{mm}$. The magnet is located such that $10 \leq x \leq 22$ and $10 \leq y \leq 22$.

4.3. One-dimensional Halbach arrays

The subject of the next computations is a one-dimensional Halbach array. The considered basis is an array consisting of four magnets whose magnetizations are rotated sequentially by 90° each. Such an array is called "1D Halbach unit". Again, plots of the horizontal field at 4 different distances above the array are shown in figure 4.2. The reason for the distances to differ compared to the ones in figure 4.1 is stated in section 5.4. The plotted field is the part above the field-increasing side of the Halbach array.

Naturally, the field displayed in these plots is less symmetric than the previous one. Above the vertically orientated magnets there is (again) almost no horizontal field. The areas with high field values lie above the horizontally orientated magnets. The field strength above the horizontal magnet surrounded by the vertical ones is higher than the one above the other horizontal magnet. Therefore, the computations clearly show an increase of the horizontal field due to the Halbach structure. Again, the field strength decreases with increasing distance while the overall shape remains unchanged. In this case, the peak values at the four depicted distances are $B_{\parallel} = 437\,\text{mT}$, $B_{\parallel} = 391\,\text{mT}$, $B_{\parallel} = 356\,\text{mT}$ and $B_{\parallel} = 324\,\text{mT}$ respectively. This corresponds to a decrease by 26% over a difference in height of 1.5 mm in the considered region above the array.

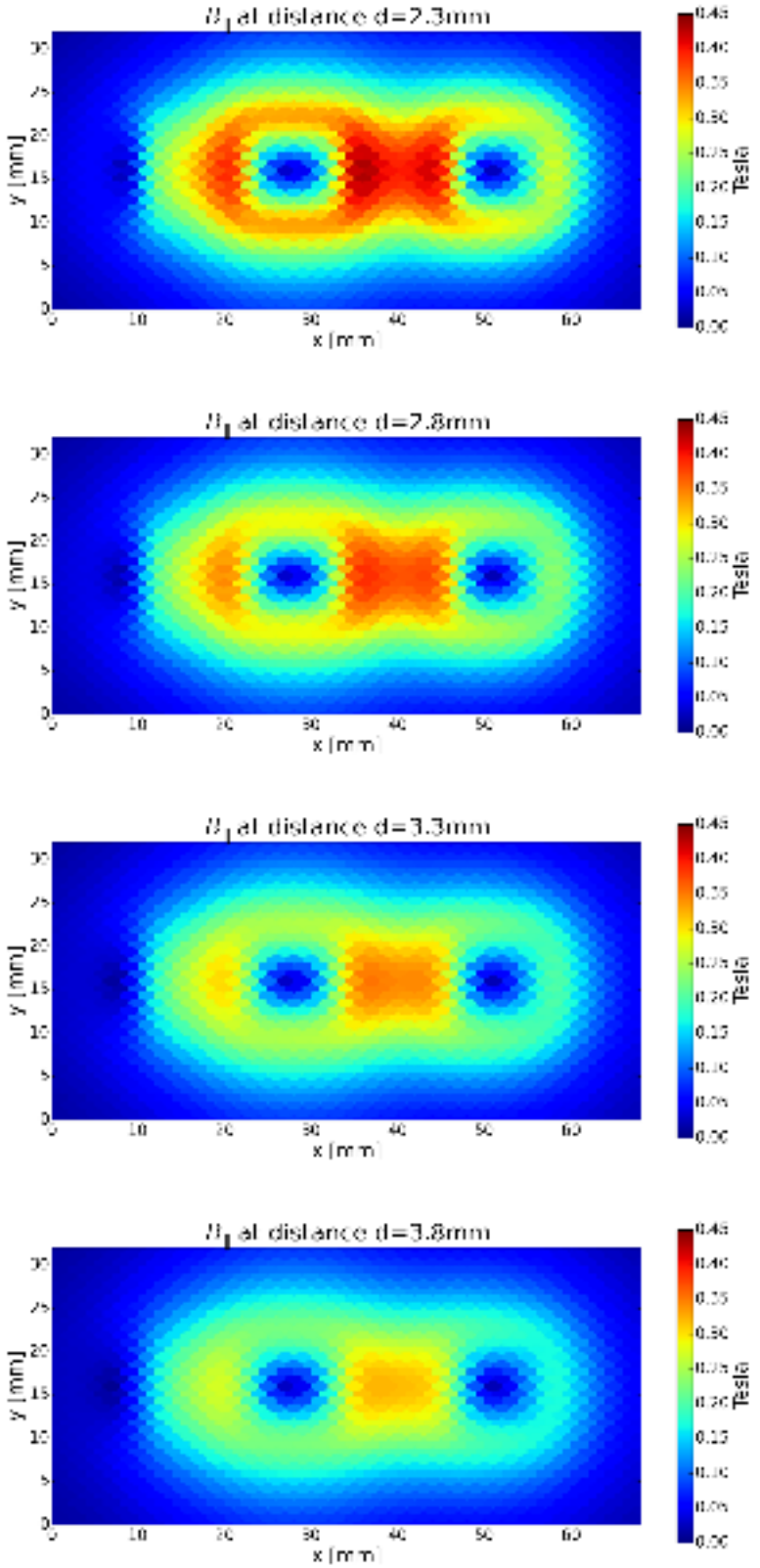

Figure 4.2.: The results of the magnetic field computations of a 1D Halbach unit. The plots show the field at distances $d = 2.3\,\text{mm}, 2.8\,\text{mm}, 3.3\,\text{mm}, 3.8\,\text{mm}$. The array is located such that $10 \leq x \leq 58$ and $10 \leq y \leq 22$.

4.4. Two-dimensional Halbach arrays

4.4.1. 5x5 array

The third phase of the field computations focuses on two-dimensional Halbach arrays. Contrary to the one-dimensional Halbach structure, there are various possibilities to arrange the magnets in two dimensions in a way that yields an increase of the magnetic field. Naturally, not all these variations offer the same enhancement. For the purpose of finding an arrangement which provides a preferably high $\langle \mathbf{B}_{\parallel}^2 \rangle$, the magnetic fields of a total of seven different arrangements, which differ to a greater or lesser extent, were computed.

The basis of these computations is a 5x5 array. A 4x4 array would have also been reasonable, being the smallest possible quadratic Halbach structure, analogue to the one-dimensional case. However, for the sake of symmetry, a fifth row and column respectively were added. For each of the seven computations a sketch of the arrangement as well as a plot of the horizontal magnetic field at a distance of 0.4 mm above the array are shown in figures 4.3 to 4.5. In the sketches the arrows point towards the south pole, which is indicated by the circle with a dot, and the circle with an X indicates the north pole. The red lines indicate a field increasing Halbach structure and the blue lines indicate a field decreasing Halbach structure.

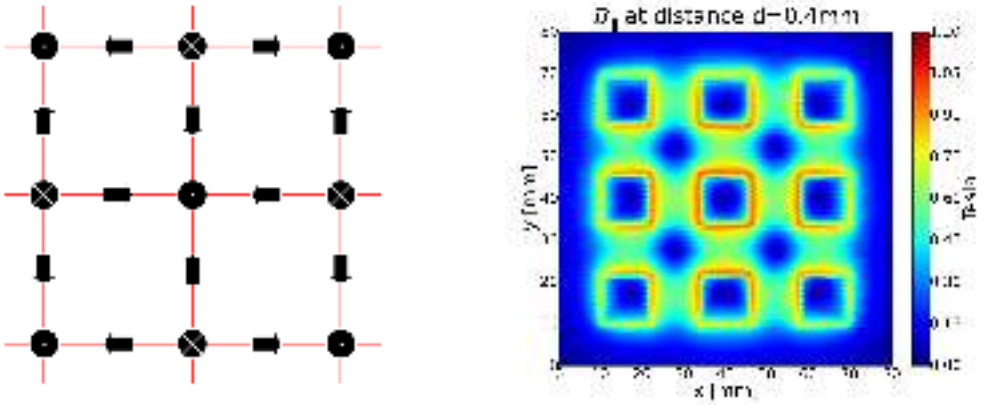

(a) Natural: Hole

Figure 4.3.: This arrangement is called “Natural: Hole”. The first part of its name originates in its composition: when starting at one edge magnet building the Halbach structure in both dimensions and repeating this at the other edge magnets, this arrangement is the result. It is therefore the “natural” way to build a 2D Halbach array. The second part corresponds to the missing magnets (the “holes”) in between the Halbach lines.

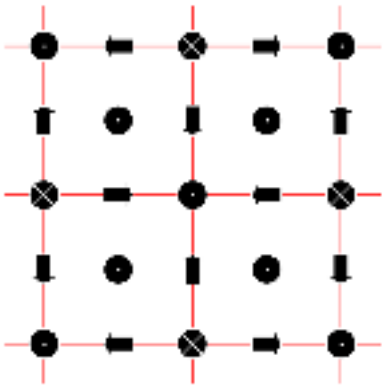

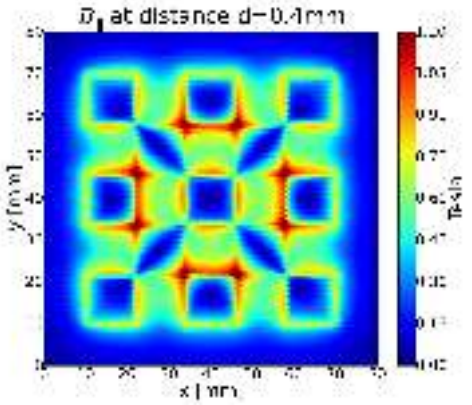

(a) Natural: Up

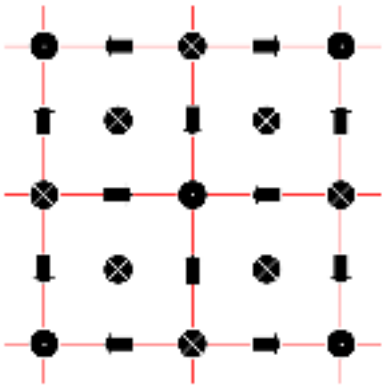

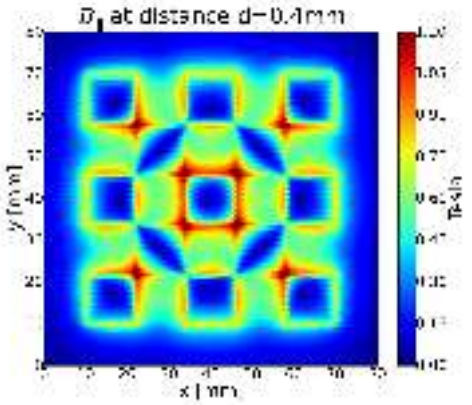

(b) Natural: Down

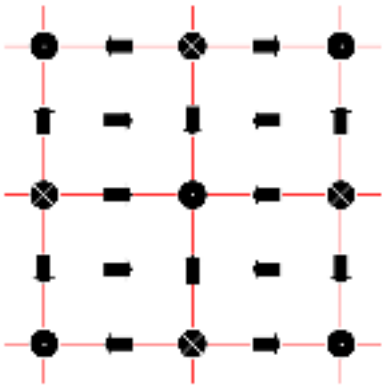

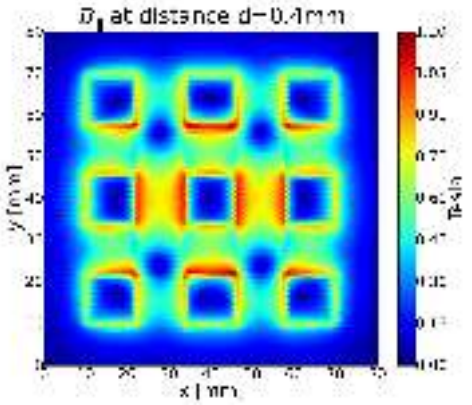

(c) Natural: Middle

Figure 4.4.: The arrangement in figure 4.3 is the template for these arrangements. It is filled with magnets pointing upwards (a), downwards (b) or towards the middle as seen from one of the two horizontal directions (c).

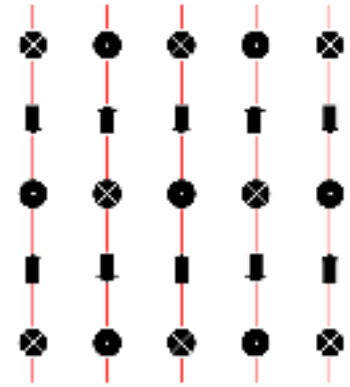

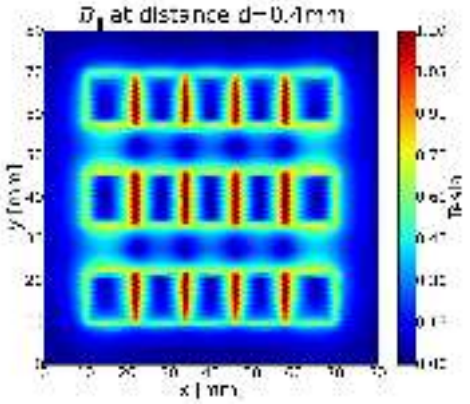

(a) Alternating

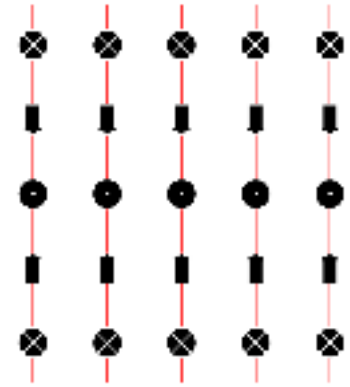

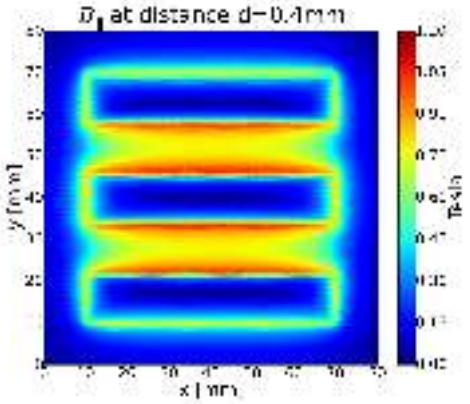

(b) Parallel: all magnets

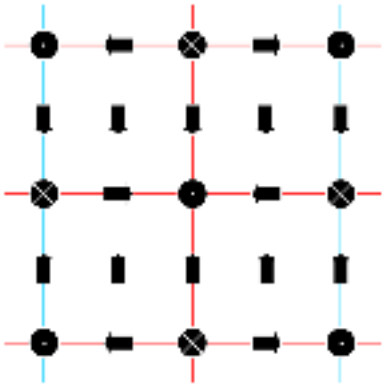

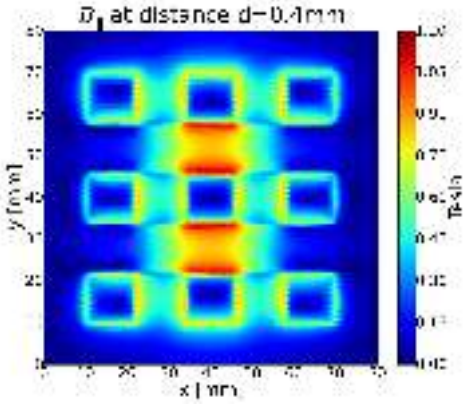

(c) Parallel: link magnets

Figure 4.5.: These arrangements are composed of parallel magnets (with respect to the x-axis). In (a) and (b) all magnets are parallel, whereas (a) is consisting of magnets with alternating magnetizations and (b) is consisting of magnets with equal magnetizations. In (c) only the linking magnets between the field increasing Halbach lines are parallel to each other.

It is clearly visible that the varying arrangements differ both in the profile and the peak strength of the field. The arrangement called "Alternating" (4.5(a)) for example offers the highest field strength but does so only in particularly small areas.
As mentioned in section 3.2, the sensitivity of BRASS does not depend on the horizontal magnetic field, but on the mean of the squared horizontal field. A comparison of all arrangements regarding this value at various distances is given in figure 4.6. For this comparison, $\langle \mathbf{B}_{\parallel}^2 \rangle$ is evaluated at distances in the range of $0.2\,\mathrm{mm} \leq d \leq 3.0\,\mathrm{mm}$. It is assumed that the WISPs possess a conversion length $\sim \lambda$ inside the magnetic field. The evaluated range of distances is therefore equal to the considered range of WISP wavelengths for BRASS. This in turn corresponds approximately to WISPs with masses in the range of $1500\,\mathrm{eV} \geq E_{\mathrm{WISP}} \geq 30\,\mathrm{eV}$. This is the planned mass range of interest of BRASS.

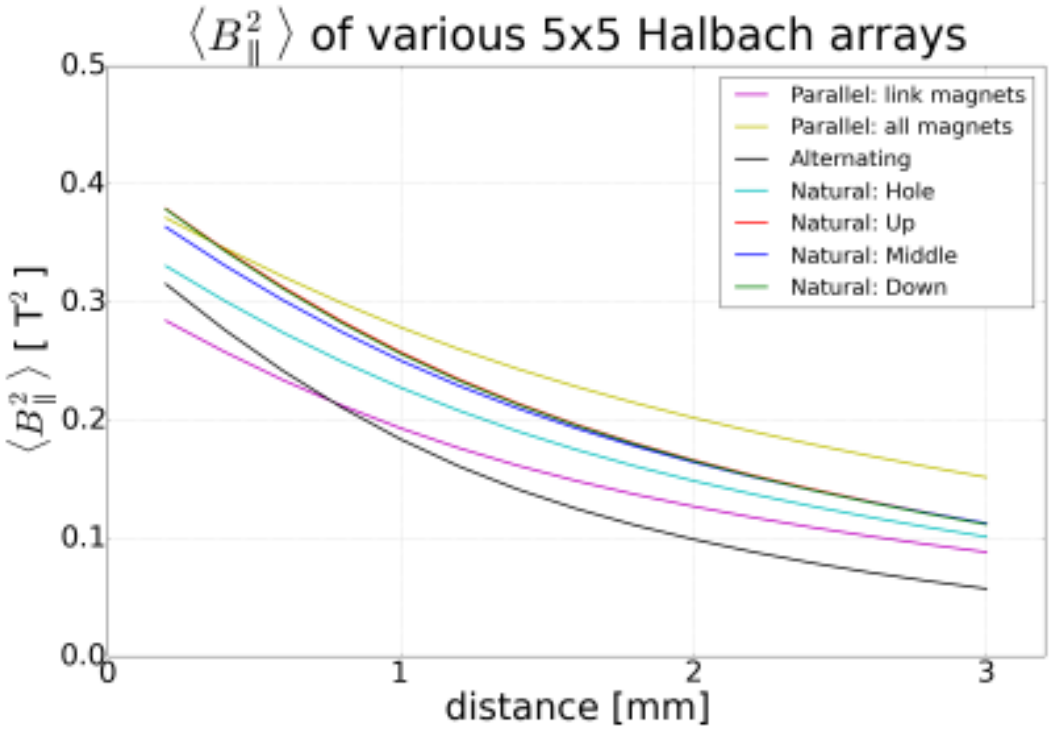

Figure 4.6.: A comparison of all presented 5x5 arrays. This plot shows the mean squared horizontal magnetic field with respect to the distance above the high field side of the arrays. While the "Natural: Up" and "Natural: Down" arrangements, which almost share the exact same curve, provide the highest $\langle \mathbf{B}_{\parallel} \rangle^2$ at small distances, the arrangement "Parallel: all magnets" provides the highest $\langle \mathbf{B}_{\parallel} \rangle^2$ from $d = 0.4\,\mathrm{mm}$ on upwards.

At the lowest considered distance of 0.2 mm the values of $\langle \mathbf{B}_{\parallel} \rangle^2$ range between $0.28\,\mathrm{T}^2$ and $0.37\,\mathrm{T}^2$. There are four arrangements at the higher limit of this range, two in the middle and one at the lower limit.
Naturally, the values of $\langle \mathbf{B}_{\parallel} \rangle^2$ decrease with increasing distance. The seven curves take similar sloping courses. In a direct comparison, three of them are rather shallow, whereas the other four are slightly steeper. Interestingly, there are only two intersections between all seven curves.
At the highest considered distance of 3.0 mm, the values range between $0.06\,\mathrm{T}^2$ and $0.15\,\mathrm{T}^2$. At this point, there is one arrangement each providing the upper and lower limit. The curves of the other five arrangements approach each other and settle at values of about $0.1\,\mathrm{T}^2 \pm 0.01\,\mathrm{T}^2$.
The arrangement “Alternating” provides the second lowest value of $\langle \mathbf{B}_{\parallel} \rangle^2$ at low distances and by far the lowest value at high distances. It is therefore not a suitable choice for the realization of a real 5x5 Halbach array. The same applies to “Parallel: link magnets”, which indeed has the shallowest curve, but provides the lowest values at low distances and the second lowest values at high distances. Slightly steeper, but also representing slightly higher values is the curve of “Natural: Hole”. This arrangement could be denoted as the mediocre one. The three considered variants to fill the gaps of this arrangement almost provide identical results. While the curves of “Natural: Up”, “Natural: Down” and “Natural: Middle” overlap at distances $d \geq 2.0\,\mathrm{mm}$, the former two, which almost share the exact same curve, provide slightly higher values at the lower distances. In fact, their values are the highest at distances $d \leq 0.4\,\mathrm{mm}$. However, they are surpassed by “Parallel: all magnets” at higher distances, which provides the second best values at low distances and whose curve is in addition also shallower. This arrangement therefore seems to be the best option at this point.

4.4.2. 17x17 array

The results of the 5x5 computations are supposedly affected by edge effects. To minimize this influence the arrangements were expanded periodically so that the computations could be done again with 17x17 arrays. This size should be large enough to reduce the edge effects measurably. Simultaneously, with its edge length of $\simeq 20\,\mathrm{mm}$ it could be later used as a model for a first testing dish antenna setup. The resulting plots of the horizontal fields, again evaluated at a distance of 0.4 mm above the array, are shown in figures 4.7 to 4.9.

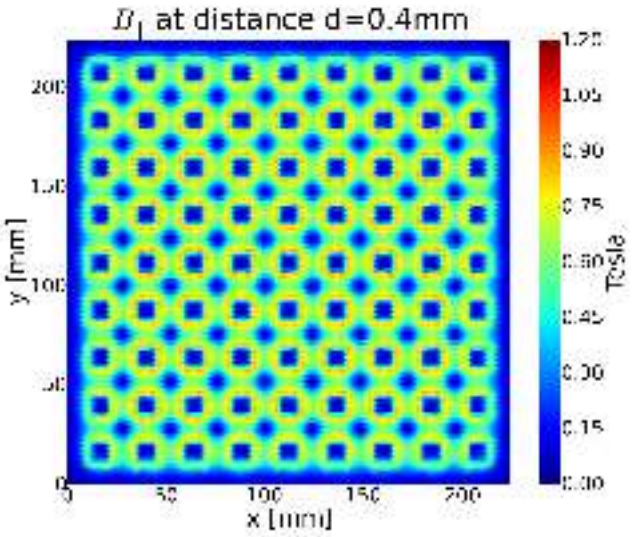

Figure 4.7.: Plot of the 17x17 version of the “Natural: Hole” arrangements.

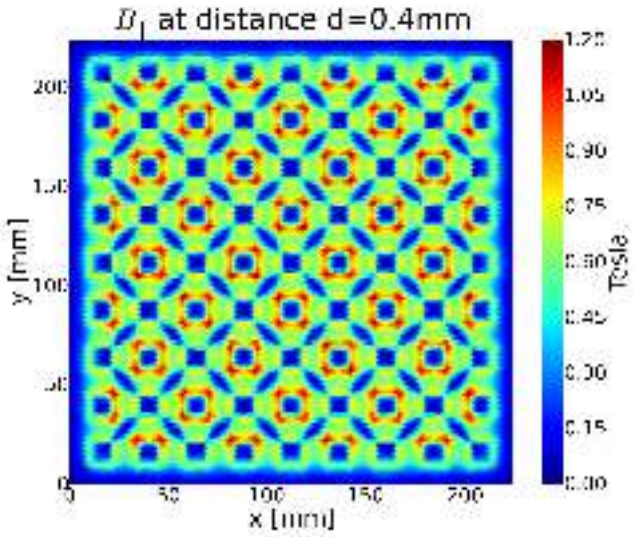

(a) Natural: Up

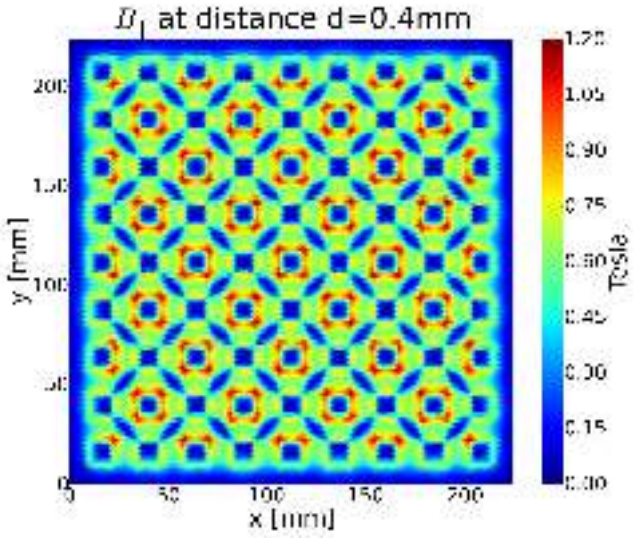

(b) Natural: Down

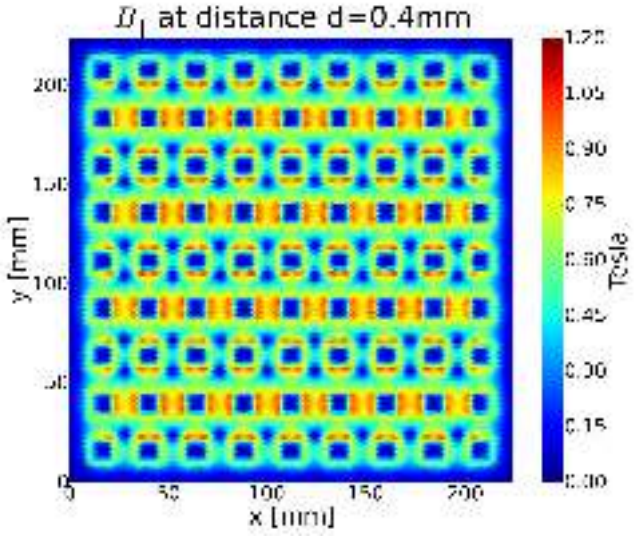

(c) Natural: Middle

Figure 4.8.: Plots of the 17x17 versions of the “Natural” arrangements.

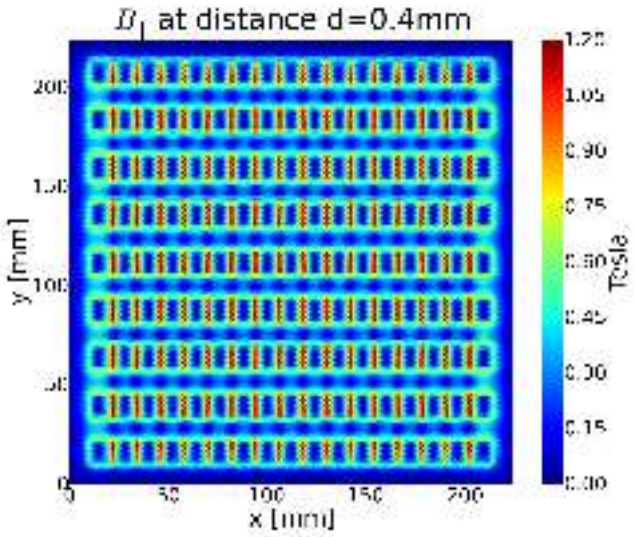

(a) Alternating

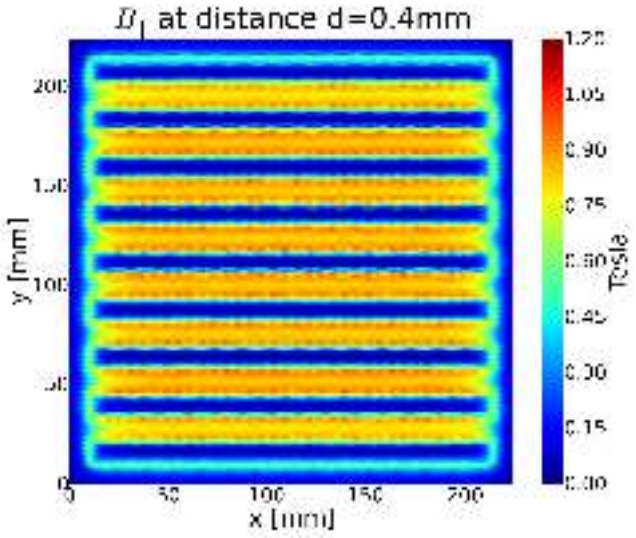

(b) Parallel: all magnets

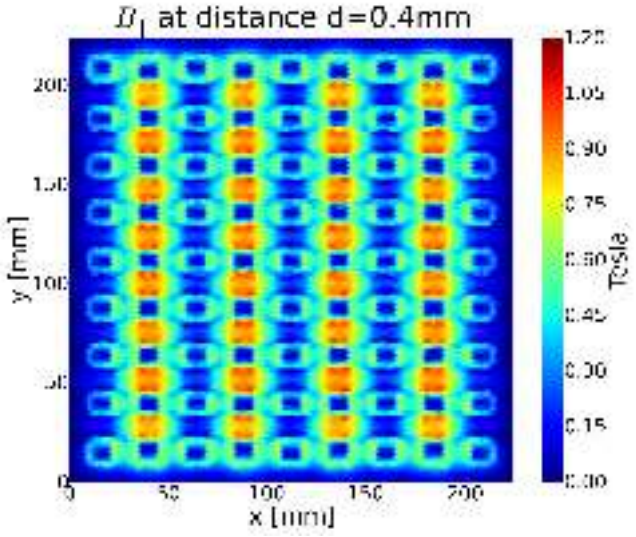

(c) Parallel: link magnets

Figure 4.9.: Plots of the 17x17 versions of the "Parallel" arrangements and the "Alternating" one.

It is no big surprise that the plots look similar to the plots of the 5x5 arrays. The overall shape of the particular horizontal fields gets expanded just like the arrangements of the magnets. This, however, only applies to $\mathbf{B}_{\parallel}$. In contrast, the difference in $\langle \mathbf{B}_{\parallel}^2 \rangle$ changes measurably. This is clearly visible in the comparison of the seven arrangements given in figure 4.10.

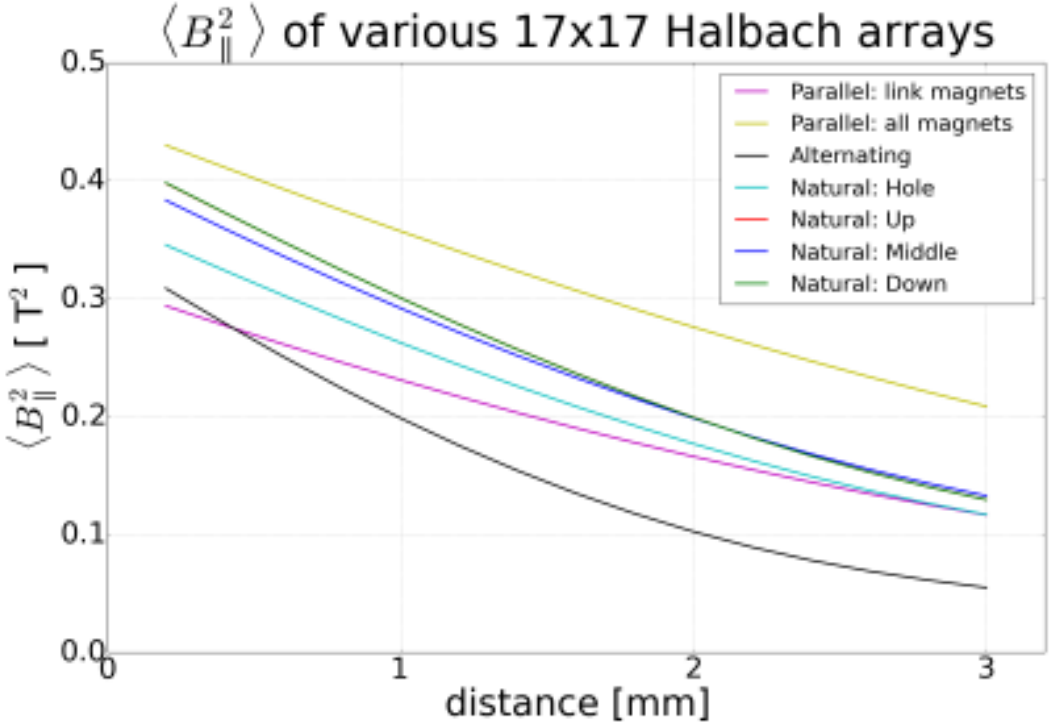

Figure 4.10.: A comparison of all presented 17x17 arrays. This plot shows the mean squared horizontal magnetic field with respect to the distance above the high field side of the arrays. Again, the curves of the "Natural: Up" and "Natural: Down" arrangements almost overlap entirely. Contrary to the 5x5 case in figure 4.6, the "Parallel: all magnets" arrangement provides the highest $\langle \mathbf{B}_{\parallel}^2 \rangle$ at every measured distance above the array.

Compared to the 5x5 case, the range of values of $\langle \mathbf{B}_{\parallel}^2 \rangle$ has slightly increased in the 17x17 case. At the lowest considered distance, the values range between $0.29\,\mathrm{T}^2$ and $0.43\,\mathrm{T}^2$. At the highest considered distance, they range between $0.05\,\mathrm{T}^2$ and $0.21\,\mathrm{T}^2$.
The curves in the 17x17 case are also sloping, but they seem to do so more linearly. Moreover, every arrangement provides higher values than in the 5x5 case. The smallest disparity occurs at the "Alternating" arrangement with a peak rise of 9% and an average rise of only 3%. The "Natural" arrangements show similar rises (related to each other) between 5% and 21% with an average of about 15%. Finally, the "Parallel" arrangements benefit the most from the expansion to the 17x17 size. "Parallel: link magnets" shows rises between 3% and 32% with an average of 24% (which is higher than the peak rises of the other ones). Nevertheless, its absolute values are still the second lowest. The greatest disparity occurs at the "Parallel: all magnets" arrangement. This one experiences an exceptional minimum rise of 16%, a peak rise of 38% and an average of 31%. At distances $d > 1.0\,\mathrm{mm}$ the average is even higher, increasing to 36%. These results show that the values of $\langle \mathbf{B}_{\parallel}^2 \rangle$ are indeed affected by edge effects. The influence of these effects varies heavily depending on the considered arrangement.
The most important difference to the 5x5 case is the fact that the arrangement "Parallel: all magnets" now provides by far the highest values regardless of the distance. It is therefore the most suitable one of the introduced two-dimensional Halbach arrangements for BRASS and will be the preferred one for future considerations.

5. Preliminary measurements

The computations presented in the last chapter yield various useful information regarding the characteristics of Halbach arrays. To verify that the computational results are in agreement with reality, the magnetic field of real Halbach arrays was measured. These arrays are composed of magnets with properties almost identical to the ones assumed for the computations. This chapter includes a description of the experimental setup, a presentation of the method used for the construction of real Halbach arrays and the results of the magnetic field measurements, which are also compared to the computational ones.

5.1. Experimental setup

The permanent magnets used for the preliminary measurements are cubic magnets with an edge length of 12 mm. Their core is made from an alloy of neodymium, iron and boron in the form of $Nd_2Fe_{14}B$ and covered with a 0.65 mm thick compound of nickel and copper. They were made by sintering and are graded with N48, meaning that their energy product is $BH_{\max} = 48\,\mathrm{MGOe}$ and their maximum working temperature is $T_{\max} = 80\,^{\circ}\mathrm{C}$. The value of their remanence lies between 1.37 T and 1.42 T as stated by the manufacturer. A picture of one of these magnets is shown in figure 5.1.

Figure 5.1.: A single cubic magnet used for the preliminary measurements for BRASS. The magnetization direction lies parallel to the centre line between the upper and the lower faces in this picture.

The magnetic field measurements are taken via a standard transversal Hall probe which is mounted to a working table. The table has three independent stepping motors whereby it is possible to navigate the probe in every direction. The whole setup is shown in figure 5.2(a) and a close up view at the probe is shown in figure 5.2(b).

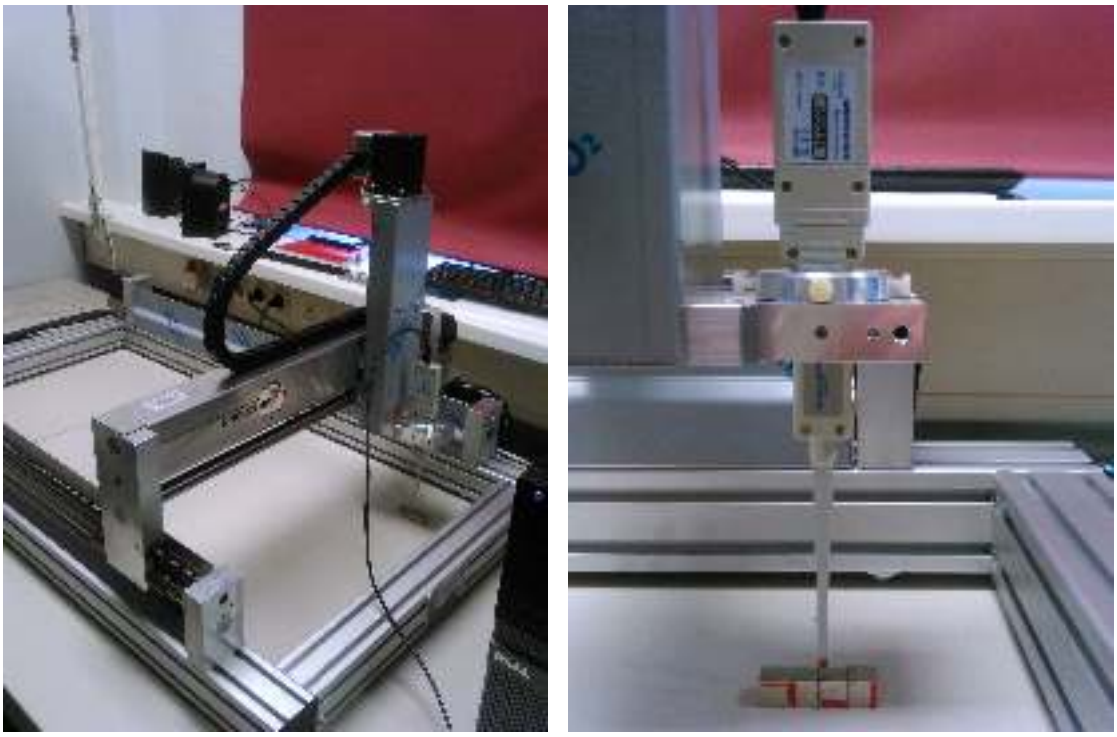

(a) entire setup (b) Hall probe

Figure 5.2.: The setup of the preliminary measurements. Figure (a) shows the entire setup with the working table and the mounted Hall probe. Figure (b) shows a close up of the probe. The tip of the probe (red) contains the active area, see figure 5.3 for details. The mounting is designed such that the probe can be rotated freely and be fixated at steps of 90°. This way, measurements of the field in x- and y-direction respectively, which are compulsory independent of each other, can be taken without readjusting the probe in relation to the magnets.

The probe works with an effective area of 1 mm × 2 mm and offers a measuring range between 2 mT and 2 T. Since the magnetic field is inhomogeneous over a distance of 1 mm, it differs between the top and the bottom of the effective area. It is not fully clear in which way the signal is averaged over the area, so from here on out it is assumed that the output value corresponds to the middle of the area which is 1.7 mm inside the tip of the probe (see figure 5.3). This is of course a possible error source if this assumption fails to be true.

Figure 5.3.: A sketch of the Hall probe used for the magnetic field measurements. The tip of the probe contains the active area, which is surrounded by ceramics. This area has the size 1 mm × 2 mm and its middle is 1.7 mm inside the tip.

The probe can only measure the field in one transversal direction. Therefore, a full horizontal field measurement consists of the two runs measuring the field in x-direction and y-direction respectively. Unfortunately there is no possibility to synchronize the start of the movement of the table and the start of the measurement of the probe. Instead, the start of the measurement is triggered by hand. This results in an uncertainty because it is not possible to create an exact mapping of the data points. While analysing the data, it became apparent that the number of data points exactly matches the expected number assuming there would be no change in velocity during a 90° turn on the path. This would imply an infinite acceleration which is naturally impossible. It is unclear how the table handles these turns so there might be an additional error source at these edge points.
A particular run is a scanning of the area at a given distance above the magnet or array. This scanning is performed row-wise alongside the x-axis. After every row the probe is moved 1 mm further in the y-direction. The probe measures with a frequency of 0.2 Hz. For the measurements, the stepping motors were tuned so that the probe moves with a velocity of $5\,\frac{\mathrm{mm}}{\mathrm{s}}$ in both the x- and y-direction. This way every data point is related to a tuple of integer values x and y. The plots in the following sections are, however, binned hexagonally. This was done for smoother plots and to ease the comparison with the computational results.

5.2. Single magnets

The first preliminary measurements were taken with single magnets. For the best understanding of the underlying physics of the Halbach arrays, the magnets composing the arrays need to have a similar remanence and need to produce the same field. Therefore, 19 out of the several hundreds of available magnets were randomly picked to check if their produced field is statistically equal.
The horizontal components of the field were measured at four different distances at intervals of 0.5 mm above the pole side of the magnets. The lowest distance is on the one hand limited by the position of the active area related to the edge of the tip of the probe, as discussed in the last section. On the other hand, a small gap of about 0.3 mm was left between the probe and the surface of the magnet. This was done to avoid a contact which could have perturbed the measurements due to the magnet being displaced or the probe getting stuck while the table would still be moving forward. Adding this gap to the 1.7 mm between the centre of the active area and the edge of the tip, the lowest distance was assumed to be ~ 2.0 mm, before comparing the results to the computational ones.
A graphical comparison is displayed in figures 5.4 to 5.7. The respective top left plots correspond to the computational results, whereas the respective other three plots correspond to the measurements of 3 of the 19 magnets. The plots of the remaining magnets can be found in appendix A.

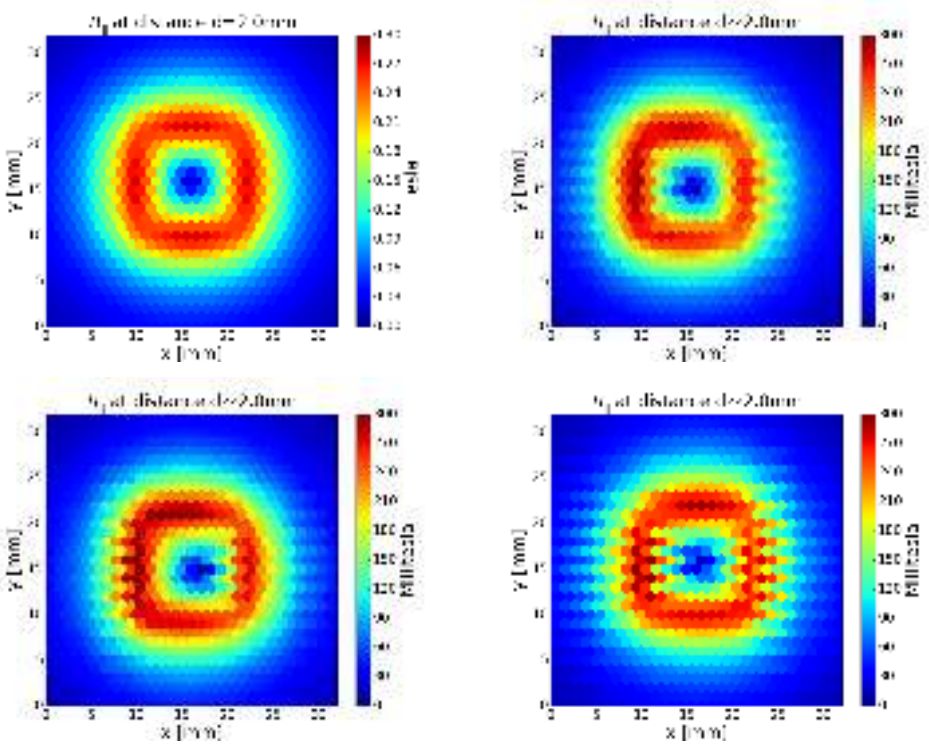

Figure 5.4.: Computed (top left) and measured horizontal magnetic field of single magnets at a distance $d = 2.0\,\mathrm{mm}$.

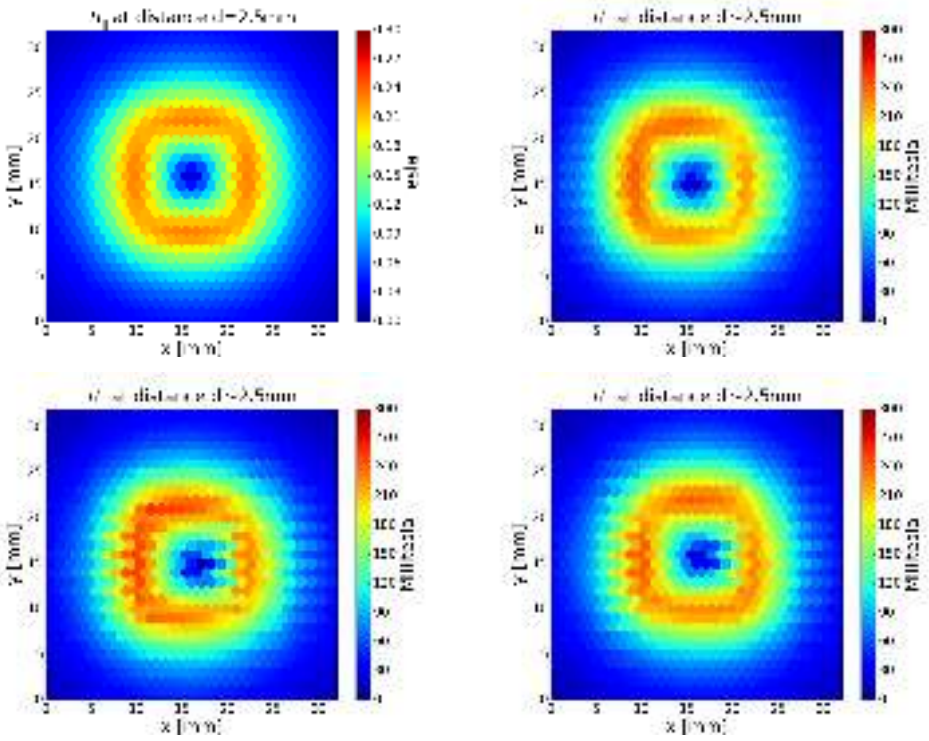

Figure 5.5.: Computed (top left) and measured horizontal magnetic field of single magnets at a distance $d = 2.5\,\mathrm{mm}$.

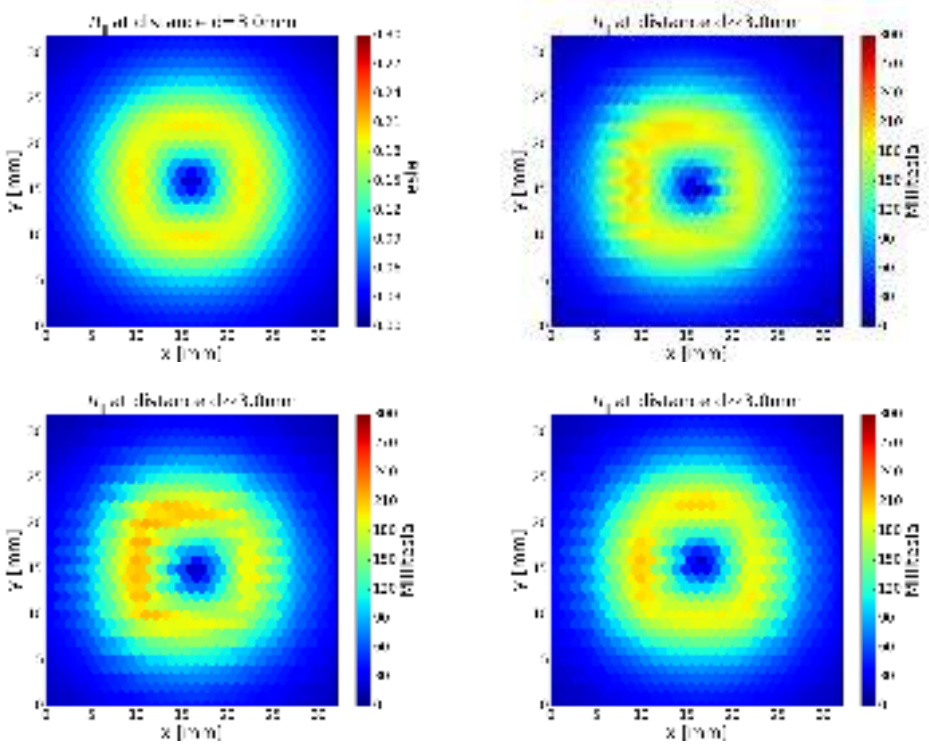

Figure 5.6.: Computed (top left) and measured horizontal magnetic field of single magnets at a distance $d = 3.0\,\mathrm{mm}$.

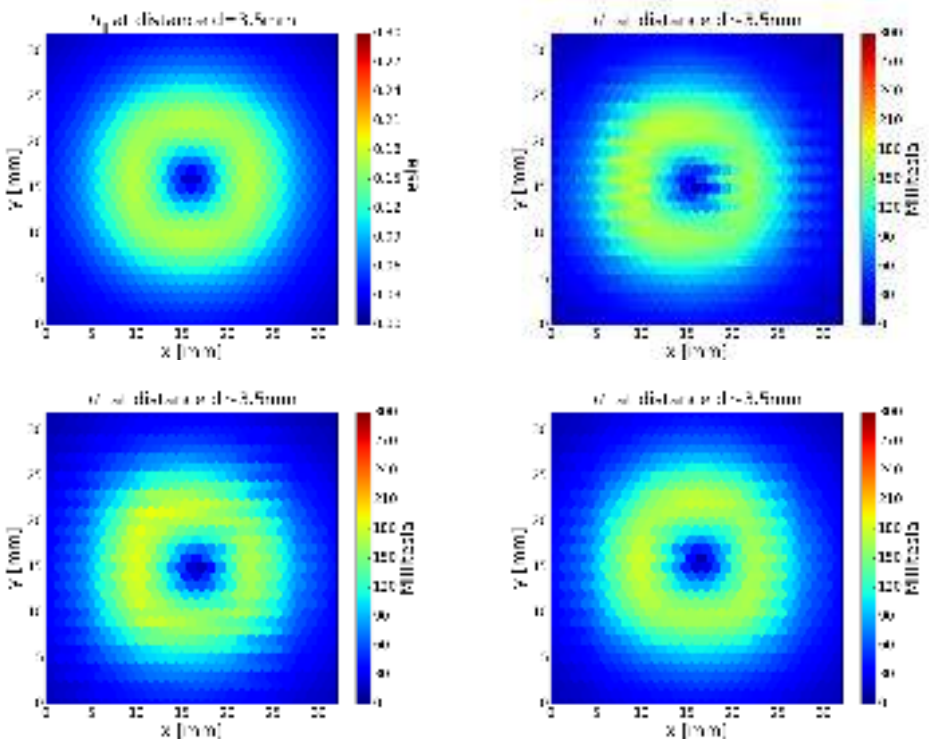

Figure 5.7.: Computed (top left) and measured horizontal magnetic field of single magnets at a distance $d = 3.5\,\mathrm{mm}$.

The plots of the experimental results look similar to the plots of the computational ones. The overall shape of the fields as well as their strength match in good approximation. The row-wise blurriness of some plots can be explained by the row-wise sequence of the measurements. There is, however, an interesting characteristic of the experimental plots. The field seems to be slightly increased on the top left corner of the magnets. Since this increase only appears on the top left corner, although the magnets were positioned randomly with respect to the corners, this abnormality can not originate from the magnets, or rather it is highly unlikely that it does. A possible explanation could be a small additional field generated by a part of the working table or the stepping motors, but this assumption could not be checked properly.
Despite the precaution mentioned above, one of the 19 magnets was displaced by the probe during the measurement of its field. This resulted in a distorted plot which can be seen in figure 5.8.

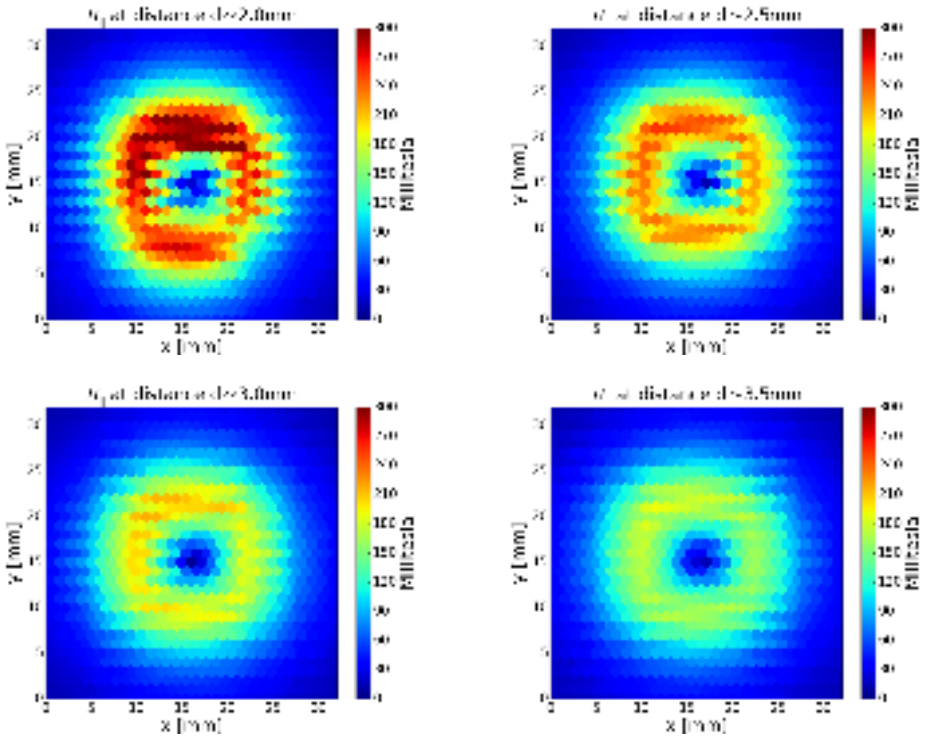

Figure 5.8.: Plots of the horizontal magnetic field of a single magnet which was displaced during the measurement. The plot of the shortest distance is distorted due to the displacement. Since this distance was measured last, the other plots are not affected.

Aside from this graphical comparison, obtained values of the strength of the field were compared as well. The maximum values of the horizontal fields of the individual magnets are given in table 5.1. A comparison with the maximum values of the computed field shows that the average values correspond to distances slightly smaller than assumed ($\simeq -0.2\,\mathrm{mm}$). In addition, the mean value of the field at certain distances was determined for selected magnets. Compared to the mean value of the calculation, these experimental values corresponded to slightly higher distances ($\simeq 0.2\,\mathrm{mm}$). Taking both conclusions into account, the distance assumption made beforehand can most likely be accepted as true. All in all, the experiment reproduces the expected results to a great extent.

Table 5.1.: Maximum values of the measured horizontal magnetic fields. The rows correspond to the individual magnets, whereas the columns correspond to the particular distances. The average values conform to the computed ones at distances $d = 1.8\,\mathrm{mm}, 2.3\,\mathrm{mm}, 2.8\,\mathrm{mm}, 3.3\,\mathrm{mm}$.

	2.0 mm	2.5 mm	3.0 mm	3.5 mm
1	293	244	208	178
2	294	246	208	179
3	312	247	210	181
4	300	254	213	188
5	299	252	214	184
6	305	254	217	187
7	301	252	213	183
8	298	250	212	180
9	302	253	213	183
10	301	251	214	183
11	302	252	214	183
12	299	250	213	183
13	300	252	213	184
14	295	246	209	180
15	299	250	213	182
16	299	251	211	182
17	300	246	211	181
18	291	245	208	179
19	288	239	203	177
average	299	249	211	182

5.3. Glueing process

As already mentioned, the construction of a Halbach array includes the fixation of the magnets to compensate the repellent and torsional forces, for example by glueing the magnets together. This section presents how the preliminary Halbach arrays were glued.

Preparations

The first step in the process of glueing is the selection of magnets. A small fraction of the magnets show little dents on the surface. Even if most of these dents should not affect the magnetic field strength nor the glueing capability, the magnets showing them are shelved in favour of the ideal coated looking magnets. The orientation of the poles of the selected magnets is then checked via a reference magnet and a corresponding mark is set to the upper face.
The next step is the preparation of a rail in which the magnets can be pushed together in-line. This can be done by fixating two plates of aluminium with straight edges onto a bigger magnetic plate which in addition fixates the magnets in the lower direction. The correct distance between the plates as well as their parallel orientation is ensured if a stack of unused magnets is placed between them while fixating the second plate. The sheet pinched between the plates prevents the glue to seep between the magnets and the lowermost magnetic plate. It is also easier to move the magnets over the smooth surface of the sheet compared to the rough surface of the plate. The fully prepared rail is shown in figure 5.9.
After this, the next step is the improvement of the adhesion between the magnets and the glue. For a better mechanical adhesion the surface of the magnets should be roughened. For this purpose, all faces which will be glued to other faces are processed with sandpaper. After this, these faces are cleaned with isopropanol to wash off dust and grease residuals. This improves the adhesion on a chemical base.

Figure 5.9.: The fully prepared rail used for the fixation of the magnets while glueing them together. Its components are described above.

Glueing

The glue is then applied to the roughened and cleaned faces and the magnets are placed inside the rail (as shown in figure 5.10). The closer they are placed the easier it gets to push them together, but they should not be placed too close to prevent unwanted movements due to repulsion. The magnets are orientated such that the field increases on the upper side. This later eases the detachment of the array. As soon as every magnet is in position, a second smaller magnetic plate is put on top to fixate the magnets in the upper direction (as shown in figure 5.11(a)). After 10 minutes of hardening, the glue is ready and the magnets are then pushed together from both sides, in this case via two steel plates. For good results, the pressing power in this process is more important than the pressing duration. After this, the setup (figure 5.11(b)) rests untreated for a couple of days to further harden the glue and gain an inner balance.

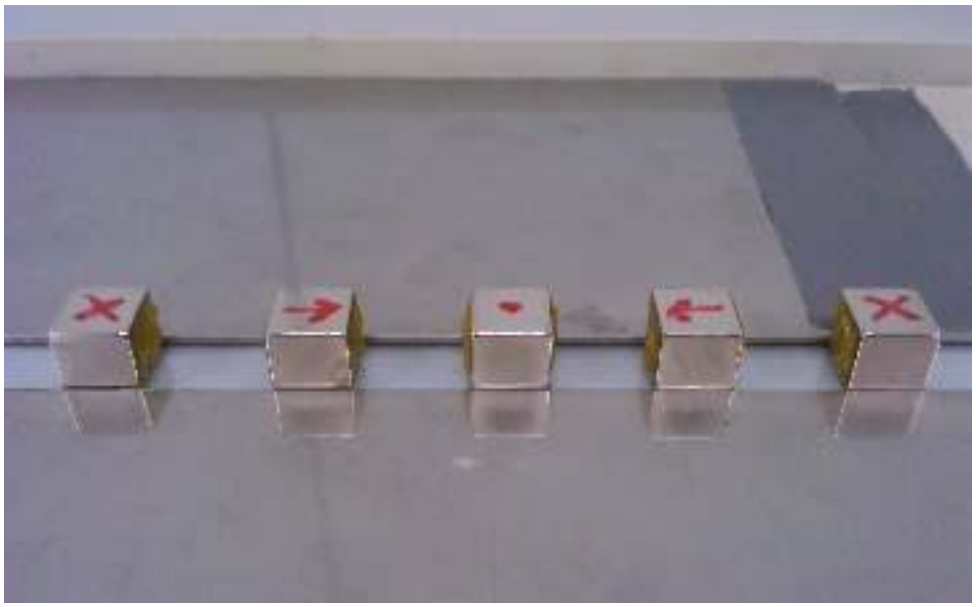

Figure 5.10.: Magnets placed inside the rail with glue put on the inner faces. The marks on the upper faces indicate the direction of magnetization; the arrows point towards the south pole which is indicated by the dot. The cross indicates the north pole. This is in analogy to the sketches in figures 4.3 to 4.5

(a) magnets in rail before being pushed together

(b) magnets in rail after being pushed together

Figure 5.11.: Figure (a) shows the magnets from figure 5.10 with a second magnetic plate put on top and two steel plates on the sides. The magnetic plate is covered in a sheet. The steel plates are used to push the magnets together. After this, in figure (b) the magnets are fixated in every direction. This setup rests untreated until the glue hardened.

Since the magnetic field is higher on the upper side, the force is stronger between the array and the smaller plate than between the array and the bigger plate on the ground. Therefore, the array sticks to the smaller plate when it is detached (as shown in figure 5.12). The array and the plate can then be uncoupled by laying the array on the edge of a desk or a similarly flat surface and then pushing the plate downwards. Again, the sheet around the plate ensures that the array is not glued to the plate and also eases the movement across it.

Figure 5.12.: The glued magnets from figure 5.11(b) after detaching them after the glue hardened. Since the magnetic field is stronger on the upper side, the array sticks to the upper plate. This plate is smaller and it is therefore easier to release the array afterwards from this one than from the bigger lower plate.

Failures

The process depicted above is a result of various attempts and failures. First tests were made without using the magnetic plates below and above the magnets. Instead, the magnets were put in a rail and then fixated by hand while pushing them together. This insufficient fixation caused some magnets to move upwards. This was attempted to be compensated with more pressure on these magnets. As a result, the coating of these magnets cracked or entire fractions at the edges broke off. Examples of the damaged magnets are shown in figure 5.13.

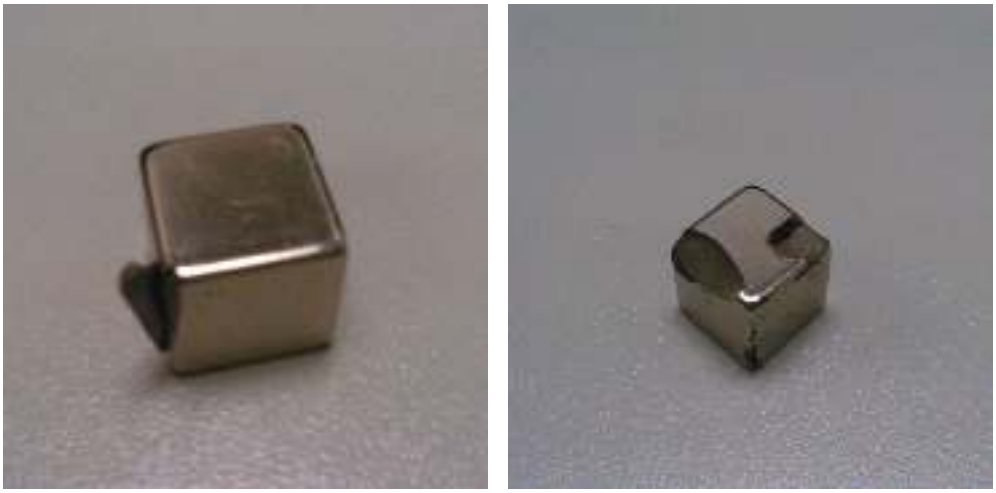

(a) magnet with cracked coating (b) magnet with splintered edges

Figure 5.13.: Examples of damaged magnets. Figure (a) shows a magnet whose coating is cracked on the left face, such that a part of the coating overhangs. Figure (b) shows a magnet with two splintered edges. In contrast to the other one, not only the coating but also the magnetic core is damaged. Both sorts of damage can occur if too much pressure is applied to the magnets. This was on the one hand the case in early attempts to glue magnets together, as described in the text. On the other hand, it occurred during preparations or transferring, when magnets were stored too close together and collided uncontrolled as a result of the magnetic attraction.

These first tests as well as the following ones were made using common glue for modelling ("greven Hart Kleber"). As this was not strong enough to compensate the repellent and torsional forces, the array formation broke just a couple of seconds after releasing it from the upper plate. After this, stronger glue ("UHU Metall") was tested, but with similar results. A longer lifespan of about 20 - 30 seconds was the only progress made in the first test with the new glue. As a consequence, the glueing process was extended with the sandpaper and the isopropanol treatment and the resting time was expanded from one or two days to about a week. After applying these changes, the second glue proved to be sufficient to get a stable Halbach array, whereupon it was used ever since.

The last improvement in the process was achieved by introducing the sheet between the lower plate and the magnets. The upper plate was covered in a sheet from the start, whereas the second sheet was added later on after a failed attempt. In this one, glue seeped underneath three adjacent magnets such that not only a magnetic but also an additional adhesive attraction between these magnets and the lower plate appeared. This combined attraction was naturally stronger than the adhesive attraction between the magnet with seeped glue and the neighbouring one without seeped glue. This resulted in the breaking of the array while trying to detach it; the three mentioned magnets stuck to the lower plate and the other two stuck to the upper one, as shown in figure 5.14.

Figure 5.14.: A 5x1 array damaged while being detached from the lower plate. As a result of glue seeping between the three magnets on the left and the lower plate, their attraction was stronger than the adhesive attraction between the three magnets on the left and the two magnets on the right. Hence, the attempt to detach the array resulted in the breaking of the array.

Another source of errors is the thickness of the layer of glue between the magnets. A characteristic of glue is that there is a middle range of widths at which it delivers the highest adhesion. Both insufficient and excessive glue is not able to maintain this level of adhesion. It is therefore important to apply the right amount of glue to maximize its efficiency. Otherwise, the magnets can probably not be held in place, as shown in figure 5.15.

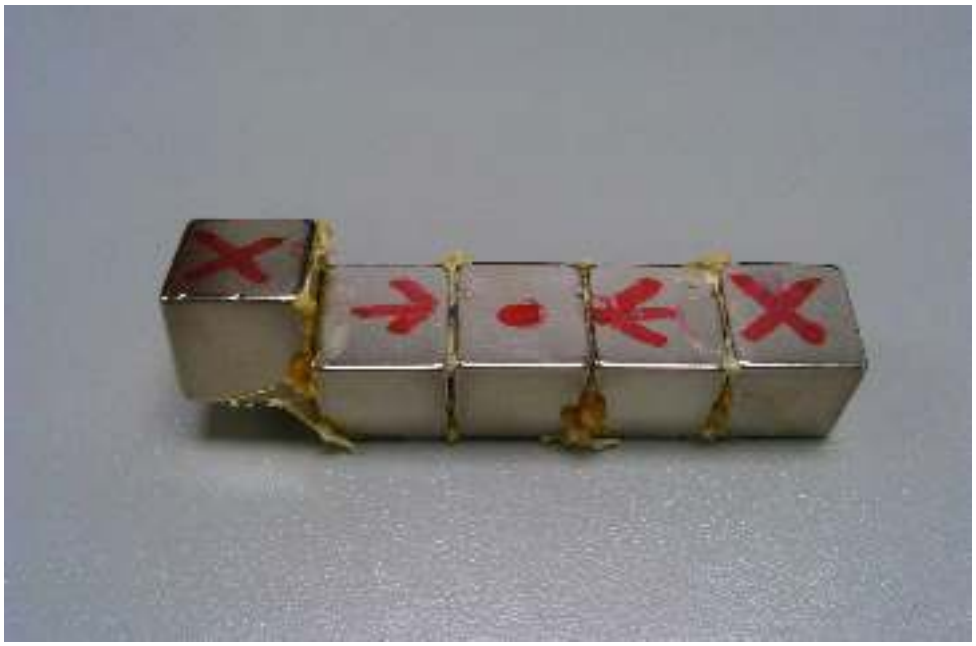

Figure 5.15.: A 5x1 array with one of the outermost magnets out-of-band. This is a result of too much glue applied between this magnet and the neighbouring one. It can also occur if too less glue is used or, regardless of the amount of glue, if there are external forces exerted on the outermost magnet after the array is detached and stored.

5.4. One-dimensional 4x1 Halbach arrays

The subject of the second phase of the preliminary measurements is a one-dimensional Halbach array consisting of four magnets, hence a 1D Halbach unit. In analogy to the single magnet measurements, the main task is the comparison between the computational (see section 4.3) and the experimental results. For this purpose, two Halbach units were constructed by glueing the magnets together as described in section 5.3. The units are shown in figure 5.16. They are both not perfectly planar but still smooth to a good extent. Due to the thickness of the layers of glue, the units possess a length of $\simeq 49\,\mathrm{mm}$. Contrary to this, the computation shows the results of an ideal unit without space between the magnets, i.e. with a length of 48 mm.

The parameter used for the comparison is, again, the horizontal magnetic field strength at various given distances above the unit. The measurements are taken in analogy to the previous measurements. They take place above the side of the unit where the field is increased due to the Halbach structure.
The results for the first unit, both computational and experimental, are presented in figures 5.17 and 5.18. Compared to the single magnet measurements in section 5.2, the distance between the probe and the magnets is higher. This has two reasons: on the one hand, this is due to the magnets not being perfectly planar, as mentioned above; on the other hand, this is caused by small amounts of glue sticking to the top side of the unit, as shown in figure 5.16. These facts induce that the boundary point is a few mm higher than the average height of the unit. Therefore, the probe has to be at a higher distance to not get stuck at the unit while running above it.
The comparison shows that the experimental results are in good accordance with the computational ones. The measured field is slightly smaller, especially above the horizontally orientated magnet lying between the two vertically orientated magnets. Furthermore, the field is not as symmetrical as the computed one. Nevertheless, taking the differences due to the glueing process and the uncertainties due to the way of measuring into account, the overall form and strength fit well to the prediction. The same applies to the second unit. Its results can be found in appendix B. Note that the measurements of the two units differ in their absolute distances, but not in their pattern. This is due to the fact that the position of the probe relative to the working table was unintentionally changed. This remained undetected and so the measurements were taken with the same initial values. However, since it is not crucial for the comparison with the calculation that the measurements of the respective units are taken at the exact same distances and since the change was detected while analysing the data, the measurement was not rerun.

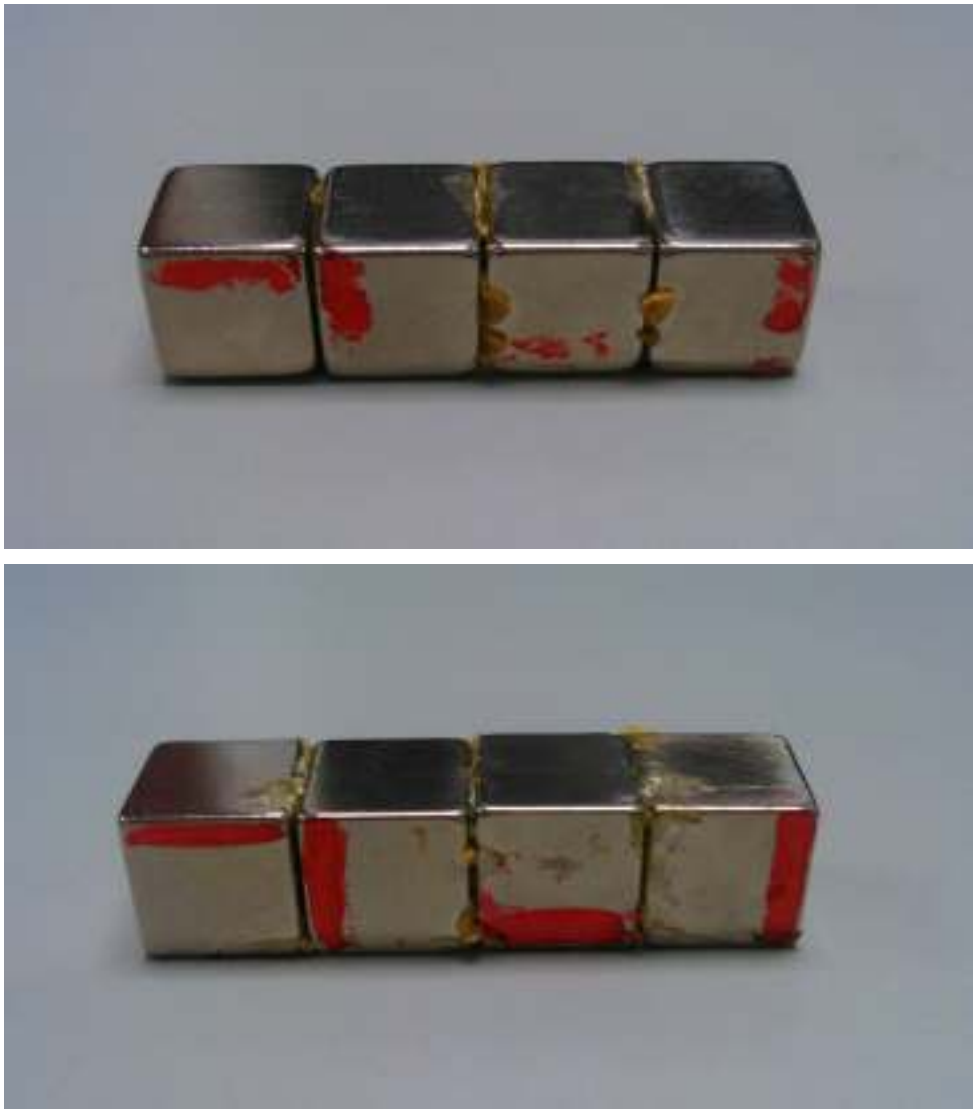

Figure 5.16.: The 2 constructed 1D Halbach units. The red bars indicate the south poles of the magnets. It is clearly visible that there is some space between the individual magnets due to the glue. The unit is therefore slightly wider than the sum of the 4 magnets. In the middle of the lower unit it is also visible that the arrangement is not perfectly planar. This also applies to the upper unit, though it is harder to see in this image.

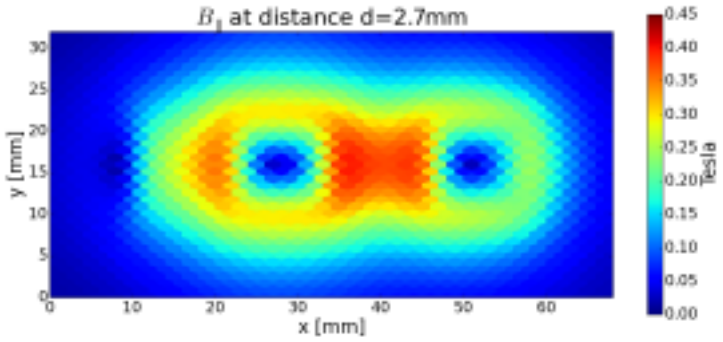

(a) Computation at 2.7 mm above the unit

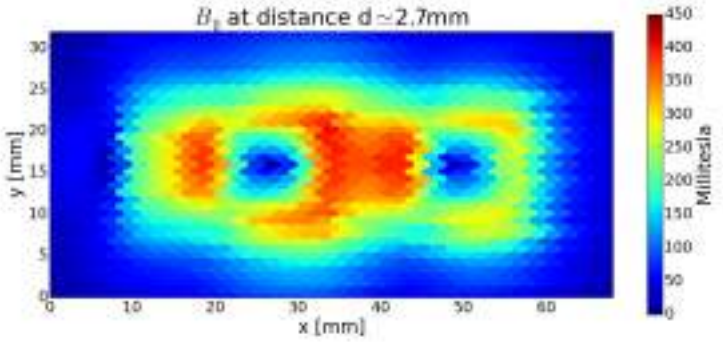

(b) Measurement at 2.7 mm above the unit

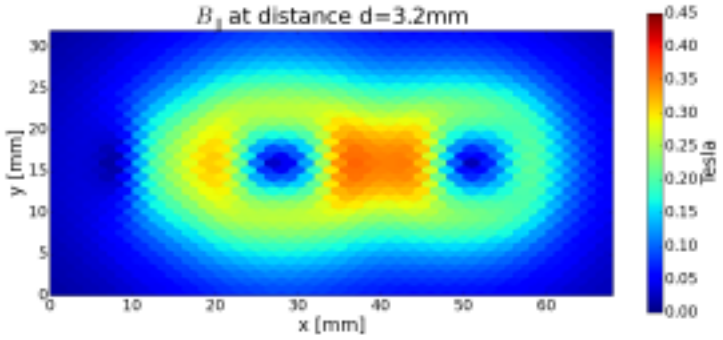

(c) Computation at 3.2 mm above the unit

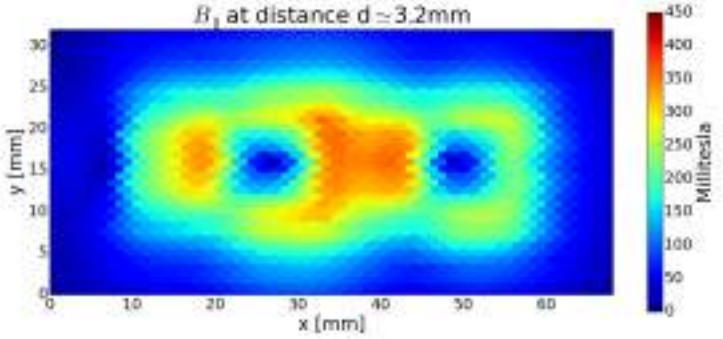

(d) Measurement at 3.2 mm above the unit

Figure 5.17.: Plots of the computation ((a) and (c)) and the measurement ((b) and (d)) of the horizontal magnetic field of the first 1D Halbach unit at a distance above the unit of 2.7 mm and 3.2 mm respectively.

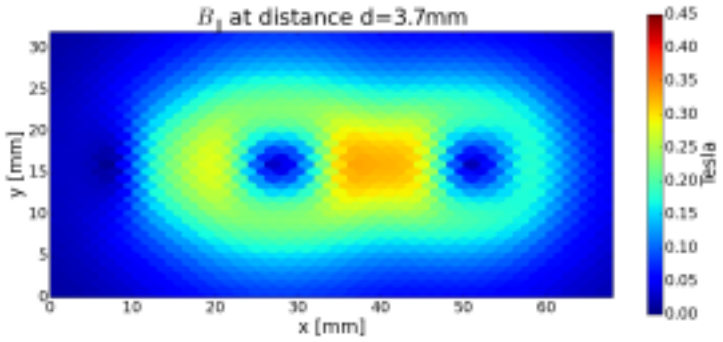

(a) Computation at 3.7 mm above the unit

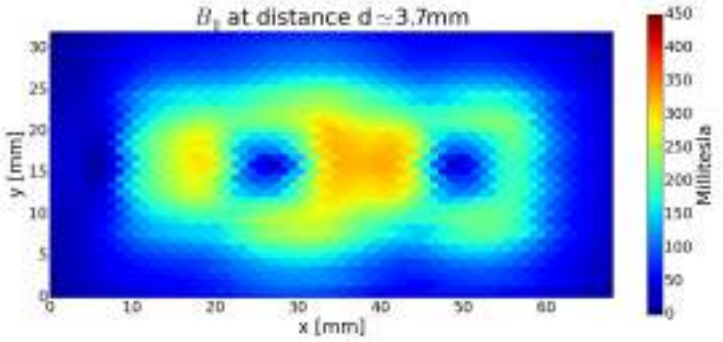

(b) Measurement at 3.7 mm above the unit

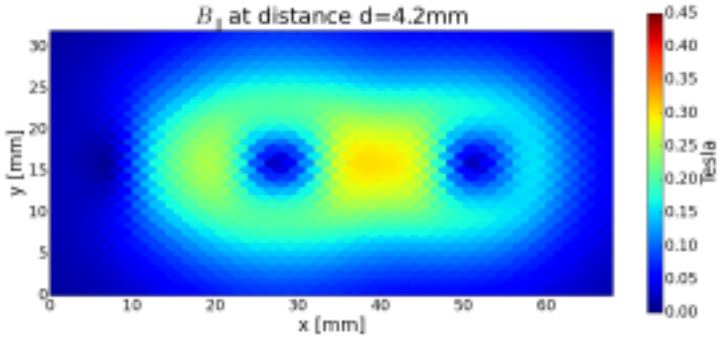

(c) Computation at 4.2 mm above the unit

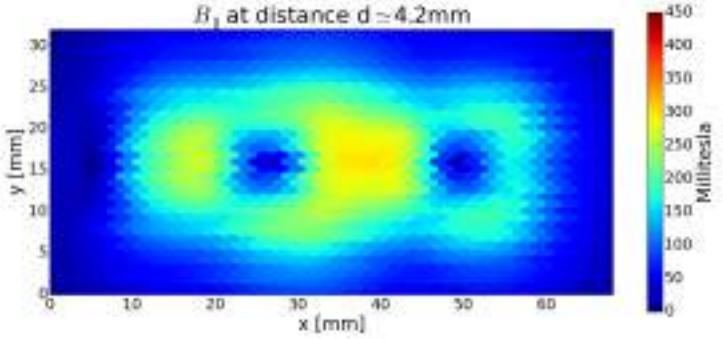

(d) Measurement at 4.2 mm above the unit

Figure 5.18.: Plots of the computation ((a) and (c)) and the measurement ((b) and (d)) of the horizontal magnetic field of the first 1D Halbach unit at a distance above the unit of 3.7 mm and 4.2 mm respectively.

5.5. Two-dimensional 5x5 Halbach array

The computations for the 5x5 and 17x17 arrays are, in analogy to the 4x1 computation, based on an ideal array without any space between the magnets. For a real array, this is hardly possible to reach due to the necessary glue. Considering the comparison of the computed and the experimentally measured one-dimensional Halbach array in section 5.4, it is therefore expected that a real two-dimensional array would generate a slightly smaller horizontal field. To test whether this is the case and, if so, how big the difference is, it was attempted to construct a real 5x5 array. As highlighted in the last chapter, this array was planned to be constructed according to the arrangement called "Parallel: all magnets". Hence it would consist of five one-dimensional Halbach units constructed with five magnets each. In a first step these Halbach stripes were constructed according to the instruction given in section 5.3. They are shown in figure 5.19. To test the similarity of these five stripes, their magnetic fields were measured at two distances above the high-field side. It turned out that the fields are sufficiently similar in the overall shape and peak strength. The corresponding plots can be found in appendix C.

Figure 5.19.: The five 5x1 Halbach stripes constructed to be the components of the 5x5 Halbach array. The symbols on the upper surfaces are analogue to the ones in figure 5.10. The distance between them is nearly the minimal distance without them reacting to each other.

The second step was to glue the stripes together in parallel. For this purpose some changes had to be made to the existing glueing process. This is due to the normal force between the equally directed, neighbouring magnets. In a row of five of such magnets with a distance of 0.5 mm between each of them, a total force of $F_{\text{normal}} = 39.60\,\text{N}$ is exerted onto the outer magnets. For smaller distances of 0.1 mm the normal force adds up to $F_{\text{normal}} = 46.75\,\text{N}$. Since this normal force is acting perpendicularly to the glued faces, it was assumed that the glue could be strong enough to compensate it. However, further preliminary measurements for BRASS discussed in [52] revealed that this could only apply if the glue is already hardened. For these measurements, three equally directed magnets were glued together. While still hardening, neither the glue nor the steel plates were capable of holding the magnets exactly in place. Instead, the glue was stretched due to the repulsion. This resulted in a stable but extended array which is shown in figure 5.20.

Figure 5.20.: Setup of different preliminary measurements for BRASS. The magnets were glued together as described in section 5.3. Due to the normal force between the magnets, the glue was stretched while hardening. The array is therefore stable but includes measurably large gaps between the magnets. See [52] for further detail.

Without adjustments to the glueing process the 5x5 array would possess the same extension in one of the two directions. To get a better comparison with the computation as well as for symmetry reasons, this is undesired and should be avoided. To do so, a new glueing setup with a new rail was prepared which is shown in figure 5.21.

Figure 5.21.: The new rail for the glueing process. Again, the basis is an iron plate. The four aluminium plates with the long holes can be moved in one direction each. Once they are positioned correctly, they can be fixed via the screws and the nuts. In a first step the "upper" plate (related to the figure) and the one on the right side are fixed. After the stripes are put onto the iron plate and brought into line with the edges, the "lower" plate is moved towards them and then also fixed. This way, the stripes are bound in three directions. The plate on the left side can then be used to push them together and, after also being fixed, bound them in the remaining direction.

Aside from the new possibilities of aligning and fixating the constituents, the main part of the process stayed unchanged. The surfaces to be glued together were already roughened up while preparing the glueing of the 5x1 stripes. These faces were then once again cleaned with isopropanol and afterwards covered with glue. The stripes prepared this way were put into the rail and capped with the small iron plate. This is shown in figure 5.22.

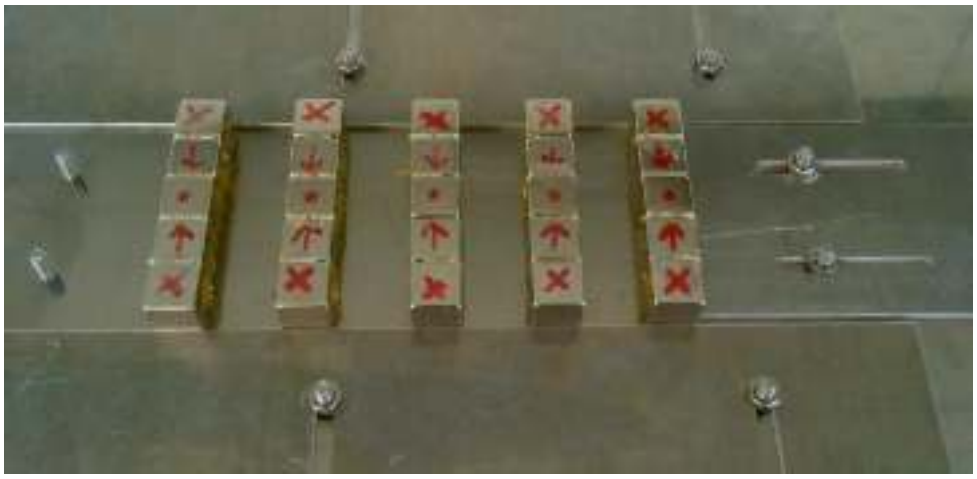

(a) stripes in rail before being pushed together

(b) stripes in rail capped with an iron plate before being pushed together

Figure 5.22.: The stripes put into the rail with glue applied to the inner faces, in analogy to figures 5.10 and 5.11(a). Figure (a) shows the situation after the first three aluminium plates were fixed via the screws and nuts. To fixate the stripes in every direction, they are capped with a small iron plate, as shown in figure (b). In the next step the aluminium plate on the left side is used to push them together and after this also gets fixed.

Unfortunately, the attempt to push the magnets together failed. It was not possible to exert a sufficiently strong pressure onto the magnets via the aluminium plate to overcome the acting forces, both repellent between the individual stripes and attracting between the stripes and the iron plates. The result after detaching the upper plate is shown in figure 5.23.

Figure 5.23.: The result of the first failed attempt. These three stripes could be pushed together, but it was not possible to push them further towards the remaining two stripes. Although still attracted by the small iron plate, they moved a little bit away from each other due to their repellent forces. This is indicated by the glue between them: to end up in this state, the inner surfaces must have been so close that the glue drops applied to them were in contact with each other. Apparently, the glue was insufficiently strong to hold the magnets together and was elongated instead.

Afterwards, a second attempt with only two stripes was made to check if it would be easier to glue the array stripe by stripe. This time, instead of the small iron plate, a heavy block of lead was put on top of the stripes to fixate them. In addition, one of the steel plates (see section 5.3) was used for the pushing instead of the thin aluminium plate. As a matter of fact, it was indeed easier to push the stripes together this way. Nevertheless, this attempt also failed, since one of the stripes flipped over, as shown in figure 5.24.

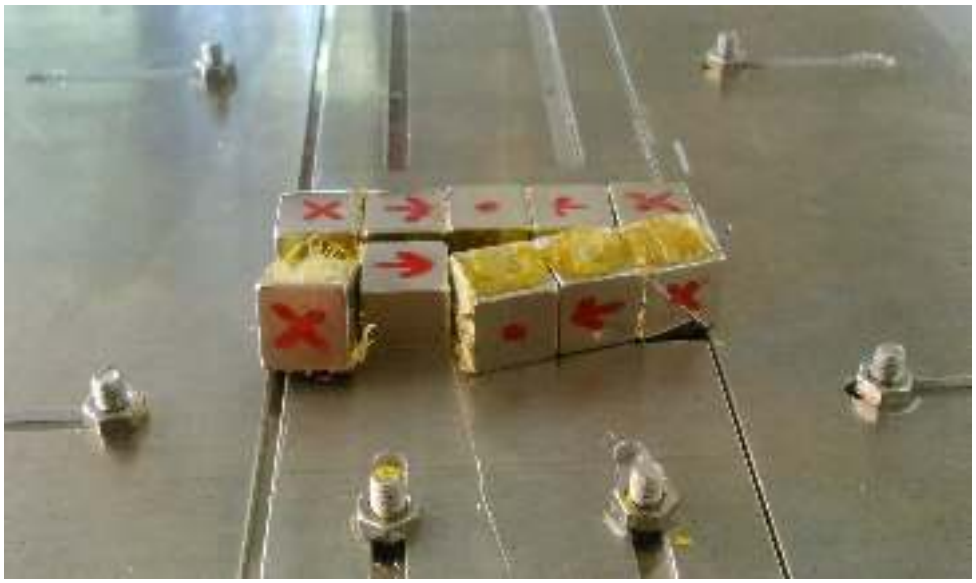

Figure 5.24.: The result of the second failed attempt. In this attempt, a heavy block of lead was put onto these two stripes instead of the small iron plate. The stripes were pushed together with one of the steel plates. Apparently, the so exerted pressure was too large for the aluminium plate on the right side (below in this picture) to stop and fixate the stripes. Therefore, the right stripe broke at two points and four of the five magnets flipped over the aluminium plate due to the combination of the pressure and the repellent force.

It is obvious that the changes applied to the glueing process were not effectual. To be able to construct a 5x5 Halbach array, it is mandatory to search for further improvements. These two failed attempts helped to draw the following conclusions regarding the new rail and the glue.

- As already mentioned, the new aluminium plate was not suitable for pushing the stripes together. It is assumed that this is mainly due to its dimensions, especially its small thickness, and its firmness. In the second attempt, the pushing was successfully done using the steel plate which is bigger and firmer. Although in this attempt only two stripes were used, the difference was great enough to assume that the steel plate should be more suitable for attempts with five stripes.
  It may also be worth considering to replace one of the iron plates with non-magnetic plates to avoid the attracting forces between them and the stripes. The function of the lower plate, namely the fixation of the stripes and the prevention of them losing their alignment, can in principle be undertaken by a suitably rigid rail. As an advantage of this replacement, the stripes could be moved easier due to the missing attracting forces. The absence of these forces would, however, also result in the necessity of building a bigger rail, since the repellent forces between the stripes could not be compensated. The function of the upper plate is to fixate the stripes and prevent them from moving upwards due to the forces acting in z-direction (see section 3.4). In the stable stripes these forces are compensated by the glue. If these stripes are being pushed together, the additionally arising forces are mainly normal forces. A heavy non-magnetic plate could therefore be sufficient to fixate the stripes. However, since the forces acting in z-direction also increase due to the additional magnets, it could be possible that the stripes lose their stability. This could result in the breaking of the stripes and hence a stable two-dimensional Halbach array would be impossible. Contrary, if the non-magnetic plate could compensate the additional forces and since the attraction between the lower plate and the array acts on the field decreasing side, it would be easier to detach the array. In summary, a replacement of the iron plates is accompanied by both advantages and disadvantages and it has to be checked if the former ones can offset the latter ones.
  Another possibility to improve the pushing could be the use of mechanical components. Since the strength of one person was not sufficient, mechanical tools like clamps could help to exert a sufficiently large pressure. However, it is obviously crucial to pay attention to the stability of the stripes, hence not all tools come into consideration.

- The new rail is in some aspects at an advantage compared to the old one. However, the situation depicted in figure 5.24 shows that it also has a disadvantage. As already mentioned, high pressure from the left side is necessary to bring the stripes together. The aluminium plate on the right side has to function as a stopping point for the stripes. However, due to its small thickness, it could not keep the outer stripe in

place. Instead, this stripe broke and parts of it flipped over the plate. To avoid this, a bigger plate could be used. Certainly though, this could possibly lead to different problems concerning the fixation via screws and nuts or the movability of the plate. Another possible solution includes an additional plate or weight put onto the screws to stop the magnets from flipping over, but it has to be tested in which way this could be realized. Note that the absence of the upper iron plate was also relevant for this incident to occur. It may not have been occurred if the iron plate had been used, so an adjustment to the aluminium plate may not be absolutely necessary.

- The glue seems to be too elastic and insufficiently strong. This is clearly visible in figures 5.20 and 5.23. The stable 5x1 stripes prove that, after hardening, the glue can compensate the acting forces if the proper amount of glue is used. However, during the process of hardening the restoring force of the glue can not counter the repellent forces between the equally directed magnets. Therefore, a different glue should be used for future attempts.
  Considering all previous results, a less elastic glue with a short hardening time is desired. In the planned 5x5 array, two types of repellent forces arise. As described in section 3.4, the normal force acts in the direction perpendicular to the long axis of the stripes and parallel to the iron plates. This force arises between magnets with parallel magnetization directions. The maximum repellent force is exerted on the edge magnets and adds up to $|F_{\text{normal,max}}| = 38.12\,\text{N}$. The shear force acting in the z-direction arises between magnets with perpendicular magnetization directions. The maximum shear force is exerted on the middle magnet and adds up to $|F_{\text{shear,max}}| = 106.8\,\text{N}$. These values are calculated for an ideal array with a given thickness of the glue of 0.5 mm. For a thickness of 0.1 mm the values of the forces are $|F_{\text{normal,max}}| = 45.10\,\text{N}$ and $|F_{\text{shear,max}}| = 125.32\,\text{N}$. Considering that these should be the upper and lower limit for the distance and also that there are further uncertainties due to the non-ideal real case, the following upper limits can be assumed:
  - $|F_{\text{normal,max}}| \leq 60.0\,\text{N}$
  - $|F_{\text{shear,max}}| \leq 140.0\,\text{N}$

  Taking the face area of the magnets of $144\,\text{mm}^2$ into account, this results in the following required properties of the new glue:
  - tensile strength $f_{\text{ten}} = 0.42\,\text{MPa}$
  - tensile shear strength $f_{\text{ten,shear}} = 0.97\,\text{MPa}$

Considering these aspects, improved attempts can be made to construct a two-dimensional Halbach array. However, due to shortness of time this can not be realized in the course of this thesis and will instead be a part of future work concerning BRASS.

6. Outlook

The first part of the preliminary measurements for BRASS, namely the analysis of single magnets and one-dimensional Halbach arrays, could be completed. The second part consisting of the analysis of two-dimensional Halbach arrays was started and computational results could already be obtained. As mentioned in the last section, the next step is the completion of this analysis by constructing a real two-dimensional array and measuring its magnetic field. After the first attempt to do so failed, another attempt to construct this array will be made considering the adjustments suggested in section 5.5. Aside from this, there are also a couple of topics which will be further analysed. These topics concern both the basic principle of the experiment and the realization of the necessary magnetic field. A selection of three of these topics is presented in this chapter.

6.1. Remanence analysis

During the preparations for the glueing of the two-dimensional array, one of the primary Halbach stripes got destroyed. This stripe had been stable for at least 4 weeks. Apart from the necessity of building a new stripe to replace the broken one, this incident also offered the chance to analyse the magnetic field of the magnets used for the stripe once more. The idea behind this renewed analysis is the fact that each magnet is exposed to the field of the other magnets. Considering the hysteretic behaviour of permanent magnets, as described in section 2.4.2, the remanence of a given magnet will presumably be affected by the field of the other magnets, especially by the one of the opposed magnet (or magnets). This would result in a loss of magnetic field strength for any given Halbach array.
For this analysis two of the five magnets were used. The first was horizontally orientated and the second was one of the outer, vertically orientated magnets. After cleaning them from the remaining glue, their field was measured in analogy to the single magnet measurements described in section 5.2. To test the impact of environmental influences, the field of a so far unused magnet was also measured. The maximum values of the horizontal fields at various distances above the magnets are given in table 6.1. For reasons of comparison, the table also includes the average values of the series of single magnet measurements as well as values from CST calculations based on magnets with lower remanence.

Table 6.1.: Maximum values of the magnetic field strength in mT. The rows correspond to the distance above the magnet at which the value is measured or calculated. The second and third columns correspond to the measurements of the magnets previously forming a stripe and the fourth column corresponds to the so far unused magnet. The fifth column corresponds to the average of the series of single magnet measurements. Finally, the sixth and seventh columns correspond to calculations of magnets with a remanence of 1.3 T and 1.35 T respectively.

	horizontal	vertical	unused	average	1.3 T	1.35 T
2.0 mm	270	268	287	299	272	282
2.5 mm	231	231	251	249	220	228
3.0 mm	200	198	213	211	196	196
3.5 mm	173	173	187	182	170	170

The magnetic field strength of these two magnets is measurably lower than the average value of the previous measurements. At the three higher distances, the values of the so far unused magnet coincide with the average values, whereas the value of the lowest distance is around 4% smaller than the average. Therefore, environmental influences can mostly be excluded, so the remanence of the two magnets has to have been decreased. A comparison with the new calculations shows that their field corresponds to a remanence between 1.3 T (matching at the lowest distance) and 1.35 T (matching at higher distances). Considering the difference between the unused magnet and the average, it is assumed that there could have been a small external influence at the lowest distance. This would mean that the remanence is more likely to be around 1.35 T. Either way, this result shows that the magnets were indeed affected by the fields of the other magnets.

This loss of magnetic field strength clearly is an undesired feature of the Halbach structure, which can barely be avoided since the interaction of the fields is necessary for the initial field increase. In addition, the loss can be assumed to be even higher in two-dimensional arrays due to the greater amount of involved magnets. However, the initial increase should still more than compensate the loss so that the field of a Halbach array is still superior to common non-Halbach arrangements. Nevertheless, further analysis regarding this feature should be the topic of future research. Examples for open questions are the maximum extent of the loss and the relationship between the loss and the primary remanence.

6.2. Asymmetric arrays

It was pointed out that the strength of the horizontal magnetic field of the 5x5 and 17x17 arrays is superior compared to the field of single magnets with the same remanence. It is simply required to arrange multiple magnets in a specific way to enhance the field like this. Nevertheless, this improvement is naturally limited as well. Since the sensitivity of BRASS is directly proportional to $\langle \mathbf{B}_{\parallel}^2 \rangle$, it would be beneficial to find arrangements generating even higher fields. For this purpose, calculations were made to check if an asymmetric structure could further enhance the field. Since there are numerous possibilities to alter the already presented arrangements, only a selection of three asymmetric structures based on the best 17x17 arrangement were calculated for a first test. The results of these calculations are presented in the following section.

Altering every magnet

The first idea is to change the dimensions of each individual magnet, but conserve the dimensions of the Halbach unit consisting of 4 magnets. This is done by altering the size of the magnets in the y-direction row-wise, alternately reducing and expanding it by the same fraction. This way, the length of two consecutive rows of magnets does not change. This type of calculation was made for the two differentials $\Delta y = 2\,\mathrm{mm}$ and $\Delta y = 3\,\mathrm{mm}$. The resulting plots of the horizontal magnetic field at a distance of 0.4 mm are given in figures 6.1 and 6.2.
In both cases, the overall shape of the horizontal field stays similar. The width of the high field areas increases compared to the symmetric array, but the field strength in these areas decreases with greater Δy. It is therefore reasonable to assume that further raising Δy will not improve the results.

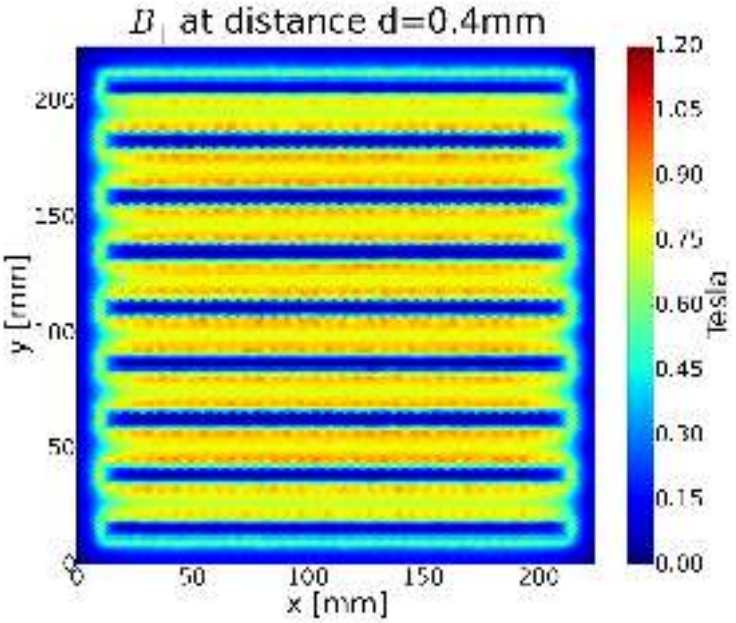

Figure 6.1.: The horizontal magnetic field of the first asymmetric array at a distance of 0.4 mm. This array consists of magnets with an edge length in y-direction of either 14 mm (horizontal orientation) or 10 mm (vertical orientation). Compared to the plot of the symmetric array (figure 4.9(b)), the width of the "bands", i.e. the area with a high field component, is enlarged. However, this is only possible at the cost of a lower peak field strength.

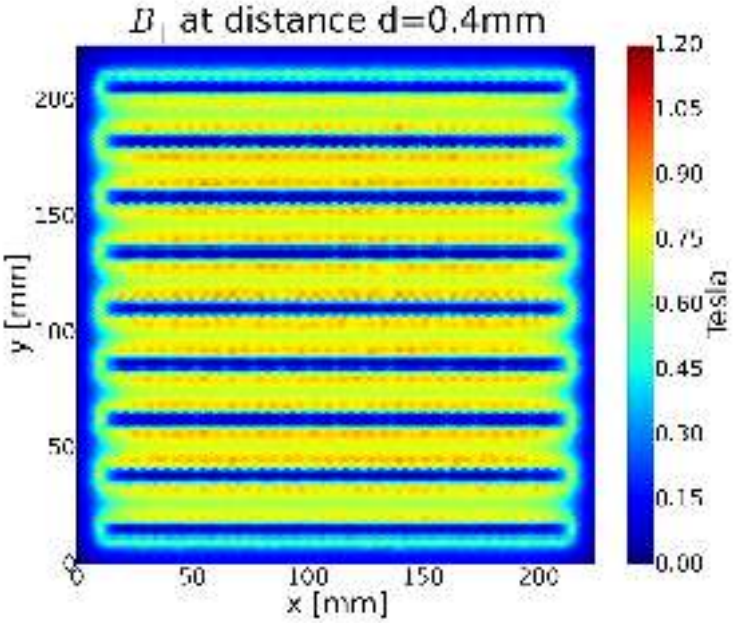

Figure 6.2.: The horizontal magnetic field of the second asymmetric array at a distance of 0.4 mm. This array consists of magnets with an edge length in y-direction of either 15 mm (horizontal orientation) or 9 mm (vertical orientation). Compared to the plot of the first asymmetric array (figure 6.1), the width of the "bands" is further enlarged resulting in an even lower peak field strength.

Altering only vertical magnets

The third calculation is based on the idea to reduce the part of the area where the horizontal field component is almost non-existent. To get such a reduction, all vertically orientated magnets are altered to half their length in the y-direction. This way, the overall area shrinks, but the ratio of high-field to low-field area rises. The resulting plot is given in figure 6.3.

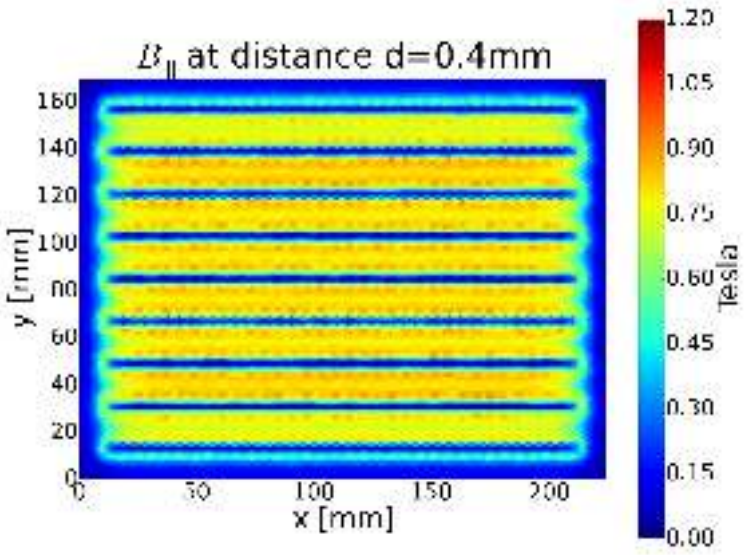

Figure 6.3.: The horizontal magnetic field of the third asymmetric array at a distance of 0.4 mm. This array consists of magnets with an edge length in y-direction of either 12 mm (horizontal orientation) or 6 mm (vertical orientation). Similar to the previous two asymmetric arrays, the "bands" are wider than in the symmetric case and the peak strength is lower. However, the ratio of high-field area to low-field area is visibly higher, contrary to the other two asymmetric arrays.

Similar to the first two asymmetric arrays, the peak strength of the horizontal field decreases. However, according to the expectations, the ratio of high-field to low-field area increases noticeably.

So far, the plots do not show an observable improvement compared to the "normal" symmetric array. Nevertheless, the decisive value is still the mean squared horizontal field strength. A comparison of the asymmetric arrays to the symmetric one with respect to $\langle \mathbf{B}_{\parallel}^2 \rangle$ is given in figure 6.4.

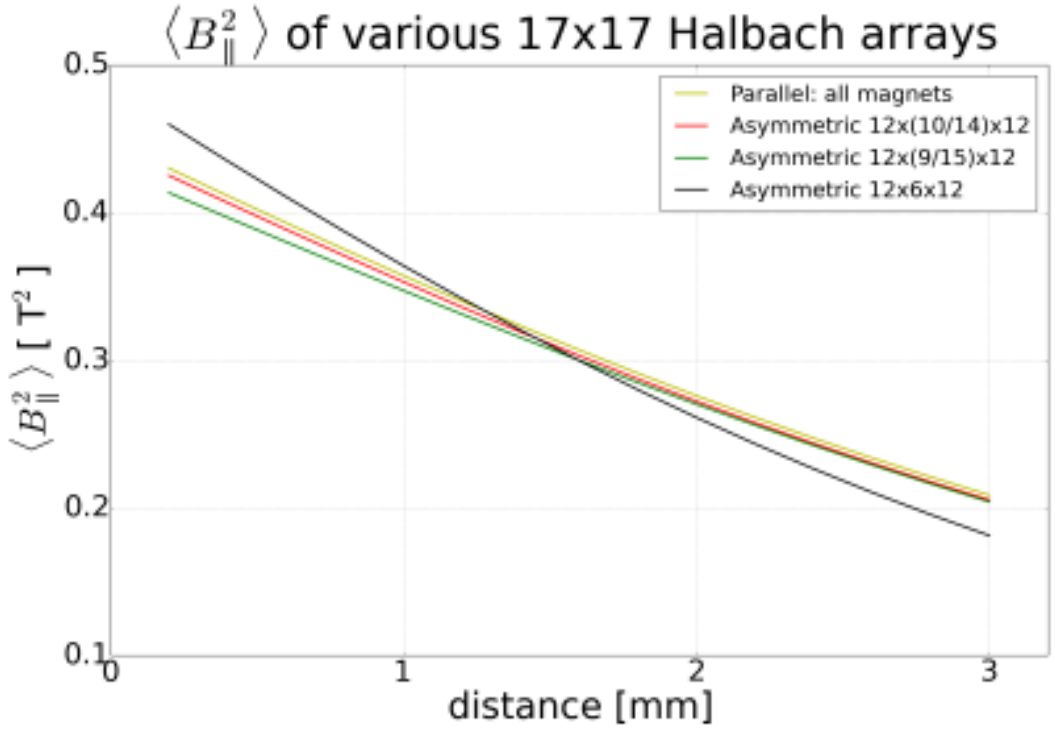

Figure 6.4.: A comparison of the asymmetric arrays to the symmetric array they are based on. This plot shows the mean squared horizontal magnetic field with respect to the distance above the high field side of the arrays. If the size of every magnet is changed as described, $\langle \mathbf{B}_{\parallel}^2 \rangle$ decreases slightly. Contrary, $\langle \mathbf{B}_{\parallel}^2 \rangle$ increases at short distances above the array if solely the vertical magnets are altered. At distances $d \gtrsim 1.5\,\mathrm{mm}$ the symmetric array still possesses the highest $\langle \mathbf{B}_{\parallel}^2 \rangle$.

The curves corresponding to the asymmetric arrays of the first category take a course similar to the one of the symmetric array. Independent of the distance above the array, their values of $\langle \mathbf{B}_{\parallel}^2 \rangle$ are smaller, but the difference to the symmetric array only varies between $0.05\,\mathrm{T}^2$ and $0.15\,\mathrm{T}^2$. Contrary, the curve of the asymmetric array of the second category is steeper than the other three. However, while providing smaller values at high distances, this array surpasses the symmetric one at distances $d \leq 1.35\,\mathrm{mm}$, with a maximum difference of $0.03\,\mathrm{T}^2$ at 0.2 mm. It should be noted that the area of this array is only about 3/4 of the area of the symmetric array. Hence, edge effects should have a slightly greater influence, which could result in higher values of $\langle \mathbf{B}_{\parallel}^2 \rangle$ if enlarged to the same size.
The comparison shows that the arrays of the first category deliver no upgrade to the symmetric array, but the array of the second category provides higher values of $\langle \mathbf{B}_{\parallel}^2 \rangle$ at lower distances. This is, however, not the case at higher distances. Instead, this array provides by far the smallest $\langle \mathbf{B}_{\parallel}^2 \rangle$ at distances $d \gtrsim 1.6\,\mathrm{mm}$ in this comparison. Considering this, it could therefore only be the favoured arrangement for specific narrowband searches. Nevertheless, the results demonstrate that it could be profitable to continue testing new ideas or modifications of already known arrangements. Hence, the search for new ways to generate higher magnetic fields will be part of future research.

6.3. Inhomogeneous B-field

In the basic principle of BRASS described in section 3 the involved magnetic field is assumed to be constant over at least one period of the WISP wavelength. However, in chapters 4 and 5 it is shown that the magnetic field generated by single magnets as well as by one-dimensional and two-dimensional Halbach arrays varies depending on the distance above the magnets and arrays respectively. Considering a maximum relevant wavelength of 3.0 mm (as described in section 4.4.1) and a two-dimensional Halbach array consisting of 17x17 magnets and constructed in the most suitable analysed configuration, the maximum decrease of the magnetic field over one whole period adds up to over 50%. This corresponds to a total difference of at least $0.22\,\mathrm{T}^2$ (see figure 4.10).
So far, it was not fully analysed how much of an influence a non-constant magnetic field has on the conversion probability of the WISPs in said field. First approaches were made in [83], but a complete analysis in the connection of BRASS should definitely be a topic of further research.

7. Conclusion

Well-motivated candidates for dark matter are the WISPs, which are particles with masses in the sub-eV range interacting weakly with Standard Model particles. The most prominent ones are the axion, axion-like particles and hidden photons, with the former two only interacting in the presence of a magnetic field. There are already various experiments designed for the search for these particles. A newly proposed one is BRASS in Hamburg, which is based on the assumption that WISPs can convert into photons at reflective surfaces. Compared to other haloscopic experiments, especially resonant cavity searches, BRASS offers the potential for broadband measurements without scanning.
One planned feature of BRASS is a magnetic field generated by magnets which are structured in a Halbach array. First preliminary analyses regarding those magnets and arrays on small length scales were made and presented in this thesis. These analyses are based on cubic magnets with an edge length of 12 mm. In a first phase, the horizontal magnetic fields of single magnets and one-dimensional Halbach arrays consisting of four magnets (a so-called Halbach unit) were computed. The results were then compared to results from magnetic field measurements which were taken using a Hall probe. In this context, a method of constructing one-dimensional Halbach arrays by glueing the magnets together was introduced and performed. Both comparisons showed conformity in good approximation. The second phase focuses on two-dimensional Halbach arrays. A total of seven different arrangements of quadratic arrays were computationally analysed in terms of their horizontal magnetic field and the square of that quantity. This was done for two different array dimensions. The highest values of $\langle \mathbf{B}_{\parallel}^2 \rangle$ are provided by an array consisting of rows with equally directed magnets; in other words consisting of five one-dimensional Halbach stripes in parallel. To again compare the computational results to experimental ones, an attempt to construct a two-dimensional array arranged as mentioned was made. For this purpose, the glueing method was expanded and enhanced. Regardless of these preparations, the attempt was unsuccessful. However, important information regarding the restrictions of the glueing method was gained and further attempts are already planned.

The results of the preliminary measurements show that Halbach arrays could offer specific benefits for the search for WISPs. However, their whole potential is not fully determined yet. There are definitely some possibilities to further enlarge their utility for haloscopes like BRASS. The future of this experiment is therefore dual. Aside from the ongoing analysis of Halbach arrays, further measurements are already in preparation. As soon as the preliminary measurements for the two-dimensional case are finished, BRASS will enter the next experimental stage which focuses on first test measurements with fully constructed two-dimensional Halbach arrays.

List of Figures

Bibliography

[1] J. S. Bullock and M. Boylan-Kolchin. Small-Scale Challenges to the ΛCDM Paradigm. *Ann. Rev. Astron. Astrophys.*, 55:343–387, 2017.

[2] P. A. R. Ade et al. Planck 2015 results. XIII. Cosmological parameters. *Astronomy & Astrophysics*, 594:A13, 2016.

[3] K. Baker et al. The quest for axions and other new light particles. *Annalen der Physik*, 525(26):A260000–A99, 2013.

[4] J. Jaeckel and A. Ringwald. The Low-Energy Frontier of Particle Physics. *Annual Review of Nuclear and Particle Science*, 60:405–437, 2010.

[5] A. Ringwald. Exploring the Role of Axions and Other WISPs in the Dark Universe. *Physics of the Dark Universe*, 1:116–135, 2012.

[6] P. Bull et al. Beyond ΛCDM: PProblem, ssolution, and the road ahead. *Phys. Dark Univ.*, 12:56–99, 2016.

[7] D. Horns, J. Jaeckel, A. Lindner, A. Lobanov, J. Redondo, and A. Ringwald. Searching for WISPy Cold Dark Matter with a Dish Antenna. *Journal of Cosmology and Astroparticle Physics*, 2013(04):016, 2013.

[8] K. Halbach. Design of Permanent Multipole Magnets with Oriented Rare Earth Cobalt Materials. *Nuclear Instruments and Methods*, 169(1):1–10, 1980.

[9] CERN. Dark Matter. home.cern/about/physics/dark-matter. accessed on 13-09-17.

[10] F. Zwicky. Die Rotverschiebung von extragalaktischen Nebeln. *Helvetica Physica Acta*, 6:110–127, 1933.

[11] V. C. Rubin and W. K. Ford Jr. Rotation of the Andromeda Nebula from a Spectroscopic Survey of Emission Regions. *Astrophysical Journal*, 159:379, 1970.

[12] G. Bertone, D. Hooper, and J. Silk. Particle dark matter: evidence, candidates and constraints. *Physics Reports*, 405:279–390, 2005.

[13] V. C. Rubin, W. K. Ford Jr., and N. Thonnard. Rotational Properties of 21 Sc Galaxies with a Large Range of Luminosities and Radii, from NGC 4605 (R = 4 kpc) to UGC 2885 (R = 122 kpc). *The Astrophysical Journal*, 238:471–487, 1980.

[14] G. Bertone. *Particle Dark Matter: Observations, Models and Searches*. Cambridge University Press, 2010.

[15] http://hubblesite.org/image/1792/news/18-gravitational-lensing. accessed on 13-09-2017.

[16] http://hubblesite.org/images/news/release/2006-23. accessed on 13-09-2017.

[17] D. Clowe et al. A Direct Empirical Proof Of The Existence Of Dark Matter. *The Astrophysical Journal*, 648:L109–L113, 2006.

[18] http://chandra.harvard.edu/photo/2006/1e0657/more.html. accessed on 13-09-2017.

[19] J. Beringer et al. (Particle Data Group) The Review of Particle Physics. *Physical Review*, D86:010001, 2012.

[20] C. Weinheimer. The Neutrino mass direct measurements. In *Neutrino telescopes. Proceedings, 10th International Workshop, Venice*, pages 335–344, 2003.

[21] V. Hannen, I. Heese, C. Weinheimer, A. Sejersen Riis, and K. Valerius. Deconvolution of the energy loss function of the KATRIN experiment. *Astroparticle Physics*, 89:30–38, 2017.

[22] L. Canetti, M. Drewes, and M. Shaposhnikov. Sterile Neutrinos as the Origin of Dark and Baryonic Matter. *Physical Review Letters*, 110:061801, 2013.

[23] C. Alcock et al. The MACHO Project: Microlensing Results from 5.7 Years of LMC Observations. *The Astrophysical Journal*, 542(1):281, 2000.

[24] P. Tisserand et al. Limits on the Macho Content of the Galactic Halo from the EROS-2 Survey of the Magellanic Clouds. *Astronomy & Astrophysics*, 469(2):387–404, 2007.

[25] V. I. Dokuchaev and Y. N. Eroshenko. Black hole atom as a dark matter particle candidate. *Adv. High Energy Phys.*, 2014:434539, 2014.

[26] S. Hawking. Gravitationally collapsed objects of very low mass. *Monthly Notices of the Royal Astronomical Society*, 152:75–78, 1971.

[27] M. Kamionkowski. WIMP and Axion Dark Matter. In *High Energy Physics and Cosmology, 1997 Summer School*, page 394, 1998.

[28] E. Aprile et al. Dark Matter Results from 225 Live Days of XENON100 Data. *Physical Review Letters*, 109:181301, 2012.

[29] R. Bernabei et al. Final model independent result of DAMA/LIBRA-phase1. *European Physical Journal C*, 73:2648–2667, 2013.

[30] M. Milgrom. A Modification of the Newtonian Dynamics: Implications for Galaxies. *The Astrophysical Journal*, 270:371–383, 1983.

[31] X. Li et al. Finslerian MOND versus observations of Bullet Cluster 1E 0657-558. *Monthly Notices of the Royal Astronomical Society*, 428:2939–2948, 2013.

[32] J. Bekenstein and M. Milgrom. Does the missing mass problem signal the breakdown of Newtonian gravity? *The Astrophysical Journal*, 286:7–14, 1984.

[33] J. Bekenstein. Relativistic gravitation theory for the modified Newtonian dynamics paradigm. *Physical Review D*, 70(8):083509, 2004.

[34] J. W. Moffat. Scalar-Tensor-Vector Gravity Theory. *Journal of Cosmology and Astroparticle Physics*, 2006(03):004, 2006.

[35] J. R. Brownstein and J. W. Moffat. The Bullet Cluster 1E0657-558 evidence shows modified gravity in the absence of dark matter. *Monthly Notices of the Royal Astronomical Society*, 382:29–47, 2007.

[36] R. D. Peccei and H. R. Quinn. CP Conservation in the Presence of Pseudoparticles. *Physical Review Letters*, 38(25):1440–1443, 1977.

[37] S. Weinberg. A New Light Boson? *Phys. Rev. Lett.*, 40:223–226, 1978.

[38] F. Wilczek. Problem of Strong P and T Invariance in the Presence of Instantons. *Phys. Rev. Lett.*, 40:279–282, 1978.

[39] J. L. Hewett, H. Weerts, et al. Fundamental Physics at the Intensity Frontier. *ArXiv e-prints*, (1205.2671), 2012.

[40] J. E. Kim. Weak Interaction Singlet and Strong CP Invariance. *Phys. Rev. Lett.*, 43:103, 1979.

[41] M. A. Shifman, A. I. Vainshtein, and V. I. Zakharov. Can Confinement Ensure Natural CP Invariance of Strong Interactions? *Nucl. Phys.*, B166:493–506, 1980.

[42] M. Dine, W. Fischler, and M. Srednicki. A Simple Solution to the Strong CP Problem with a Harmless Axion. *Phys. Lett.*, 104B:199–202, 1981.

[43] A. R. Zhitnitsky. On Possible Suppression of the Axion Hadron Interactions. (In Russian) . *Sov. J. Nucl. Phys.*, 31:260, 1980.

[44] M. Goodsell, J. Jaeckel, J. Redondo, and A. Ringwald. Naturally Light Hidden-Photons in Large Volume String Compactifications. *JHEP*, 11:027, 2009.

[45] M. Cicoli, M. Goodsell, J. Jaeckel, and A. Ringwald. Testing String Vacua in the Lab: From a Hidden CMB to Dark Forces in Flux Compactifications. *JHEP*, 07:114, 2011.

[46] M. Goodsell, S. Ramos-Sanchez, and A. Ringwald. Kinetic Mixing of $U(1)$s in Heterotic Orbifolds. *JHEP*, 01:021, 2012.

[47] P. Sikivie. Experimental Tests of the „Invisible“ Axion. *Physical Review Letters*, 51(16):1415–1417, 1983.

[48] I. Stern. ADMX Status. In *Proceeding, 38th International Conference on High Energy Physics, Chicago*, page 198, 2016.

[49] B. M. Brubaker et al. First Results from a Microwave Cavity Axion Search at 24 μeV. *Physical Review Letters*, 118(6):061302, 2017.

[50] L. H. Nguyen, D. Horns, A. Lobanov, and A. Ringwald. WISPDMX: A holoscope for WISP Dark Matter between 0.8-2 μeV. In *Proceedings, 11th Patras Workshop on Axions, WIMPs and WISPs (Axion-WIMP 2015), Zaragoza*, pages 219–223, 2015.

[51] B. Majorovits and J. Redondo. MADMAX: A new Dark Matter Axion Search using a Dielectric Haloscope. In *12th Patras Workshop on Axions, WIMPs and WISPs (AXION-WIMP 2016), Jeju Island*, 2016.

[52] M. Schmitz. Optimierung magnetisierter Spiegel für das BRASS-Experiment. Bachelor thesis, Universität Hamburg, 2017.

[53] D. M. Lazarus et al. Search for Solar Axions. *Physical Review Letters*, 69(16):2333–2336, 1992.

[54] S. Moriyama, M. Minowa, T. Namba, Y. Inoue, Y. Takasu, and A. Yamamoto. Direct search for solar axions by using strong magnetic field and x-ray detectors. *Phys. Lett.*, page 147, 1998.

[55] T. Mizumoto, R. Ohta, T. Horie, J. Suzuki, Y. Inoue, and M. Minowa. Experimental search for solar hidden photons in the eV energy range using kinetic mixing with photons. *Journal of Cosmology and Astroparticle Physics*, 1307:013, 2013.

[56] V. Anastassopoulos et al. New CAST Limit on the Axion-Photon Interaction. *Nature Physics*, 13:584–590, 2017.

[57] M. Giannotti, J. Ruz, and J. K. Vogel. IAXO, next generation of helioscopes. *Proceedings of Science*, 2016.

[58] M. Schwarz, E.-A. Knabbe, A. Lindner, J. Redondo, A. Ringwald, M. Schneide, J. Susol, and G. Wiedemann. Results from the Solar Hidden Photon Search. *Journal of Cosmology and Astroparticle Physics*, 1508(08):011, 2015.

[59] L. B. Okun. Limits on electrodynamics: paraphotons? *Soviet Physics - JETP*, 56:502–505, 1982.

[60] A. A. Anselm. Arion $\leftrightarrow$ Photon Oscillations in a Steady Magnetic Field. (In Russian). *Yadernaya fizika*, 42:1480–1483, 1985.

[61] K. van Bibber et al. Proposed experiment to produce and detect light pseudoscalars. *Physical Review Letters*, 59:759, 1987.

[62] J. Redondo and A. Ringwald. Light shining through walls. *Contemporary Physics*, 52:211–236, 2011.

[63] K. Ehret, M. Frede, S. Ghazaryan, M. Hildebrandt, E.-A. Knabbe, D. Kracht, A. Lindner, J. List, T. Meier, N. Meyer, D. Notz, J. Redondo, A. Ringwald, G. Wiedemann, and B. Willke. New ALPS results on hidden-sector lightweights. *Physics Letters B*, 689(4):149 – 155, 2010.

[64] A. Spector. ALPS II technical overview and status report. *ArXiv e-prints 1611.05863*, 2016.

[65] F.-J. Schmitt. Glossar: Magnetismus von A - Z. www.supermagnete.de/magnetismus, 2015. accessed on 17-10-2017.

[66] J. Lucas, P. Lucas, T. Le Mercier, A. Rollat, and W. G. Davenport. *Rare Earths: Science, Technology, Production and Use*. Elsevier Science, 2014.

[67] M. Sagawa, S. Fujimura, N. Togawa, H. Yamamoto, and Y. Matsuura. New material for permanent magnets on a base of Nd and Fe (invited). *Journal of Applied Physics*, 55(6):2083–2087, 1984.

[68] J. J. Croat, J. F. Herbst, R. W. Lee, and F. E. Pinkerton. High-energy product Nd-Fe-B permanent magnets. *Applied Physics Letters*, 44(1):148–149, 1984.

[69] S. Sugimoto. Current status and recent topics of rare-earth permanent magnets. *Journal of Physics D: Applied Physics*, 44(6):064001, 2011.

[70] D. Brown, B.-M. Ma, and Z. Chen. Developments in the processing and properties of NdFeB-type permanent magnets. *Journal of Magnetism and Magnetic Materials*, 248(3):432–440, 2002.

[71] J. Ormerod and S. Constantinides. Bonded permanent magnets: Current status and future opportunities (invited). *Journal of Applied Physics*, 81(8):4816–4820, 1997.

[72] M. Drak and L. A. Dobrzanski. Corrosion of Nd-Fe-B permanent magnets. *Journal of Achievements in Materials and Manufacturing Engineering*, 120(1-2), 2007.

[73] E. H. Hall. On a New Action of the Magnet on Electric Currents. *American Journal of Mathematics*, 2(3):287–292, 1879.

[74] E. Ramsden. *Hall-Effect Sensors: Theory and Application*. Elsevier Science, 2011.

[75] A. Kogut. Synchrotron Spectral Curvature from 22 MHz to 23 GHz. *The Astrophysical Journal*, 753(2):110, 2012.

[76] P. Morrison, J. Billingham, and J. Wolfe. The Search for Extraterrestrial Intelligence. *NASA SP*, 419:68, 1977.

[77] P. Arias, D. Cadamuro, M. Goodsell, J. Jaeckel, J. Redondo, and A. Ringwald. WISPy Cold Dark Matter. *Journal of Cosmology and Astroparticle Physics*, 1206:013, 2012.

[78] J. C. Mallinson. One-Sided Fluxes - A Magnetic Curiosity? *IEEE Transactions on Magnetics*, 9(4):678–682, December 1973.

[79] https://www.kjmagnetics.com/blog.asp?p=halbach-arrays. accessed on 13-09-2017.

[80] J.-P. Yonnet and H. Allag. Analytical calculation of magnet interactions in 3D. *The 7th International Symposium on Linear Drives for Industry Applications*, 2009.

[81] G. Akoun and J.-P. Yonnet. 3D Analytical Calculation Of The Forces Exerted Between Two Cuboidal Magnets. *IEEE Transactions on Magnetics*, 20(5):1962–1964, September 1984.

[82] J. M. M. Rovers, J. W. Jansen, E. A. Lomonova, and M. J. C. Ronde. Calculation of the Static Forces Among the Permanent Magnets in a Halbach Array. *IEEE Transactions on Magnetics*, 45(10):4372–4375, 2009.

[83] J. Redondo. Photon-Axion conversions in transversely inhomogeneous magnetic fields. In *Proceedings, 5th Patras Workshop on Axions, WIMPs and WISPs (AXION-WIMP 2009), Durham*, pages 185–188, 2010.

A. Plots of the single magnets

In this section the remaining plots of the single magnet measurements discussed in section 5.2 are shown. Each figure contains the plots corresponding to one specific magnet.

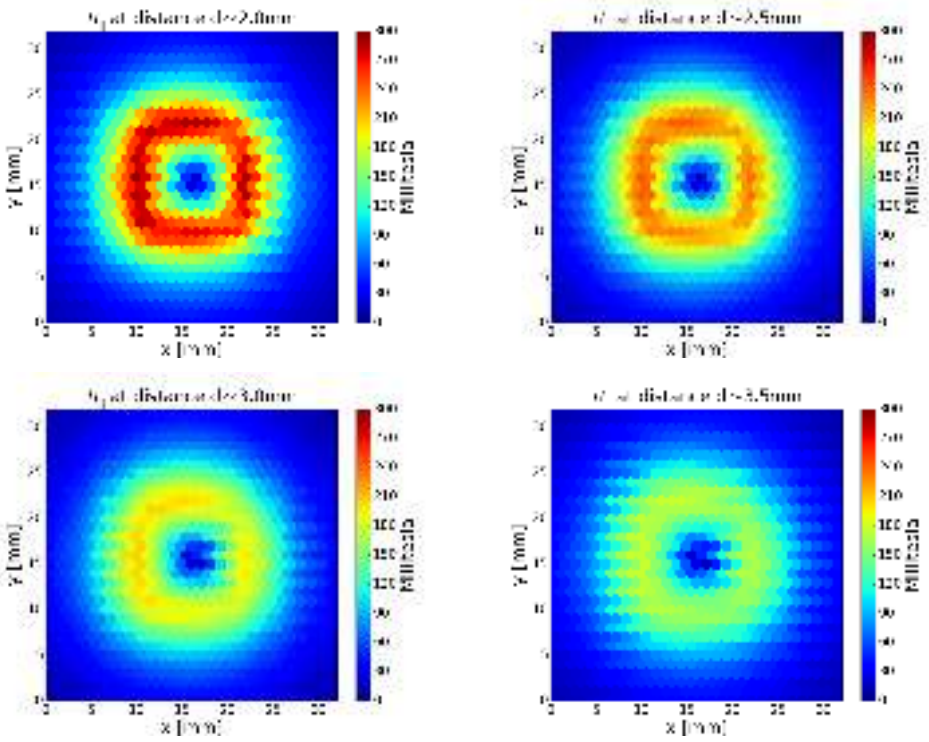

Figure A.1.: Horizontal magnetic field at various distances above the magnet 5.

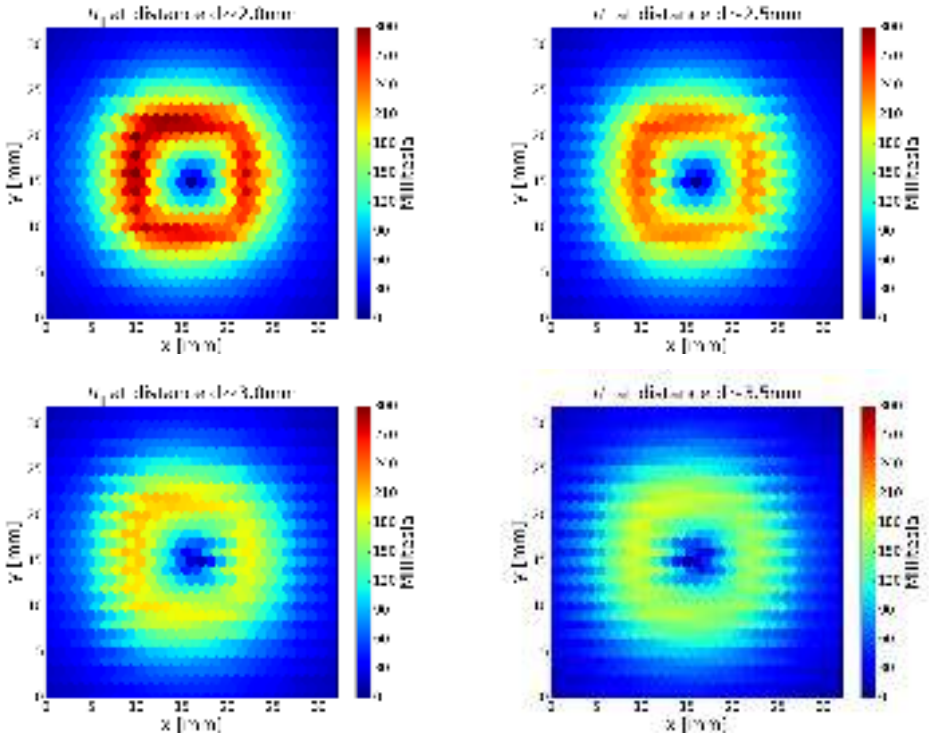

Figure A.2.: Horizontal magnetic field at various distances above the magnet 6.

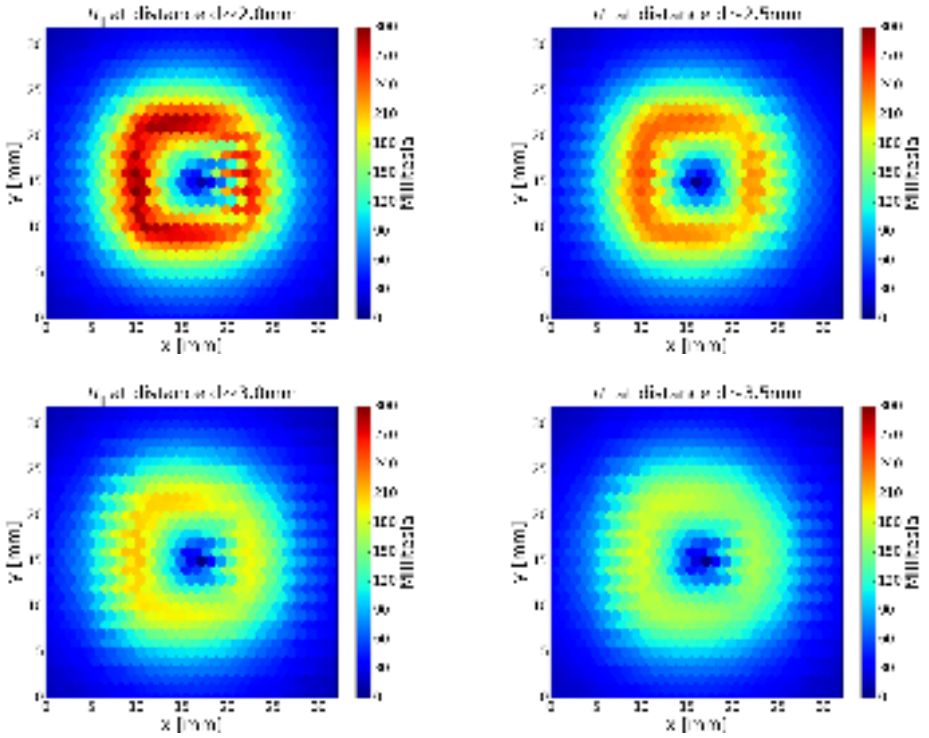

Figure A.3.: Horizontal magnetic field at various distances above the magnet 7.

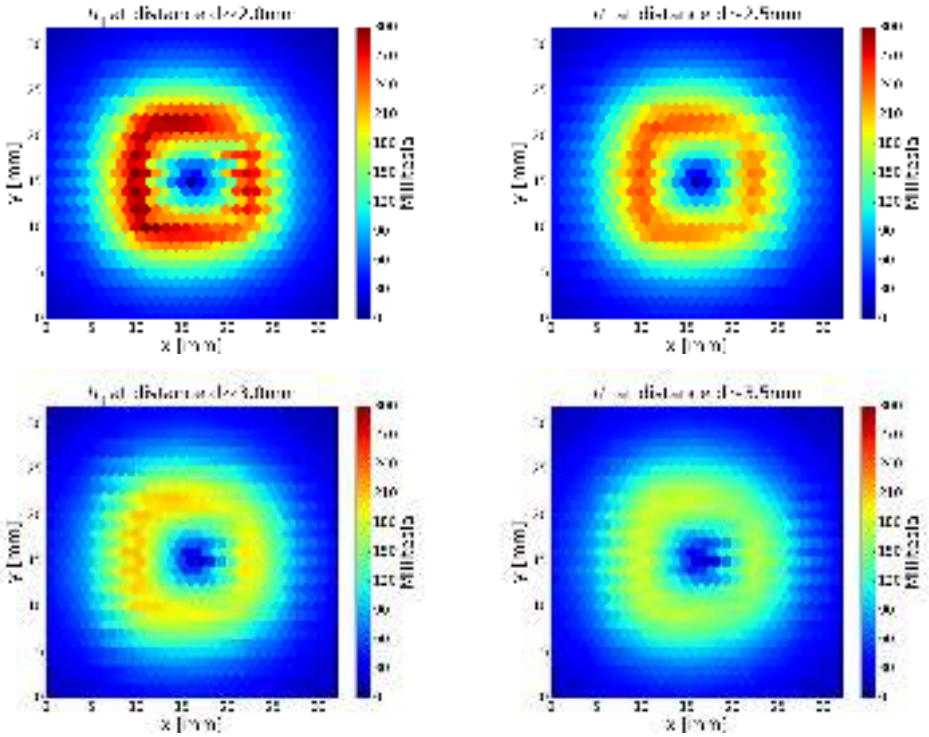

Figure A.4.: Horizontal magnetic field at various distances above the magnet 8.

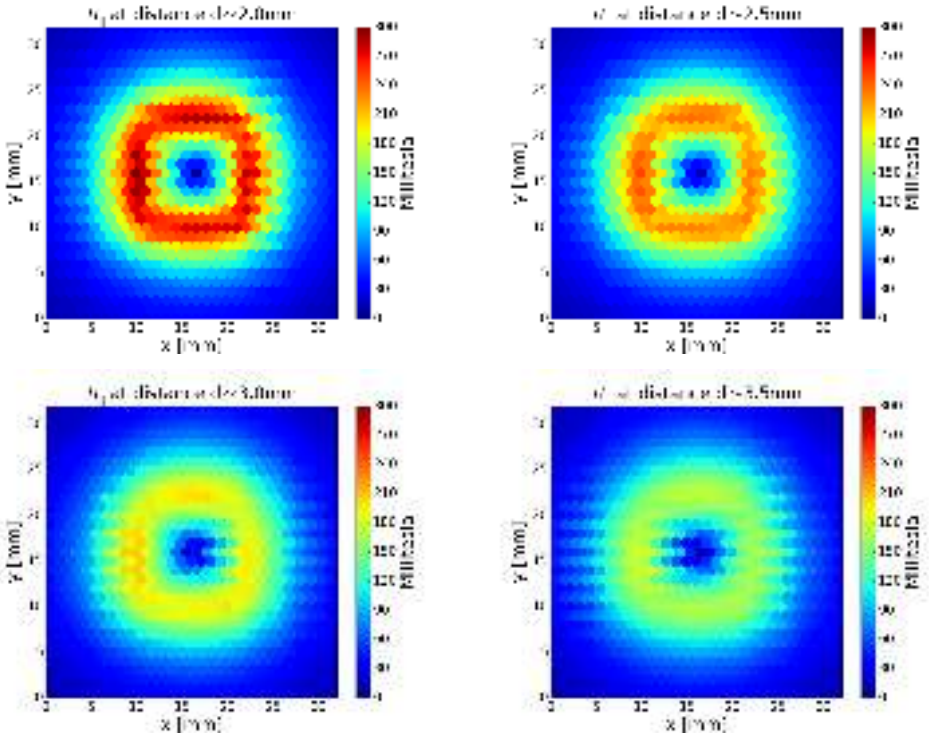

Figure A.5.: Horizontal magnetic field at various distances above the magnet 9.

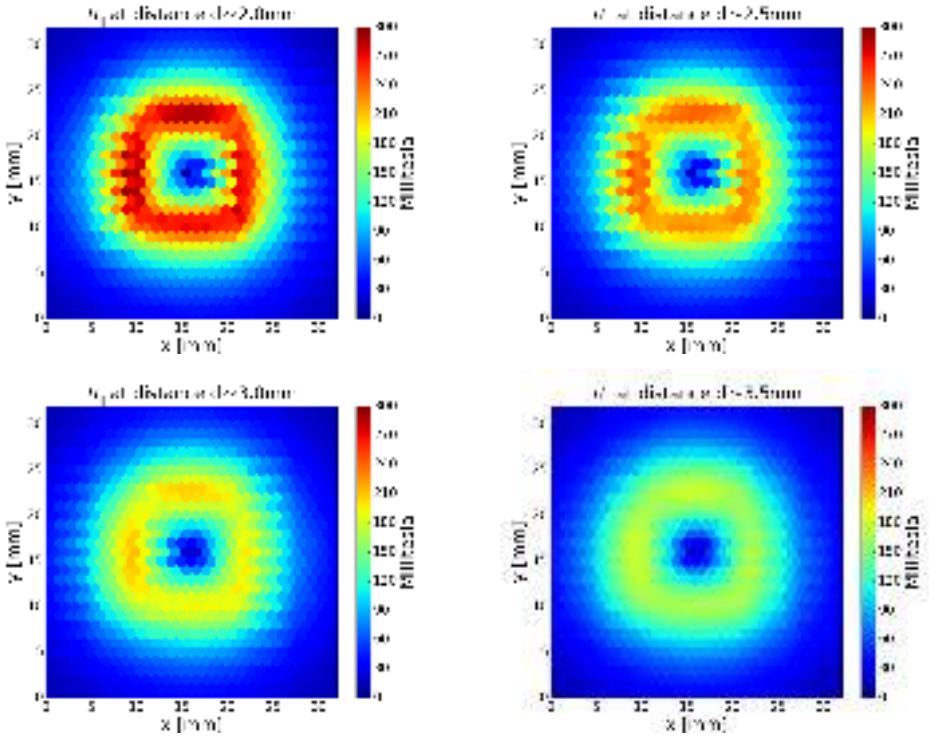

Figure A.6.: Horizontal magnetic field at various distances above the magnet 10.

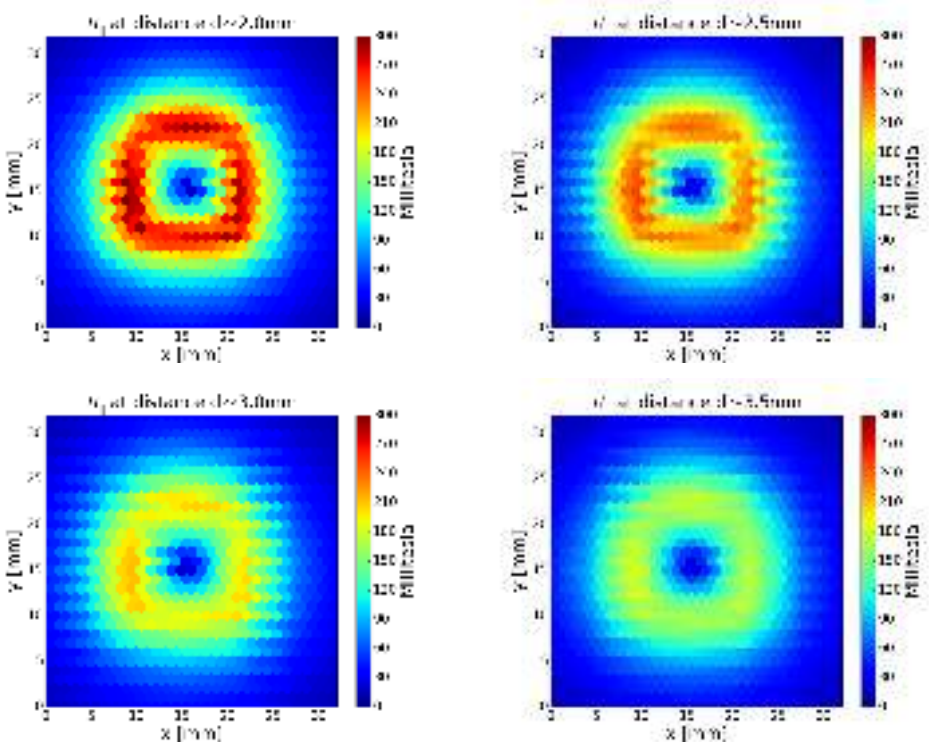

Figure A.7.: Horizontal magnetic field at various distances above the magnet 11.

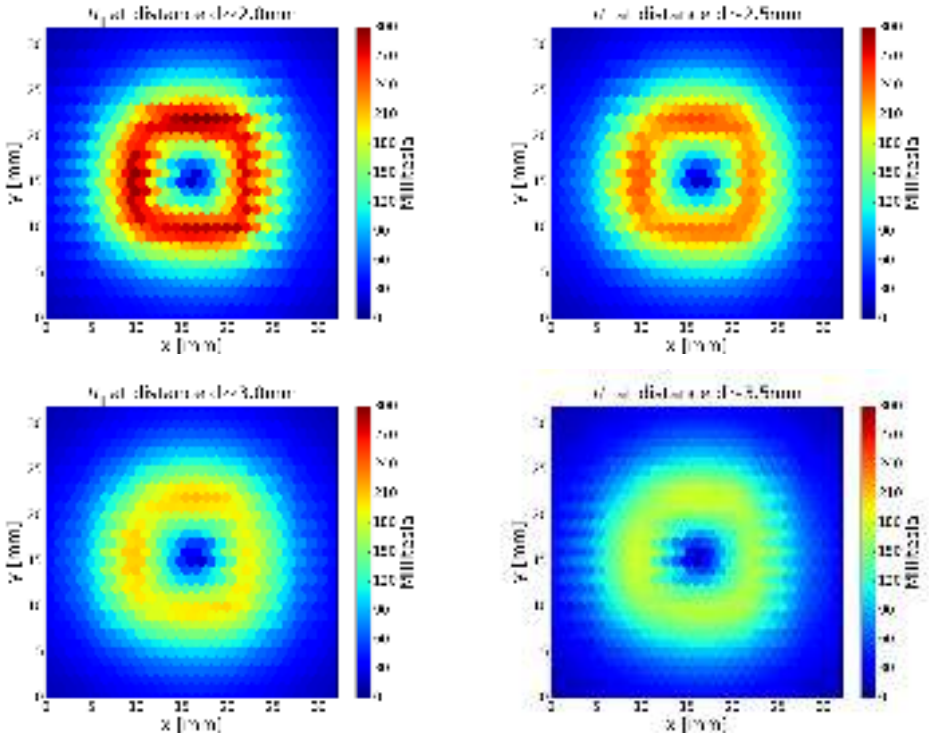

Figure A.8.: Horizontal magnetic field at various distances above the magnet 12.

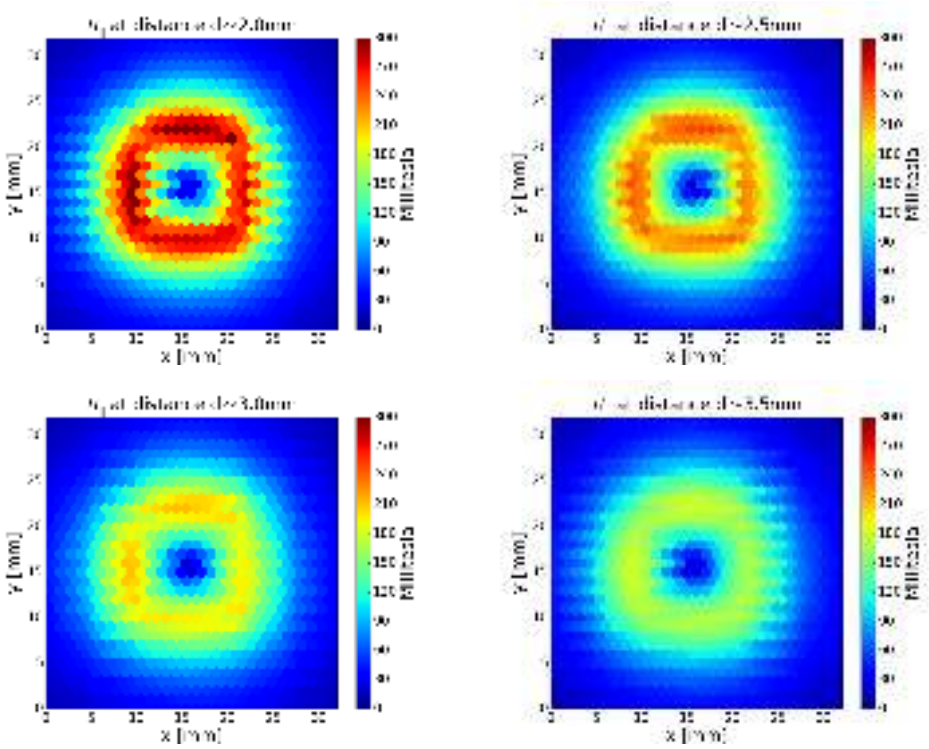

Figure A.9.: Horizontal magnetic field at various distances above the magnet 13.

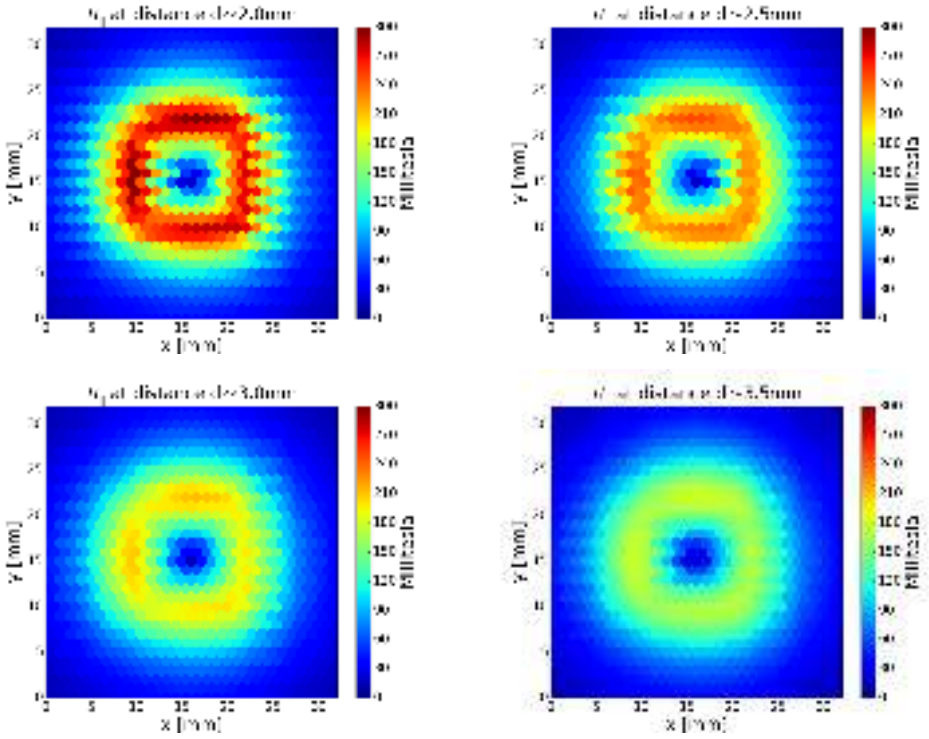

Figure A.10.: Horizontal magnetic field at various distances above the magnet 14.

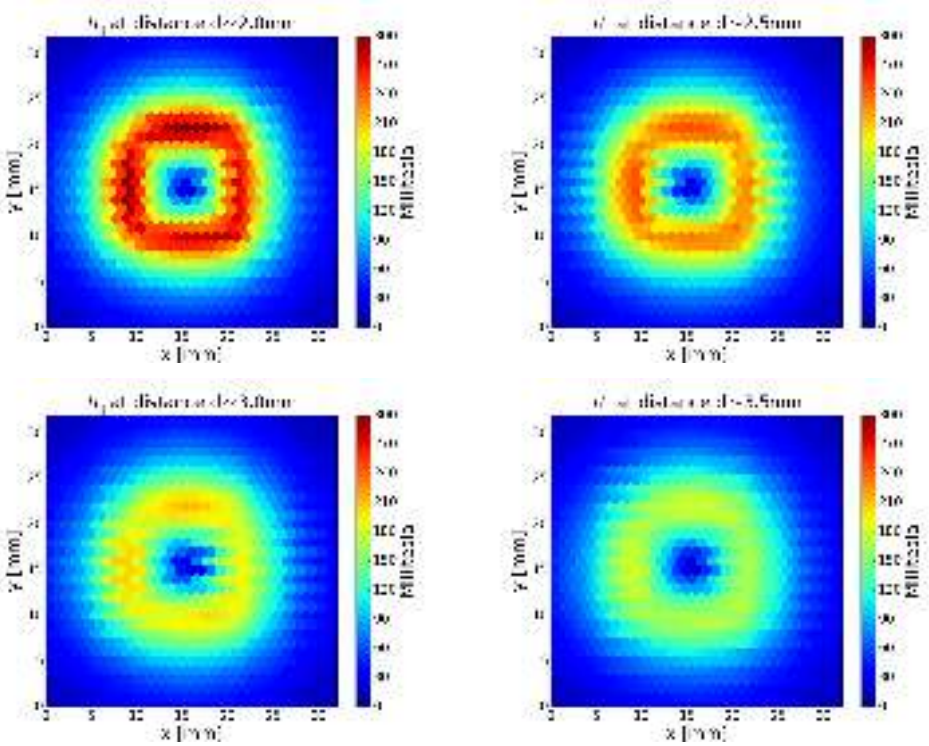

Figure A.11.: Horizontal magnetic field at various distances above the magnet 15.

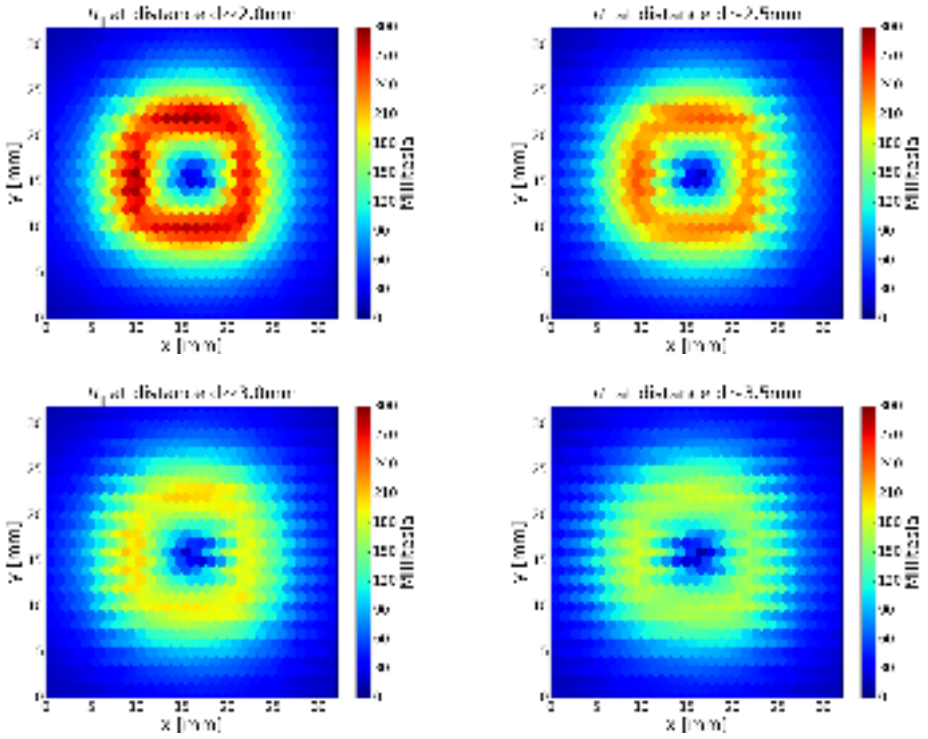

Figure A.12.: Horizontal magnetic field at various distances above the magnet 16.

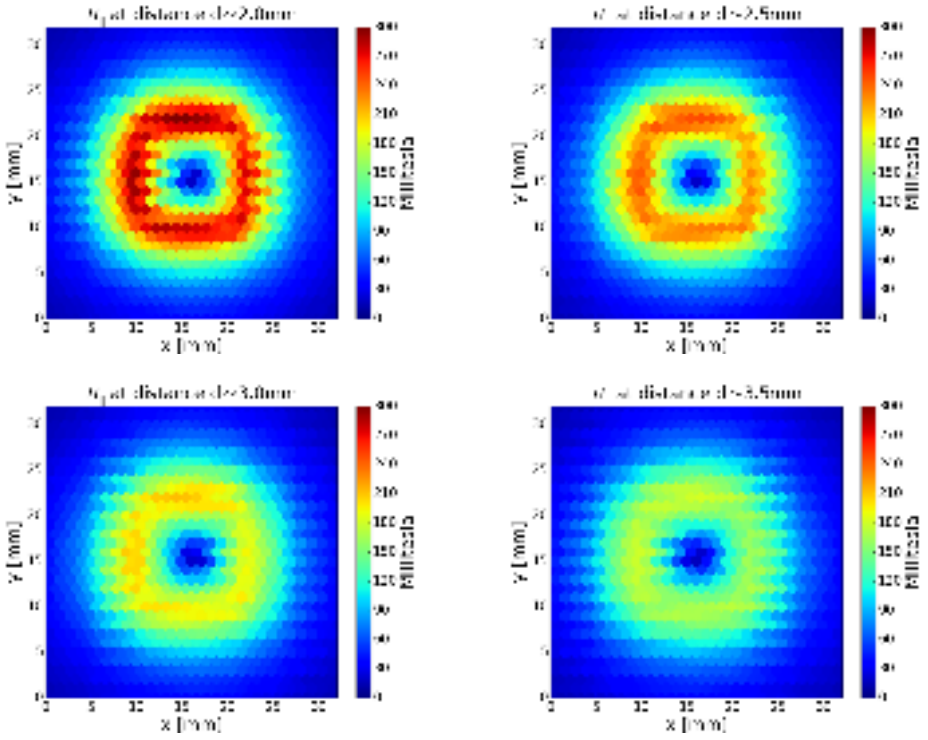

Figure A.13.: Horizontal magnetic field at various distances above the magnet 17.

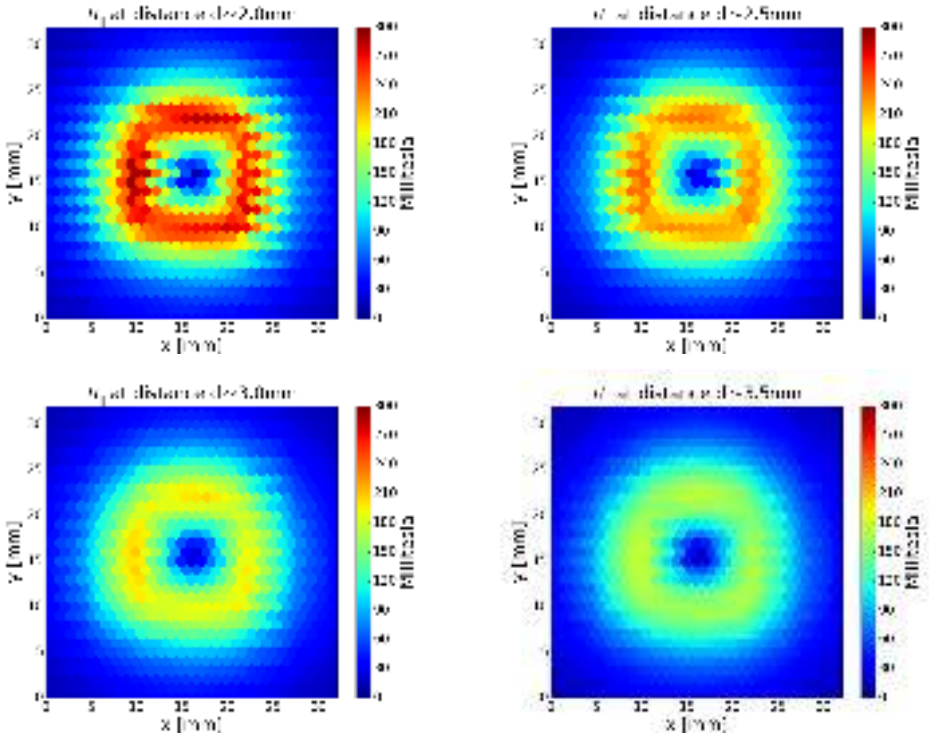

Figure A.14.: Horizontal magnetic field at various distances above the magnet 18.

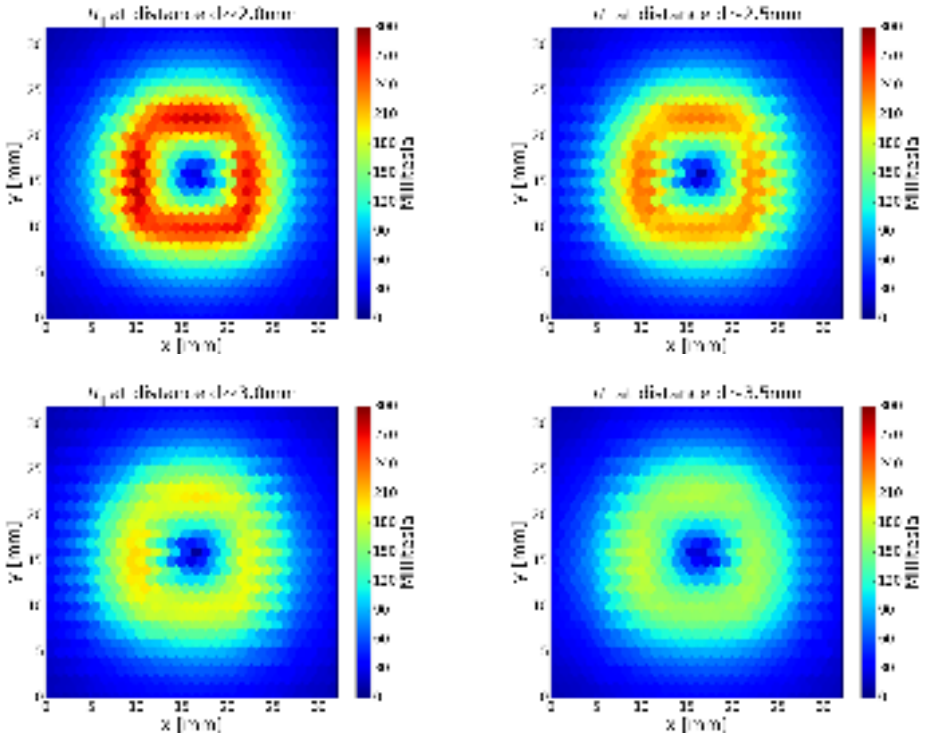

Figure A.15.: Horizontal magnetic field at various distances above the magnet 19.

B. Plots of the second 1D Halbach unit

In this section the plots of the horizontal magnetic field of the second 1D Halbach unit presented in section 5.4 are shown. For every pair of plots, the computational result is above and the experimental result is below.

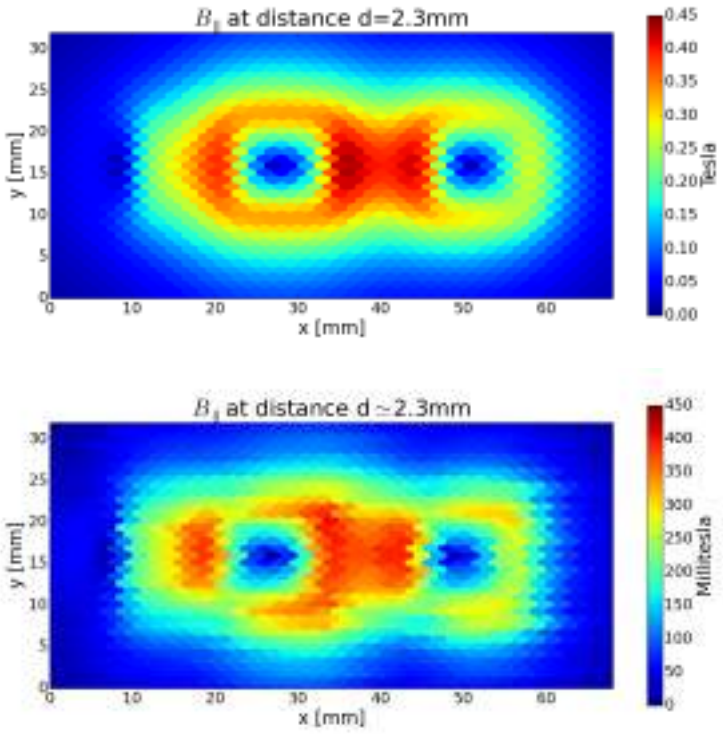

Figure B.1.: Horizontal magnetic field at a distance of 2.3 mm above the unit.

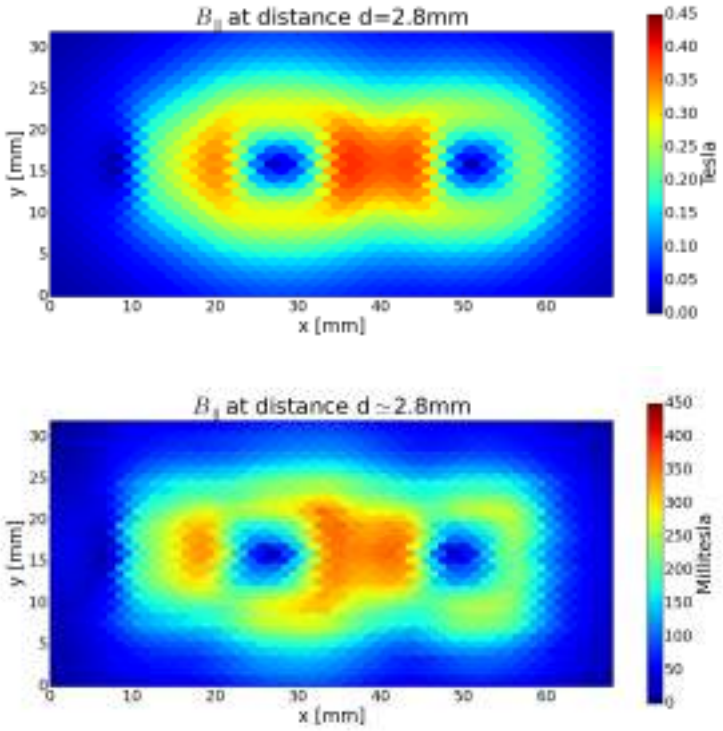

Figure B.2.: Horizontal magnetic field at a distance of 2.8 mm above the unit.

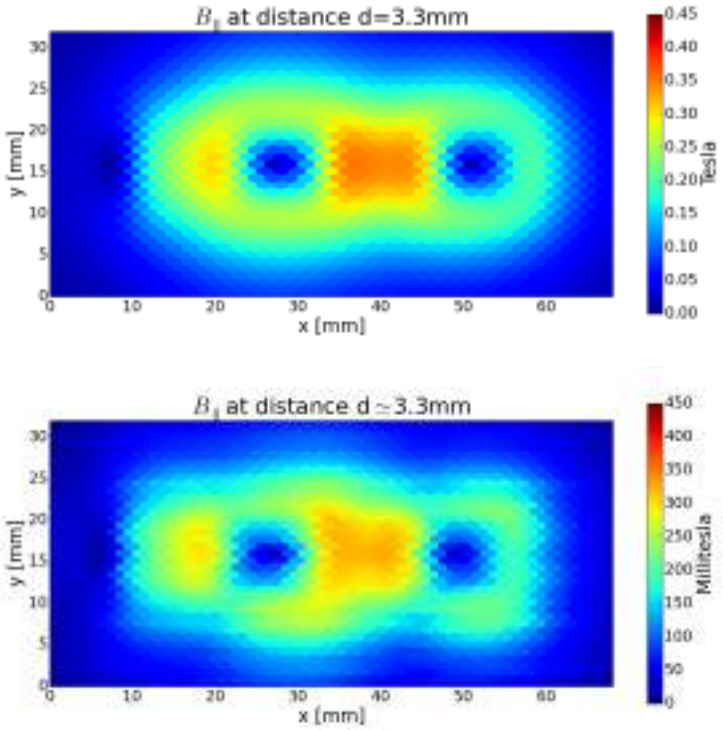

Figure B.3.: Horizontal magnetic field at a distance of 3.3 mm above the unit.

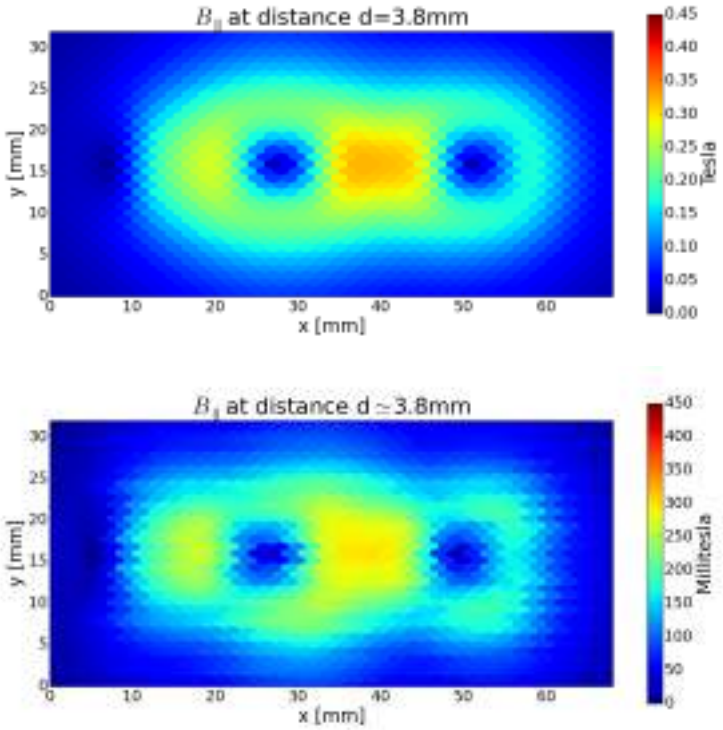

Figure B.4.: Horizontal magnetic field at a distance of 3.8 mm above the unit.

C. Plots of the 5x1 stripes

In this section the plots imaging the measurement of the horizontal magnetic field above the five Halbach stripes consisting of five magnets each, which are presented in section 5.5, are shown.

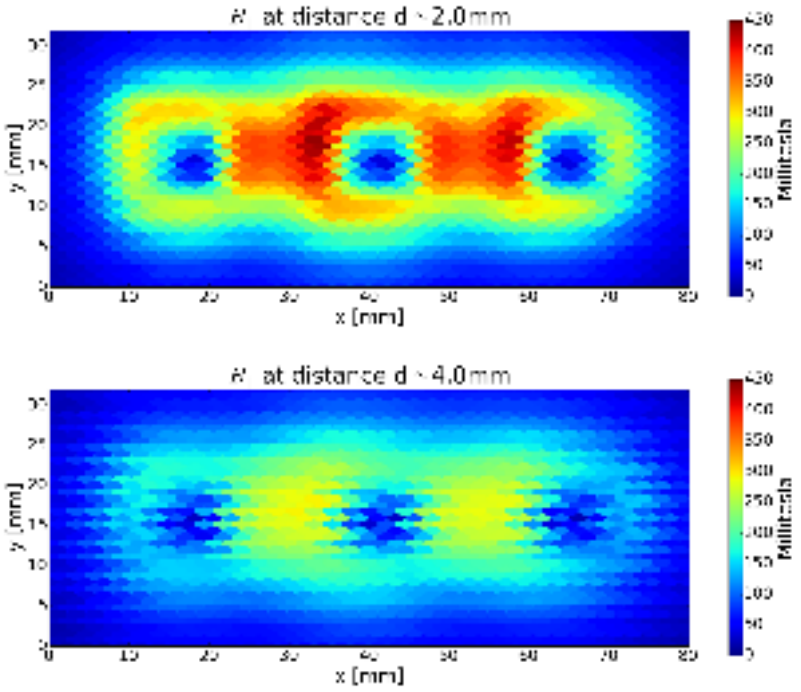

Figure C.1.: Horizontal magnetic field at a distance above the first stripe of 2.0 mm and 4.0 mm respectively.

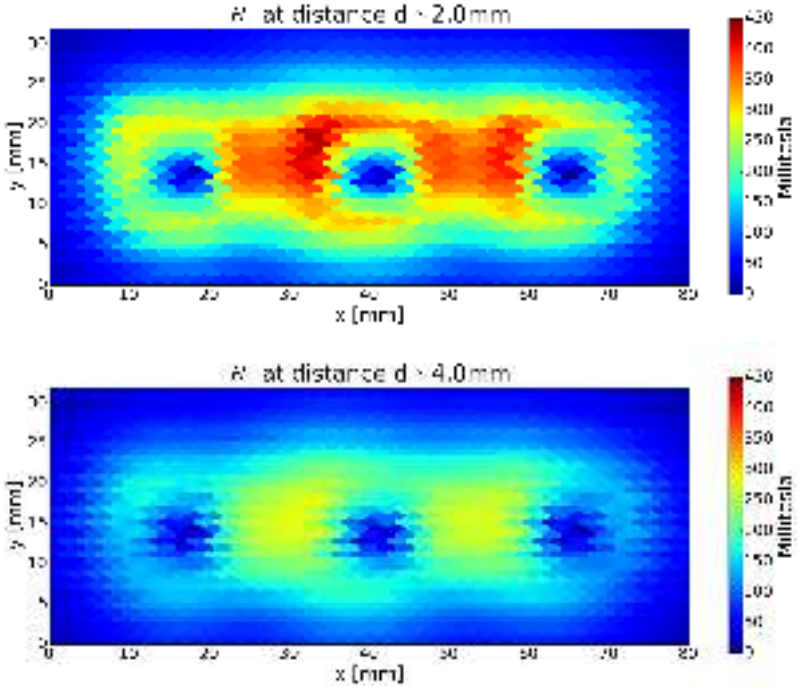

Figure C.2.: Horizontal magnetic field at a distance above the second stripe of 2.0 mm and 4.0 mm respectively.

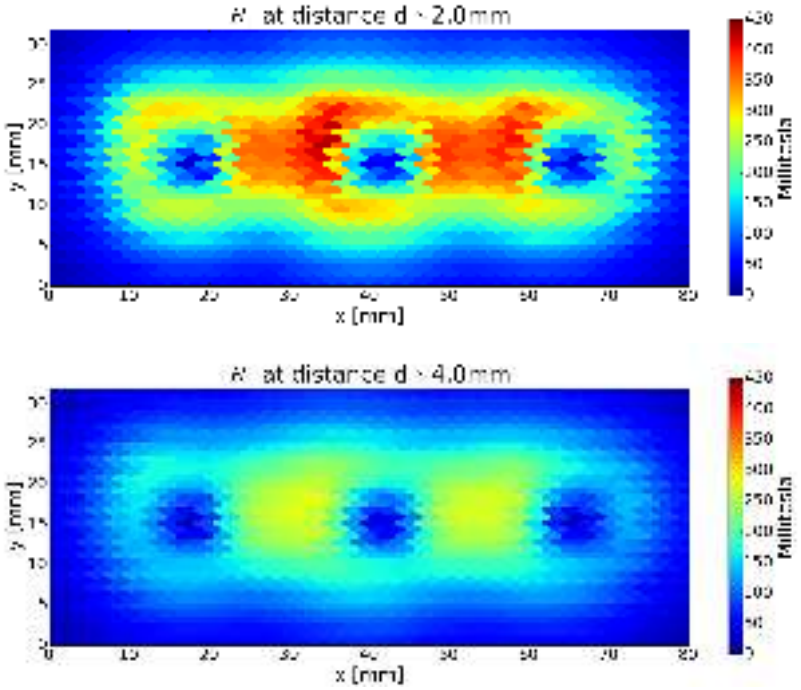

Figure C.3.: Horizontal magnetic field at a distance above the third stripe of 2.0 mm and 4.0 mm respectively.

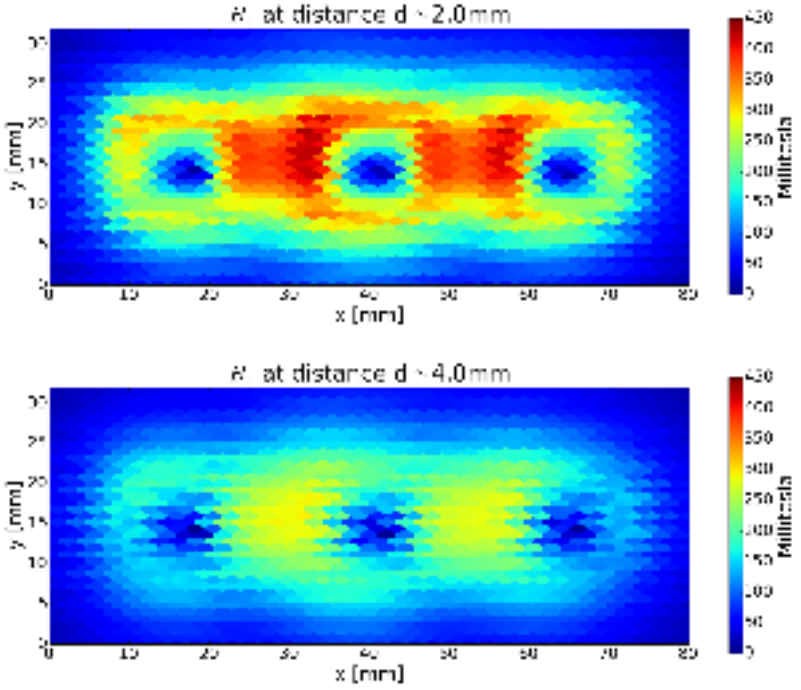

Figure C.4.: Horizontal magnetic field at a distance above the fourth stripe of 2.0 mm and 4.0 mm respectively.

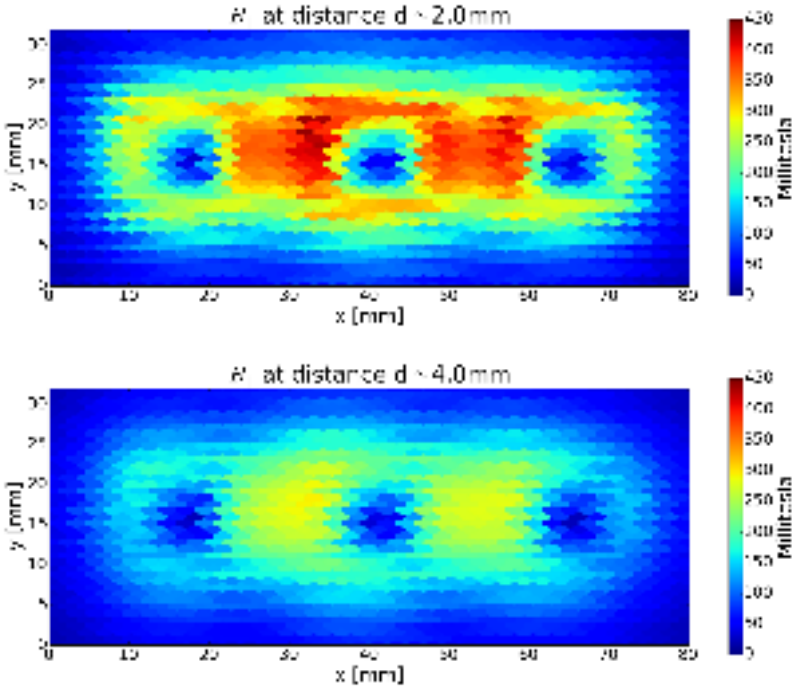

Figure C.5.: Horizontal magnetic field at a distance above the fifth stripe of 2.0 mm and 4.0 mm respectively.

Erklärung

Hiermit bestätige ich, dass die vorliegende Arbeit von mir selbstständig verfasst wurde und ich keine anderen als die angegebenen Hilfsmittel - insbesondere keine im Quellenverzeichnis nicht benannten Internet-Quellen - benutzt habe und die Arbeit von mir vorher nicht einem anderen Prüfungsverfahren eingereicht wurde. Die eingereichte schriftliche Fassung entspricht der auf dem elektronischen Speichermedium. Ich bin damit einverstanden, dass die Masterarbeit veröffentlicht wird.

Sparrieshoop, den 24.10.2017

Christoph Mangels